

博士論文

Controlling the band alignments at complex oxide heterointerfaces

(複合酸化物界面におけるバンドアラインメント制御)

立川 卓

Index

Chapter 1. Introduction.....	1
1.1. Background.....	1
1.2. Scope of this Thesis	5
1.3. Bibliography	7
Chapter 2. Theory.....	8
2.1. Concept of band alignment tuning by electrostatic dipole.....	8
2.2. Mechanisms that may hinder the dipole effect	11
2.2.1. Atomic and electronic reconstructions of polar surfaces.....	11
2.2.2. Pinning effect.....	12
2.3. Bibliography	17
Chapter 3. Experimental.....	19
3.1. Pulsed laser deposition technique.....	19
3.2. Atomic Force Microscopy (AFM).....	23
3.3. X-ray Diffraction	24
3.4. X-ray reflectivity	26
3.5. Electrical transport measurements.....	27
3.6. Characterization technique of vertical transport.....	28
3.6.1. Current-voltage measurement	28
3.6.2. Capacitance voltage measurement	33
3.6.3. Internal photoemission	34
3.7. Bibliography	36
Chapter 4. Fabrication of high quality LaAlO₃/TiO₂/LaAlO₃ heterostructure.....	39
4.1. Introduction.....	39
4.2. Experimental.....	41
4.3. Anatase TiO ₂ thin films growth	42
4.4. Growth parameters for LaAlO ₃ capping layer and crystalline quality of TiO ₂	45
4.5. LaAlO ₃ Repetition rate dependence of anatase TiO ₂	46
4.6. Surface treatment of anatase TiO ₂ (001) surface	49
4.7. Conclusion.....	51
4.8. Bibliography	51

Chapter 5. Band alignment tuning at Pt/LaAlO₃/Nb:TiO₂ interface.....	54
5.1. Introduction.....	54
5.2. Experimental.....	55
5.3. Current voltage measurements.....	57
5.4. Capacitance voltage measurement.....	59
5.5. Internal photoemission technique.....	64
5.6. The origin of barrier height change.....	67
5.7. Attempt to increase barrier height.....	71
5.8. Comparison of three measurement techniques.....	72
5.9. Conclusion.....	72
5.10. Bibliography.....	73
Chapter 6. Band offset increase by AgTaO₃ dipole layer at Pt/Nb:SrTiO₃ interface....	75
6.1. Introduction.....	75
6.2. Experimental.....	77
6.3. Characterizations of basic physical properties of AgTaO ₃	78
6.4. Schottky barrier height characterization.....	81
6.5. Solar cell operation of Pt/AgTaO ₃ junction.....	84
6.6. Conclusion.....	86
6.7. Bibliography.....	87
Chapter 7. Conclusion.....	88
Acknowledgement.....	92
Appendix.....	94
A.1. Maxwell's equation for a metal insulator semiconductor junction.....	94
A.2. Maxwell's equation for a MIS with a dipole layer.....	96

Chapter 1.

Introduction

1.1. Background

Last year, the three Japanese scientists, Prof. Nakamura, Prof. Amano, and Prof. Akasaki won the Nobel Prize in Physics for the invention of efficient blue light emitting diode (LED). The central reason is that the blue LEDs were a foundational step in the creation of bright white LEDs which are inevitable for human society. Nowadays, many of the white incandescent bulbs have been replaced by white LEDs which have much smaller electrical consumption. The invention of a single electrical device has so much impact on human society. Not only the blue LED, many electrical devices like transistors, solar cells and Schottky diodes have taken human societies to the next stage in the long history. Most of these devices properties are strongly governed by 1) appropriate selection and development in the materials quality and 2) control over the electron transport across interfaces between different materials through interface band alignment. These device functionalities are predominantly governed by band alignment engineering. For example in a metal-semiconductor interface, a low barrier would be ideal where series resistance needs to be minimized as in Ohmic contacts, but a high barrier is essential in operating diodes.

Transition metal oxides have attracted much attention as promising candidates for new device applications not achievable in conventional semiconductors. This stems from the diverse electronic properties they exhibit and to their high chemical stability in atmosphere. Some examples such as transparent conductors and photocatalysts for pollutant

	Dipole moment density (D/cm ²)
(CF ₃)(CF ₂) ₇ (CH ₂)Si(OC ₂ H ₅) ₃	1.60 × 10 ¹⁵
Pair of p-type and n-type semiconductor	2.38 × 10 ¹⁴
GaN polar surface (0001)	5.25 × 10 ¹⁵
LaAlO₃ (100)	1.26 × 10¹⁶

Table. 1.1 Dipole moment densities of various systems employed in previous studies [4-7].

remediation are already applied on the industrial scale. Despite the wide range of bulk properties readily available in oxides, controlling the interface energy band alignments of these oxides has a small degree of freedom because of the strong electronegativity of the oxygen anion which predominantly forms the valence band independent of the metal cations leading to fixed ionization energies. This limits access to utilizing the unique intrinsic properties for different device applications in oxide materials [1]. For example, transparent conductors are widely used as top electrodes of solar cells and LEDs. However, the work functions of most transparent conducting oxides are in the range of 4 eV to 5 eV. Therefore, it is difficult to form Ohmic contacts for high work function materials like p-type semiconductors [2,3].

This problem can be resolved by considering the interface electrostatic boundary conditions. Band alignments for any pair of materials can be tuned by insertion of electrostatic dipoles at the interface. It has been demonstrated in compound semiconductors and organic interfaces by using depleted p-n junctions [4] and polar organic molecules as the inserted electrostatic dipoles [5]. Recently, this concept has been applied to oxide interface systems and continuous band alignment tuning has been demonstrated in an-all perovskite SrRuO₃/0.02 wt % Nb doped SrTiO₃ (100) Schottky junction using a perovskite LaAlO₃ as the dipole layer [6]. The crystal structure of LaAlO₃ is shown in Figure 1.1. In the pseudocubic [100] direction, the structure can be regarded as an alternate stacking of LaO layer and AlO₂ layer. Considering the nominal valence of ions in each layer, LaO layer has +1 charge and AlO₂ layer has -1 charge which is the origin of electrostatic dipole. Because of the highly ionic nature of oxides, the expected dipole moment of 1 u.c. LaAlO₃ is equal to dipole moment of +1 and -1 charge separated by the lattice constant of LaAlO₃. Namely, it is calculated from the following:

$$P = QdN = \frac{Q}{d} \quad (1.1)$$

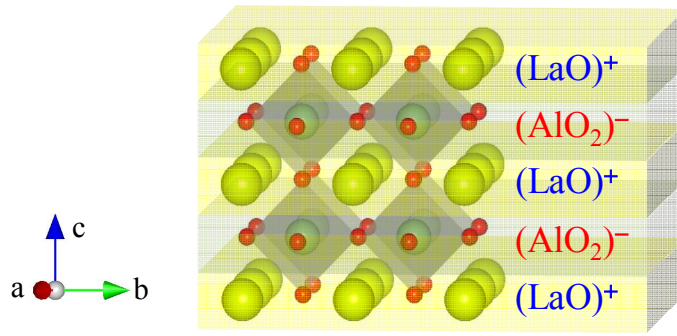


Figure. 1.1 Crystal structure of LaAlO₃.

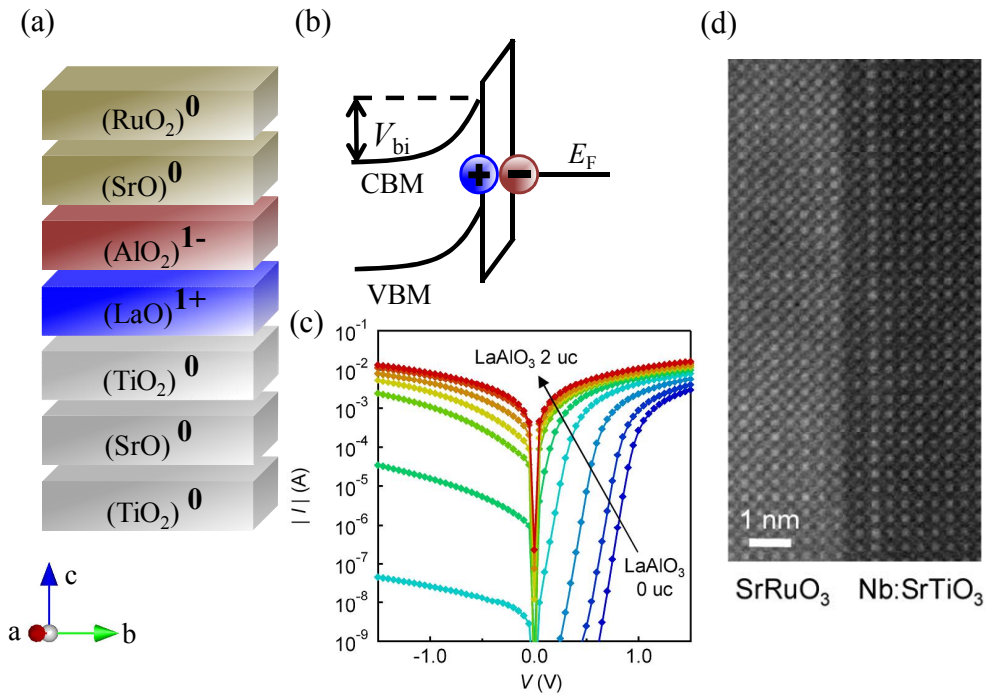


Figure. 1.2 (a) The schematic structure, (b) the band diagram, and (c) the I - V curves of SrRuO₃/LaAlO₃/SrTiO₃ (100) junction. (d) Scanning tunneling electron microscopy (STEM) image of the SrRuO₃/Nb:SrTiO₃ (100) junction without LaAlO₃ insertion [6].

where Q is charge density of single (LaO)⁺ or (AlO₂)⁻ unit layer, d is the lattice constant of LaAlO₃, N is the number of u.c./cm². The expected dipole moment densities of LaAlO₃ and various dipoles in organic materials and compound semiconductors are summarized in Table. 1.1 [4-7]. The dipole moment density of the polar organic molecule is calculated as the product of the molecular dipole moment and the sheet density of the adsorbed molecule same as the study of Kobayashi *et al.* [5]. According to the table, the estimated dipole moment of LaAlO₃ is at least three times larger than the other dipole layers employed previously.

Schematics of the junction structure, the band structure and the current voltage ($I-V$) curves for the all-perovskite Schottky junctions are shown Figures. 1.2 (a)-(c). The SBHs obtained from the $I-V$ curves monotonically decreased with the insertion of LaAlO_3 . It should be noted that continuous tuning of SBH was achieved by depositing fractional layers of LaAlO_3 which is difficult for polar organic molecules or polar surfaces of nitride semiconductors. Since the all-perovskite junctions can be grown with structural coherently from the bottom semiconductor to the top metal layer with a lattice mismatch smaller than 4 %, atomically flat and abrupt interfaces were readily obtained as shown in Figure 1.2 (d).

The ultimate goal for exploring device functionalities in oxides, we need to expand the application of dipole engineering technique to potentially less well-defined interfaces and clarify the structural requirements for this technique to be feasible. The schematic of the strategy is shown in Figure. 1.3. In order to achieve the ultimate goal, two different challenges should be overcome. First, the structural requirement to utilize this dipole has to be clarified. Although the isostructural interface is suitable for the demonstration of the concept, most of the practical devices are non-isostructural interfaces where abrupt interfaces are not always available. For example, polycrystalline metal films, rather than epitaxial films, are widely used as metal electrodes since they still hold good metallicity as deposited by standard evaporator at room temperature without considering the epitaxial

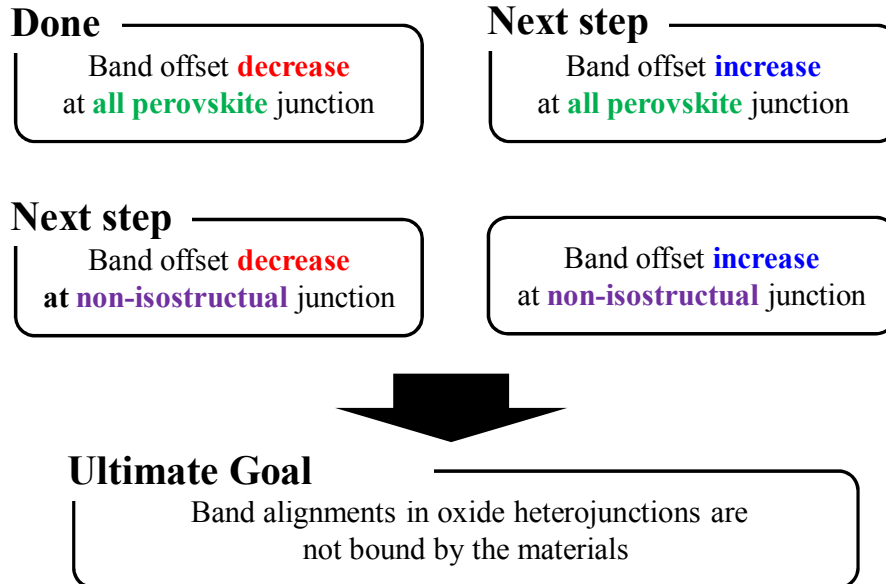


Figure. 1.3 The grand strategy in this study.

relation. Furthermore, binary oxides, whose crystal structures are not perovskite, are promising for various applications because of its chemical stabilities and simplicity of stoichiometry. For example, TiO_2 attracts much attention as photocatalysts [8], ZrO_2 has been widely employed for fuel cells [9], ZnO is a promising material for UV LEDs cheaper than GaN [10].

Second goal is bidirectional dipole tuning. If band alignment can be both decreased and increased in a wide range, the materials selection for devices can be made on the intrinsic bulk properties and unconstrained by the band offset. A sign of the perovskite oxide dipole is determined by the stacking order of charged layer on the semiconductor substrate. As shown in Figure 1.4 (a), if the negatively charged layer is adjacent to the semiconductor, the band offset is expected to increase. If LaAlO_3 is utilized to achieve a band offset increase, the negatively charged $(\text{AlO}_2)^-$ layer has to be deposited on the SrO terminated SrTiO_3 as shown in Figure 1.4 (b). However, the tunable range of the band offset by perovskite oxide dipole is -0.6 eV to $+0.2 \text{ eV}$, with smaller range in increasing the dipole potential.

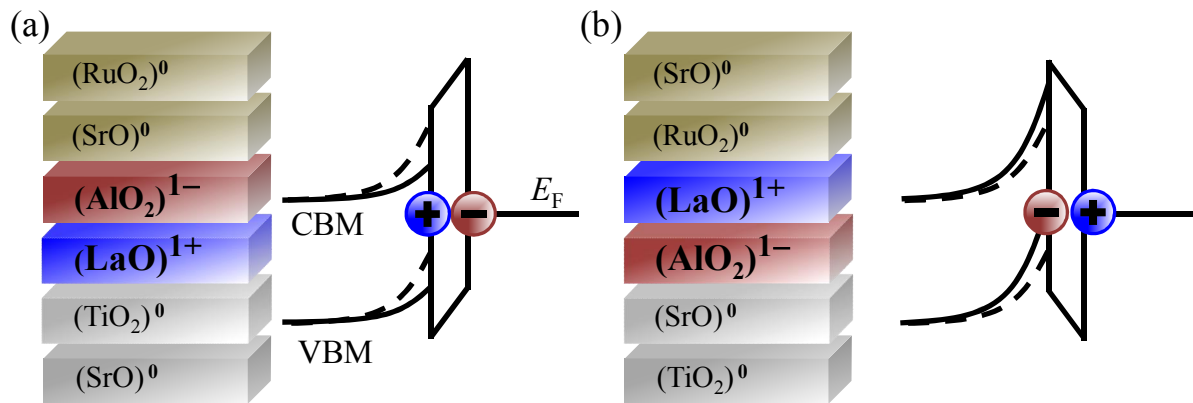


Figure. 1.4 Stacking structures and band diagrams of (a) the LaO/TiO_2 interface and (b) the AlO_2/SrO interface of $\text{SrRuO}_3/\text{LaAlO}_3/\text{SrTiO}_3$ (100).

1.2. Scope of this Thesis

Given the importance of band alignment tuning technique for designing device structures, the central motivation of this research is to clarify the feasibility of oxide dipoles in general. In particular, we set three goals shown below

1. Clarify the structural requirements to utilize electrostatic dipoles

Non iso-structural interfaces are susceptible to various phenomena that may screen electrostatic dipoles, for example, surface reconstructions of polar surfaces and pinning effects. These effects are strongly dependent on the crystal structures and forms of the constituting materials of the interface. Therefore, we aim to clarify the structural requirements to activate the dipole effect. Especially, considering the importance of binary oxides and polycrystalline metal electrodes for device applications, we set following three questions.

- (i) Can band alignments be tuned at a polycrystalline metal/single crystalline oxide semiconductor interface by oxide dipoles?
- (ii) Does the dipole layer need to be grown epitaxially?
- (iii) Can the oxide dipole tune the band alignment of non-perovskite interfaces?

In order to answer these questions, we studied polycrystalline Pt/LaAlO₃/anatase TiO₂ (001) interfaces which have a polycrystalline metal electrode, a non-perovskite semiconductor and oxide dipole/semiconductor interface whose epitaxial relation can be controlled by the surface reconstruction of anatase TiO₂ (001).

2. Demonstration of increase in band offset by electrostatic dipoles

The previous study of bi-directional dipole tuning was based on using LaAlO₃ as the dipole layer on the termination controlled SrTiO₃ (100) surfaces exploiting the iso-structural nature of the junction. Namely, for a SrO terminated surface, an AlO₂⁻ layer forms first and for a TiO₂ terminated case, a LaO⁺ layer forms first thereby reversing the sign of the dipole. However, the experimentally obtained dipole sign was independent of the termination likely due to the instability of the SrO-terminated SrTiO₃ (100) surface. Here we used an alternative perovskite insulator AgTaO₃. Assuming the formal valence of Ag⁺ and Ta⁵⁺ in AgTaO₃, we can expect to stabilize the negatively charged (AgO)⁻ layer on a stable TiO₂-terminated SrTiO₃ (100) surface.

3. Establish SBH measurement technique of the junction with electrostatic dipole.

Generally, SBHs can be characterized by current voltage measurement, capacitance voltage measurement, and internal photoemission technique. Although they are very well established techniques in conventional semiconductors, SBHs obtained by them do not match all the time. In Schottky junctions consisting of a low doped compound semiconductor and a simple metal, internal photoemission technique is generally considered as the most reliable technique [11]. However, in the case of

metal-insulator-semiconductor junction, internal photoemission spectra can be complicated because of the existence of the tunneling barrier. Therefore, we aimed to apply these three different methods for the same heterojunction and compare the results to establish the understanding of the advantages and disadvantages of each in this system.

1.3. Bibliography

- [1] A. Kudo and Y. Miseki, Chem. Soc. Rev. **38**, 253 (2008).
- [2] N. Wang, X. X. Liu, and X. Y. Liu: Adv. Mater. **22**, 2211 (2010).
- [3] M. G. Helander, M. T. Greiner, Z. B. Wang, W. M. Tang, and Z. H. Lu, J. Vac. Sci. Tec. A **29**, 011019 (2011).
- [4] F. Capasso, A. Y. Cho, K. Mohammed, and P. W. Foy, Appl. Phys. Lett. **46**, 664 (1985).
- [5] S. Kobayashi, T. Nishikawa, T. Takenobu, S. Mori, T. Shimoda, T. Mitani, H. Shimotani, N. Yoshimoto, S. Ogawa, and Y. Iwasa, Nat. Mater. **3**, 317 (2004).
- [6] T. Yajima PhD Thesis (2012).
- [7] I. Vurgaftman and J. R. Meyer, J. Appl. Phys. **94**, 3675 (2003).
- [8] A. Fujishima and K. Honda, Nature **238**, 5358 (1972).
- [9] N. Q. Minh, J. Am. Ceram.Soc. **76**, 563 (1993).
- [10] A. Tsukazaki, M. Kubota, A. Ohtomo, T. Onuma, K. Ohtani, H. Ohno, S. F. Chichibu, and M. Kawasaki, Jpn. J. Appl. Phys. **44**, L643 (2005).
- [11] S. M. Sze and K. K. Ng, *Physics of Semiconductor Devices*, Wiley (1981) .

Chapter 2. Theory

2.1. Concept of band alignment tuning by electrostatic dipole

Interface band alignments are determined by the relationship between the intrinsic physical properties of the two constituent materials. The basic principles of band alignments are described in Figure. 2.1 using a Schottky junction consisting of a metal and an n-type semiconductor. In the following discussion, it is assumed that there is no electric field in the

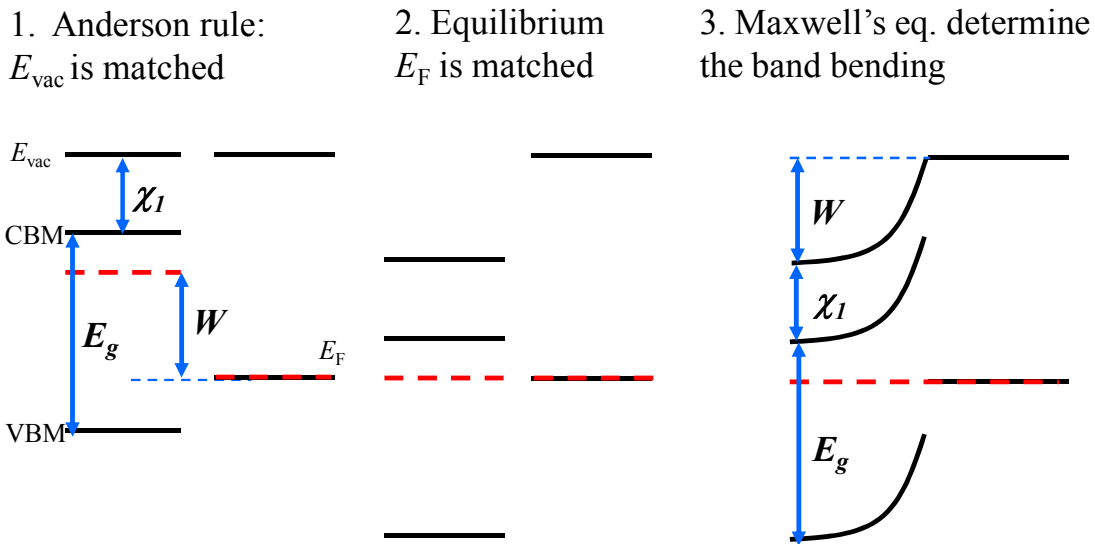


Figure. 2.1 The basic principle of a band alignment for a n-type semiconductor and a metal. χ_1 and E_g are the electron affinity and the band gap of the semiconductor. W is the work function difference. E_{vac} is the vacuum level, E_{F} is the Fermi level of the metal.

metal since the carrier density of the metal is much higher than the semiconductor. First, the Anderson rule, which states that vacuum level of the two materials are equal when they are isolated at an infinite distance, determines the relative positions of the energy bands before a junction is formed [1]. Second, the Fermi level of these two materials matches as they form a junction. Third, the conduction band bottom of the semiconductor ($\phi(z)$) is described by the Maxwell's equation:

$$\frac{\partial^2 \phi(z)}{\partial z^2} = -\frac{\rho(z)}{\varepsilon} \quad (2.1)$$

solved under the boundary conditions of,

$$\phi(z = z_0) = 0 \quad (2.2)$$

$$\phi(z = 0) = E_{F_metal} - E_{F_semi} = W \quad (2.3)$$

$$\frac{\partial \phi(z = z_0)}{\partial z} = 0 \quad (2.4)$$

where E_{F_metal} and E_{F_semi} are the work function of the metal and the semiconductor. The coordination is defined so that z is defined as the distance normal to the interface towards the semiconductor and the origin is the interface of the semiconductor and the metal. ε is the dielectric constant of the semiconductor and z_0 is the thickness of the depletion layer. The conduction band bottom of the semiconductor at an infinite distance from the interface is defined as 0. Charge density ($\rho(z)$) is given by

$$\rho(z) = qN_D \quad (z_0 < z < 0) \quad (2.5)$$

$$\rho(z) = 0 \quad \text{for else} \quad (2.6)$$

By using them, the solution of (2.1) is calculated as

$$\phi(z) = -\frac{qN_D}{2\varepsilon} \left(z + \sqrt{\frac{2\varepsilon W}{qN_D}} \right)^2 \quad \left(-\sqrt{\frac{2\varepsilon W}{qN_D}} < z < 0 \right) \quad (2.7)$$

As shown in Figure. 2.1, the band alignments are determined by the work function, the electron affinity and the semiconductor band gap. Since these physical properties are unique to each material and difficult to control, band alignments are determined by the constituting materials. However, it is often difficult to find an appropriate material that has desired bulk physical properties and forms ideal band alignments for a device with arbitrary materials. A reduction in the number of prerequisites for material choices lets us revisit device structure prohibited before. Out of the many restrictions, band alignments at interfaces can be tuned by inserting electrostatic dipoles between two materials. Figure. 2.2 explains the concept of

electrostatic dipoles in Schottky junctions. In the case of an ideal Schottky junction, the Schottky barrier height (SBH) is equal to the difference in work function of the metal and electron affinity of the semiconductor. When the electrostatic dipole is inserted at the interface, the vacuum level of the two materials at an infinite distance have an offset equal to the built in potential of the electrostatic dipole. When the junction is formed, the SBH is also modified by this built-in potential. Therefore, if we establish the technique to continuously tune the dipole moment at the interface, arbitrary SBH from any combinations of materials should be achievable.

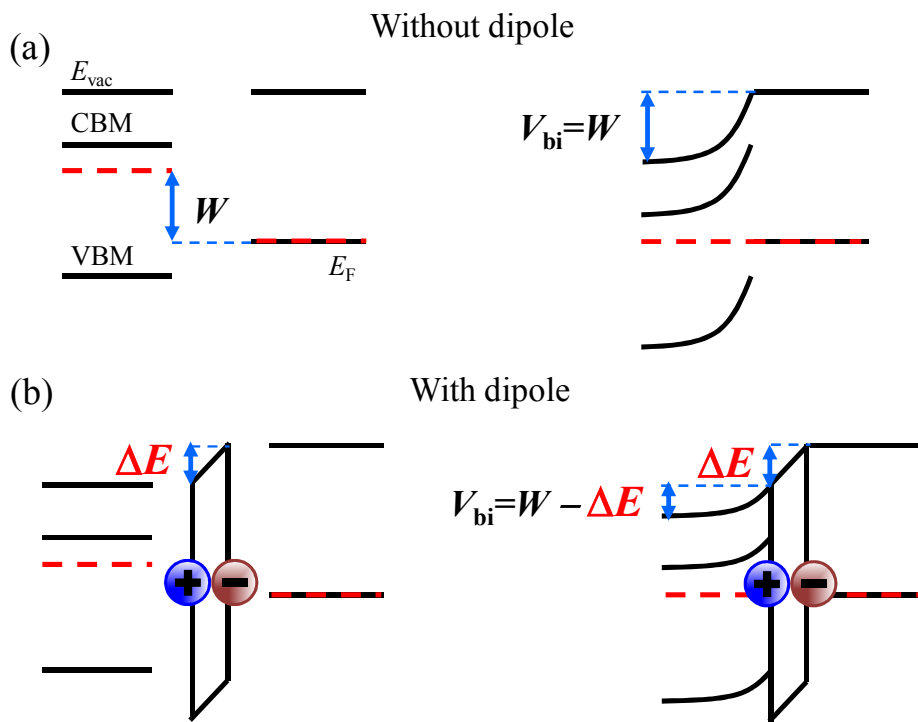


Figure. 2.2 Band diagrams of the Schottky junction (a) without and (b) with electrostatic dipoles. ΔE corresponds to the built-in potential of the dipole.

2.2. Mechanisms that may hinder the dipole effect

In this section, two possible mechanisms in semiconductors and insulators that may hinder band alignments tuning by electrostatic dipoles are discussed. These are reconstruction at polar surfaces and pinning effects. The possibility of each phenomenon in oxide interfaces is discussed later.

2.2.1. Atomic and electronic reconstructions of polar surfaces

.When electrostatic dipole moment at a surface becomes non zero, the surface is defined as a polar surface. The surface dipole moment is calculated from the spatial distribution of the Wannier functions of the occupied bands [2]. Polar surfaces are energetically unstable and are susceptible to atomic and electronic reconstructions. The spatial distribution of the charges can be estimated from the knowledge of the ground-state electron distribution in the bulk unit cell, which is quite accurately provided either by high-resolution x-ray diffraction experiments, as shown for example in the alumino-silicate compounds [3], or by first-principles methods, such as those based on the density functional theory (DFT) [4]. Actually, in most cases, atomic configurations of ions and their valences

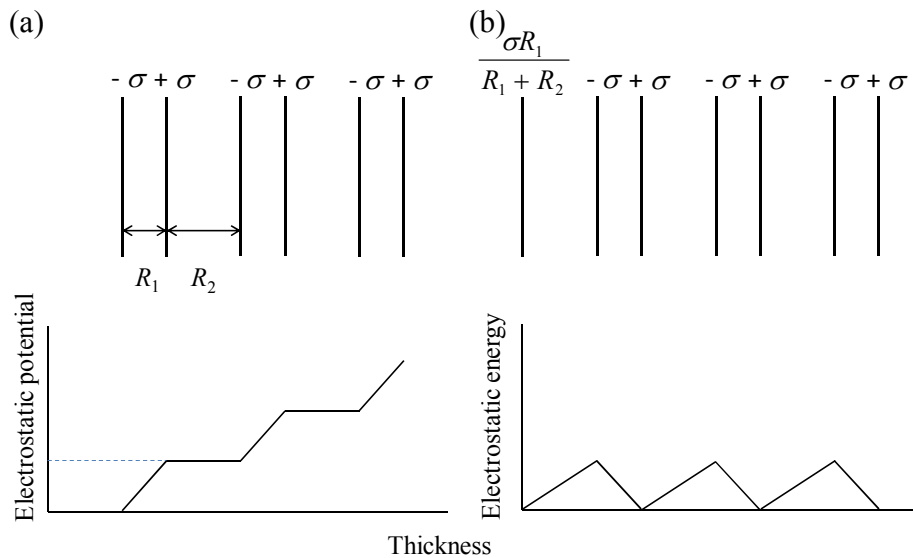


Figure. 2.3 (a) The charge distribution and electrostatic potential of the polar surface that holds non-zero dipole moment in all the repeating unit cells. The origin is defined as surface. (b) The same polar surface with compensating charge at the top surface to suppress the divergence of electrostatic potential.

are enough to judge whether a surface is polar or not.

In the case of a polar surface that hold non-zero electrostatic dipole moment in all the repeating unit cells through the material, the electrostatic surface potential is cut along a polar direction is given in Figure. 2.3, where the unit cell consists of two atomic layers with charge densities of $+\sigma$ and $-\sigma$ separated by the spacing R_1 and the inter-unit cell spacing is R_2 . Each unit cell bears a dipole moment density equal to $\mu = \sigma R_1$, and, as a result, the electrostatic potential increases monotonically across the system by an amount $\delta V = 4\pi\sigma R_1$ per unit cell which is typically of the order of several tens of eV in ionic oxides. The total dipole moment $M = N\sigma R_1$ and the electrostatic energy amounts to $E = 2\pi N R_1 \sigma^2$ for N unit cells. In the limit $N \rightarrow \infty$, which is the bulk crystal, the electrostatic contribution to the surface energy diverges.

Specific modifications of the charge density in the outer layers may suppress the divergence of the dipole moment and the electrostatic energy. Figure. 2.3 (b) shows how this can be achieved, for example, by assigning a value $\sigma R_2 / (R_1 + R_2)$ to the charge density on the outer layers of the slab, and this results in a total dipole moment $M = \sigma R_1 R_2 / (R_1 + R_2)$ which is constant independent of the thickness. A polar surface can thus be stabilized by charge compensation achieved by reconstruction of atomic configuration, charged defects, or formation of two dimensional electron gases [5-7].

Since the charge modification decreases the total dipole moment of the polar surface, it should be suppressed for the sake of band alignment tuning. Because the driving force of this charge modification is the increase in the total surface electrostatic energy proportional to the thickness, there is a critical thickness at which the charge modification occurs [8]. Therefore, the dipole layer thickness should be smaller than the critical thickness in order to tune the band alignment.

2.2.2. Pinning effect

The presence of a continuum of surface states in the gap may cause a pinning effect. Originally, this effect was found in Schottky junctions where the SBHs found for a wide range of metals on a particular semiconductor seemed to fall within the narrow range around at a two thirds of the band gap for n-type (one third for p-type) semiconductor from the valence band [9,10]. Since the Fermi level of the semiconductor surface appeared to be pinned to a specific value independent of the metal, this effect is called as the pinning effect. This is because the high density of surface states equilibrate with the bulk semiconductor and not between the metal and the semiconductor as shown in Figure. 2.4 (b).

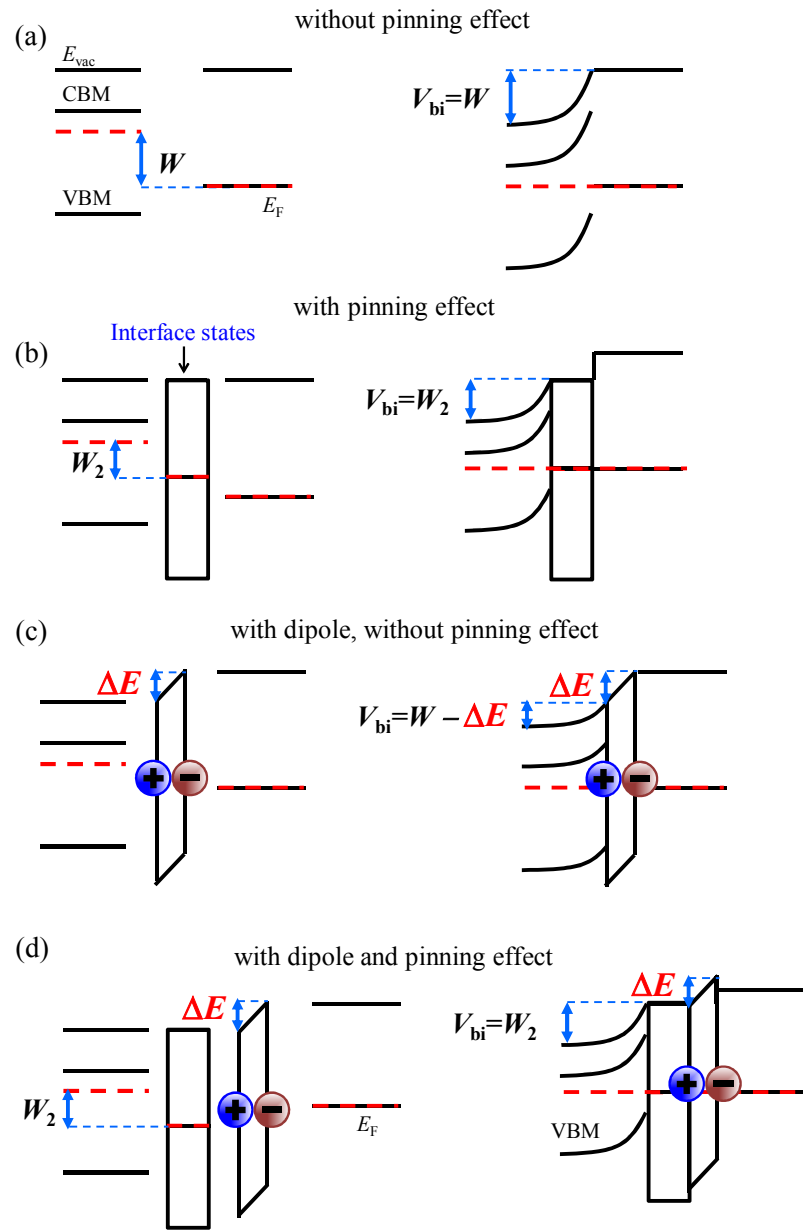


Figure. 2.4 Band alignments of Schottky junctions (a) without pinning effect, (b) with pinning effect, (c) with dipole and without pinning, (d) with dipole and with pinning effect. W_2 is the work function difference of the interface state and the bulk semiconductor.

When the charge density of interface states are not enough to screen the space charges in the semiconductor, systematic trend was observed for the SBH and the metal work function. However, their correlation is much weaker than that expected from Schottky Mott rule where the SBHs is defined as the difference between the metal work function and the semiconductor electron affinity. The gradient of the linear fitting which is expressed as

S_ϕ and obtained by the least-square technique for the SBH vs. metal work function is often utilized as strength of pinning effect for a given semiconductor.

Previously, it was reported that S_ϕ monotonically increases with the ionicity of materials which is defined by the difference in the electron negativity of the constituent elements as shown in Figure. 2.6 (a) [11]. Therefore, most of the Schottky junctions consisting of transition metal oxides were expected to have no pinning effect because of its ionic nature. However, this trend has been denied by further research performed by M. Schluter proving that electronic dielectric constant is a good parameter to explain the trend in S_ϕ as shown in (b) [12]. In addition, some of the oxides have large scattering in S_ϕ values mainly due to the degree of disorder in the junction which is large in non-isostructural junctions. Therefore in the case of non-isostructural Schottky junctions, pinning effect is likely to happen even in ionic oxides.

Pinning effect is expected to screen the barrier height tuning induced by the dipole effect too. Figure. 2.4 (c) and (d) show the band alignment of the metal-insulator-semiconductor junction with and without pinning effect where the insulator has an electrostatic dipole. As we have already seen in the case of without the pinning effect, the SBH is changed by the built in potential of the electrostatic dipole. However, in the case of strong pinning effect, the dipole only changes the band offset between the interface state and the metal. SBH is determined by the band bending of the semiconductor which is still determined by the Fermi energy difference of the interface state and the bulk semiconductor.

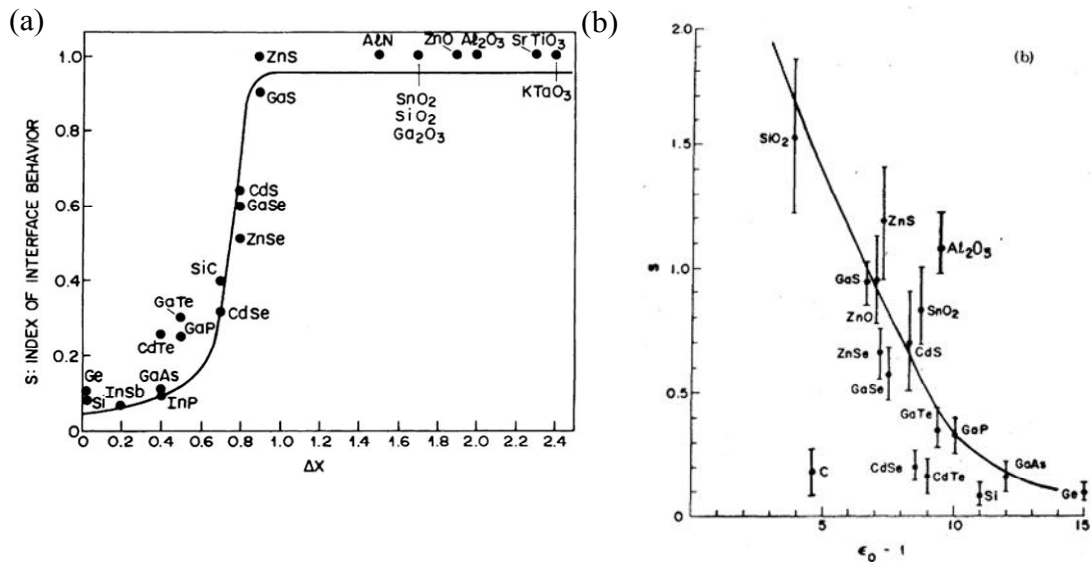


Figure. 2.5 (a) S_ϕ vs. electronegativities of various semiconductors [11]. (b) S_ϕ vs. electronic dielectric constants of various semiconductors reanalyzed by M. Schluter [12].

Therefore, pinning effect is expected to disable the dipole effect as well.

There are two major origins for interface states that cause pinning effect reported in conventional semiconductors. The first is overlap of wave functions at a metal semiconductor interface which can significantly alter the electronic structure and the charge distribution at the interface forming metal induced gap states (MIGS). Although the states

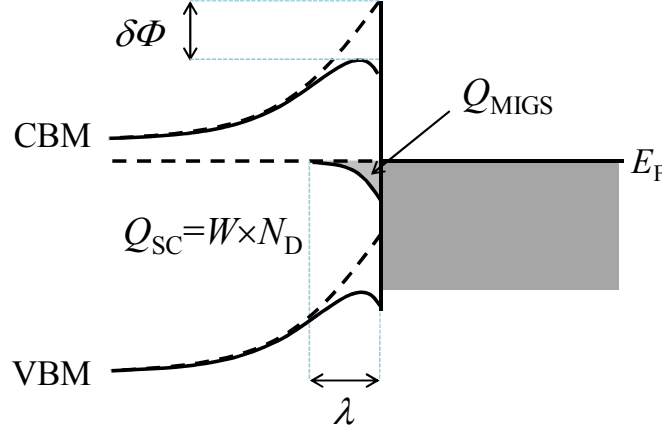


Figure. 2.6 A band diagram of a Schottky junction with metal induced gap states. Band bending without MIGS is displayed as dashed lines.

are induced by the metal, the energy distribution of the states is determined by the semiconductor electronic structure within the band gap. The typical band alignment of a Schottky junction with MIGS is shown in Figure. 2.6 [13,14].

The MIGS effects in oxides are examined by considering the penetration length of the MIGS. The MIGS decay from the metal semiconductor interface toward the semiconductor with a characteristic length that correlates with the ionicity of the semiconductor. The barrier height lowering by MIGS is calculated from the following equation [15]

$$\delta\Phi_{\text{MIGS}} = e\lambda \frac{Q_{\text{SC}}}{\epsilon_s} \ln \left| \frac{Q_{\text{MIGS}}}{Q_{\text{SC}}} \right| \quad (2.8)$$

where λ is the penetration length of MIGS, ϵ_s is the dielectric constant of the semiconductor, Q_{SC} and Q_{MIGS} are the charge density of the space charge region and the MIGS, respectively. MIGS always decrease SBH because MIGS are negatively charged and penetrate into the positively charged depletion layer in the n-type semiconductor. Since charge distribution of MIGS is explained by a simple tunneling picture of metal wave function to semiconductor, the penetration length is longer for smaller band gap material [16]. Thus, typical penetration

length of MIGS in oxide material is smaller than 0.4 nm which is not enough to cause significant barrier height modification.

The second is a thin disordered layer produced by depositions of insulator or metal on semiconductors. Iso-structural interfaces tend to form epitaxial interface with small defect densities since long range order provides the largest energy gain by cohesion. However, at non-isostructural interfaces, conservation of perfect crystal in semiconductor is not necessarily the most energetically favorable atomic configuration. Namely, formation of defects or atomic reconstruction can lower the total energy at the interface. The disordered layers formed by them are characterized by the fluctuations of bond length and bond angles due to interface irregularity. Anderson localization, which is the wave interference between multiple scattering paths leads to the defect induced gap states (DIGS) in the energy gap whose density depends on the degree of the disorders.

The location of the Fermi level of the DIGS spectrum can be obtained by an LCAO tight binding model where the matrix size extends over all the sites in the structure so as to

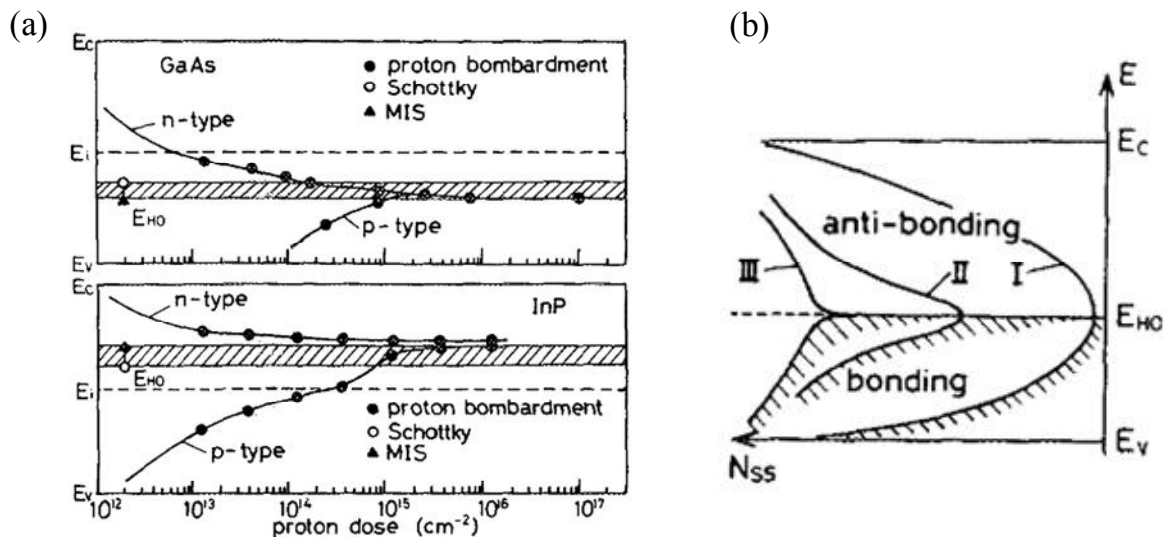


Figure. 2.7 (a) The Fermi energy of proton bombarded GaAs and InP estimated from electrical conductivity data [17-19]. (b) Density of states of DIGS for I-S interface with small disorder (I), with highly disordered (II) and M-S interface [17]. E_c is the conduction band minimum, E_v is the valence band maximum, E_i is the intrinsic Fermi level and N_{ss} is the density of states.

account for the disorder. In the case of conventional semiconductors like Si, Ge and III-V semiconductors, the Fermi level of DIGS is equal to the hybrid orbital energy of the bond E_{HO} , which is the averaged energy of hybridized bonding in semiconductor independent of

degree of disorder as shown in Figure. 2.7 (a) [17-19]. The density of states of DIGS at three different interfaces are shown in Figure. 2.7 (b) and they have symmetric distribution around the E_{HO} . Their shapes are extremely sensitive to the properties and the degree of disorders of deposited insulator or metal and the deposition process itself [20].

Since DIGS depend on the preparation processes and the atomic configurations of the two materials at the interface, it can be a problem in non-isostructural oxide interfaces. Therefore, optimizations of the growth conditions for dipole layers and metals could be crucial in activating the electrostatic dipoles.

2.3. Bibliography

- [1] R. L. Anderson, J. Res. Dev. **4**, 283 (1960).
- [2] D. Vanderbilt and R. D. King-Smith, Phys. Rev. B **48**, 4442 (1993).
- [3] S. Kuntzinger, N. E. Ghermani, Y. Dusausoy, and C. Lecomte, Acta Crystal. B-Stru. **54**, 819 (1998).
- [4] E.G. See, R. G. Parr and Y. Wang, *Density Functional Theory of Atoms and Molecules*, Oxford University Press (1989).
- [5] A. Pojani, F. Finocchi, and C. Noguera, Appl. Surf. Sci. **142**, 177 (1999).
- [6] A. Ohtomo and H. Y. Hwang, Nature **427**, 423 (2004).
- [7] N. Nakagawa, H. Y. Hwang, and D. A. Muller, Nat. Mater. **5**, 204 (2006).
- [8] E. Lesne, N. Reyren, D. Doennig, R. Mattana, H. Jaffrès, V. Cros, F. Petroff, F. Choueikani, P. Ohresser, R. Pentcheva, A. Barthélémy, and M. Bibes, Nat. Commun. **5**, 4291 (2014).
- [9] W. G. Spitzer and C. A. Mead, J. Appl. Phys. **34**, 3061 (1963).
- [10] C. A. Mead and W. G. Spitzer, Phys. Rev. **134**, A713 (1964).
- [11] S. Kurtin, T. C. McGill, and C. A. Mead, Phys. Rev. Lett. **22**, 1433 (1969).

- [12] M. Schlüter, Phys. Rev. B **17**, 5044 (1978).
- [13] G. H. Parker, T. C. McGill, C. A. Mead, and D. Hoffman, Solid-State Electron. **11**, 201 (1968).
- [14] J. M. Andrews and M. P. Lepselter, Solid-State Electron. **13**, 1011 (1970).
- [15] R. T. Tung, Appl. Phys. Lett. **58**, 2821 (1991).
- [16] V. Heine, Phys. Rev. **138**, A1689 (1965).
- [17] H. Hasegawa and H. Ohno, J. Vac. Sci. & Tech. B **4**, 1130 (1986).
- [18] J. C Dymont, J. C North, and L. A. D'Asaro, J. Appl. Phys. **44**, 207 (1993).
- [19] J. P. Donney and C. E. Hurwitz, Solid-State Electron. **20**, 727 (1977).
- [20] S. Dueñas, H. Castán, H. García, A. de Castro, L. Bailón, K. Kukli, A. Aidla, J. Aarik, H. Mändar, T. Uustare, J. Lu, and A. Hårsta, J. Appl. Phys. **99**, 054902 (2006).

Chapter 3.

Experimental

In this chapter, each experimental technique employed in this study will be briefly explained. Transition metal oxide thin films were deposited on (100) oriented perovskite oxide substrates by using the pulsed laser deposition (PLD) technique. The thickness of the films was estimated by counting the number of intensity oscillations from the reflection high-energy electron diffraction (RHEED) spots during growth. After the growth, X-Ray reflectometry (XRR) was used in order to confirm the actual thickness. The crystalline quality of thin films was characterized by X-ray diffraction (XRD), atomic force microscopy (AFM), and Raman scattering spectroscopy. The temperature dependent resistivity and Hall measurements were carried out in Physical Properties Measurement System (PPMS). Room temperature junction electrical transport measurements were performed using a probe station with an LCR meter and a semiconductor parameter analyzer (SPA). An internal photoemission technique was also utilized to obtain the SBH. Optical transmittance and reflectance were characterized by using ultraviolet-visible spectrometer (UV-Vis).

3.1. Pulsed laser deposition technique

In this study, PLD was employed for deposition of high-quality transition metal oxide thin films. This technique is widely used to grow functional oxides [1,2]. The basic

fabricating scheme is as follows:

1. A high power pulsed laser beam is focused inside a vacuum chamber to strike a target of the material that is to be deposited.
2. The surface of the target is heated and the material is vaporized resulting in a plasma, so called "plume" [3, 4].

The plasma expands away from the target surface due to the strong Coulomb repulsion among the ablated species and the recoil from the target surface under high vacuum (10^{-5} Torr) [5]. The ablated species are deposited on the surface of a substrate positioned opposite to the target, a portion of which forms the nucleation cluster. The sticking coefficient is different from neutral atoms [6]. Finally, these nuclei coalesce and cover the entire surface producing a uniform thin film.

PLD is a physical vapor deposition process similar to molecular beam epitaxy (MBE) in the following senses. Both of them are processes under ultra high vacuum that eliminate impurities from residual gases and are capable of utilizing various in-situ growth monitoring techniques such as RHEED [7, 8], and surface X-ray diffraction [9,10].

There are many advantages in PLD techniques. Firstly, the stoichiometry of the grown thin film is mainly determined by that of the target enabling fabrication of multi-component materials. This contrasts to typical oxide MBE growth which requires independent control of the constituent cations. Secondly, the laser system is placed outside the chamber, that is not affected by the condition inside the chamber like oxygen partial pressure. Most of the growth techniques including MBE have their precursor sources inside the chamber. Thirdly, the high kinetic energy of the plasma makes it possible to perform low temperature growth of thin films compared with MBE [11,12]. Fourthly, PLD is applicable to many materials having high melting points. Figure. 3.1 shows the schematic picture of the PLD system employed in this study. A pulsed KrF Excimer laser (COMPexPro 201F, Coherent Inc.) with a pulse duration time of about 25 ns and $\lambda = 248$ nm was used for the ablation of the oxide targets. The pulsed nature of the laser gives two independently controllable parameters which govern the growth kinetics, namely the volume of species ablated per shot and the time interval between pulses. The former parameter depends on the laser power on the target surface that is adjusted by rotating the variable attenuator. The latter parameter is determined by the laser repetition rate, which is modulated by changing the frequency of the input trigger voltage by a function generator (DS345, Stanford research systems, Inc.).

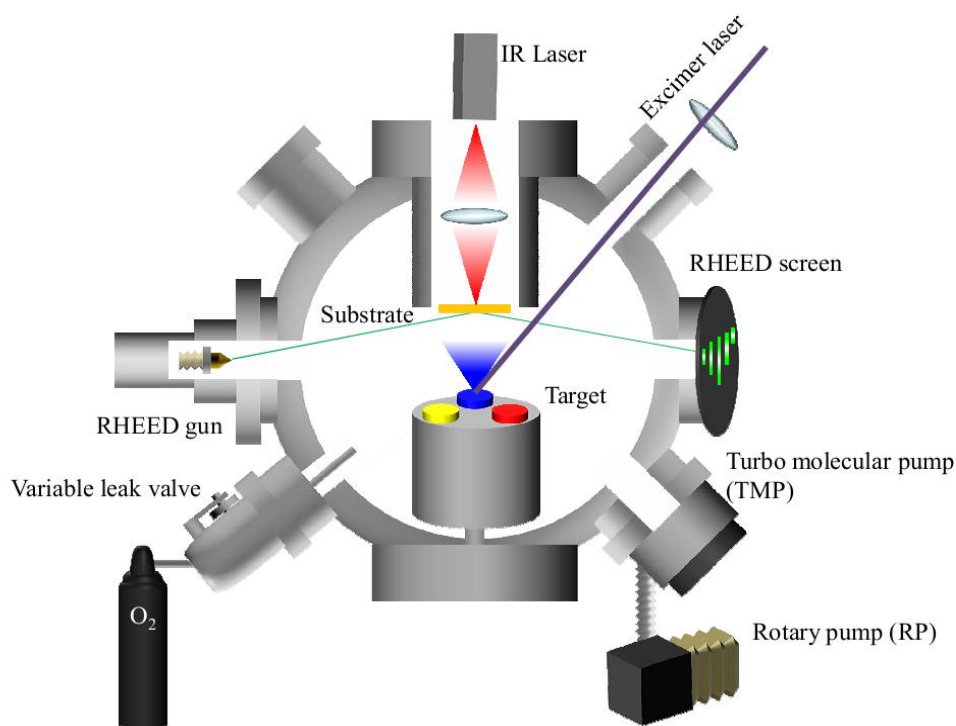


Figure. 3.1 A schematic pulsed laser deposition apparatus.

The LaAlO_3 (100) substrate was cut into ($5 \times 5 \text{ mm}^2$) and attached to the center of a carbon plate with Pt paste. This carbon plate is mounted on the sample holder and fixed using Inconel wires. The thin film growth is performed under oxygen atmosphere. The base pressure of the chamber is around 10^{-9} Torr which mainly consists of water and nitrogen. High purity oxygen (99.999 %) is introduced during growth and its partial pressure is precisely controlled by a variable leak valve to 10^{-8} Torr accuracy. The oxygen partial pressure is monitored by an ion gauge under high vacuum ($< 10^{-5}$ Torr) and a capacitance gauge for low vacuum ($> 10^{-3}$ Torr). The substrate is heated by a continuous infrared laser (PA-LH0601-001-T, Pascal) guided through an optical fiber bundle from the top flange radiating the back side of the carbon plate where the substrate is mounted. The substrate temperature is monitored by the observation of the black body radiation from the carbon plate using a pyrometer. The maximum available temperature is around $1300 \text{ }^\circ\text{C}$.

During the growth, the thin film surface is monitored by RHEED (ARH-100 Vacuum products Co., Ltd) which is widely used to characterize the surface structures of crystalline materials as shown in Figure. 3.2 [10,13]. The incident angle of the electron beam was kept at a glancing angle in order to prevent the electron beam from transmitting into the bulk region. The basic principle is that diffraction occurs when two different

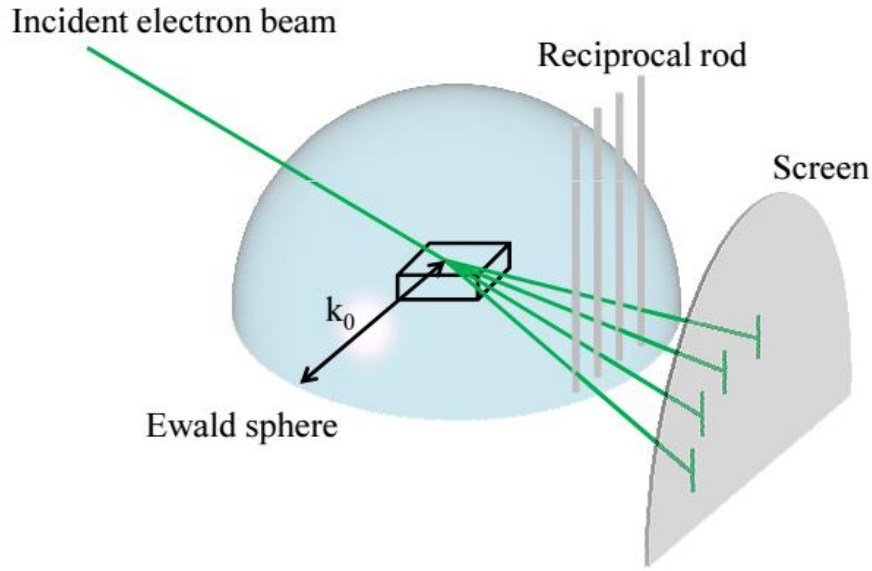


Figure. 3.2 The principle of reflection high energy electron diffraction (RHEED).

reciprocal points, which are Fourier transforms of the crystal structure in real space, exist on the surface of an Ewald sphere whose radius equals the incident electron beam wave vector k_0 . In the case of RHEED, the electrons are reflected mainly in the top-most surface of the thin film and the reciprocal points are degenerated into reciprocal rods. The wave vector of the incident electron is expressed as

$$k = \frac{1}{\hbar} \sqrt{2m_e E + \frac{E^2}{c^2}} \quad (3.1)$$

where $k = 785\text{nm}^{-1}$ when the energy of the electron $E = 20\text{ keV}$, and \hbar is the Plank constant divided by 2π , and m_e is the free electron mass. The lattice constant of reciprocal unit cell of anatase TiO_2 is 2.64 nm^{-1} and 1.05 nm^{-1} for a-axis and c-axis, respectively. Since the radius of the Ewald sphere is substantially larger than the reciprocal of the lattice constant, the intersection of the Ewald sphere and the reciprocal rods become long that result in a streak pattern on the screen. In the Frank-van der Merwe growth mode, so called the layer-by-layer growth mode, where complete films form prior to growth of subsequent layers, the intensity of RHEED diffraction spot is known to oscillate periodically. The relationship between the intensity and the surface morphology change during growth is shown in Figure. 3.3. In the initial stage of the growth, adatoms attach to the surface and form many nuclei resulting in rough surface which lowers the diffraction intensity of the RHEED. As the growth progresses, the nuclei become large and the surface turns flat

increasing the diffraction intensity. In the case of anatase TiO_2 thin films, a single RHEED oscillation corresponds to the deposition of 0.5 unit cell [14]. This technique enables us to control the thickness of the grown thin films with sub-monolayer accuracy.

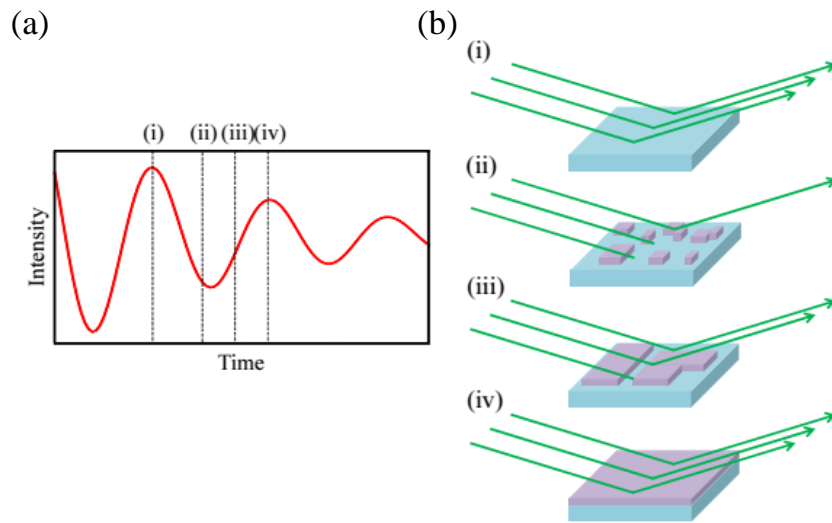


Figure. 3.3 (a) An intensity oscillation of RHEED diffraction spot during thin film growth. (i) to (iv) corresponds to the each step during the formation of one monolayer shown in (b).

3.2. Atomic Force Microscopy (AFM)

Atomic force microscopy (AFM) is one of the foremost techniques for imaging, measuring, and manipulating matter at the nanoscale. The principle of measurement depends on atomic force between the surface and the tip. Since atomic forces exist in all materials, AFM is capable of measuring any samples. In addition, the samples measured in AFM do not

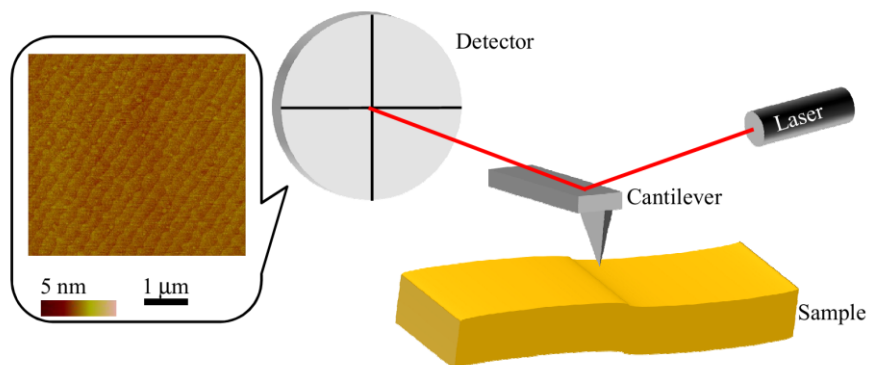


Figure. 3.4 The principle of Atomic Force microscope.

require any special treatment or environment such as metal coating or high vacuum unlike the case of scanning tunneling microscope, for example. A schematic picture of an AFM is shown in Figure. 3.4. In this research, the tapping mode AFM was employed, in which the cantilever is driven near its resonance frequency. Compared with contact mode where tip touches the surface, tapping mode causes minimal damage to the surface. Laser light from a solid state diode is reflected from the back of the cantilever and detected by a photodiode as the cantilever oscillates as it scans across the sample surface. The deflection of the cantilever is detected by the position of the laser spot on the photodiode. When the tip-surface distance changes, the amplitude of the tapping oscillation changes accordingly. The servomotor attached to cantilever adjusts the tip-surface distance to maintain a constant cantilever oscillation amplitude as the cantilever is scanned over the sample. A tapping mode AFM image is therefore produced by imaging the force of the intermittent contacts of the tip with the sample surface. Typical accuracy in the z-direction is better than 1 nm with the scan range of several micrometers.

3.3. X-ray Diffraction

X-ray diffraction (XRD) techniques are widely used as a non-destructive technique which reveals information about the crystallographic structure because wavelengths of X-rays is typically of similar order to the lattice constants. The XRD techniques are based on Bragg's law:

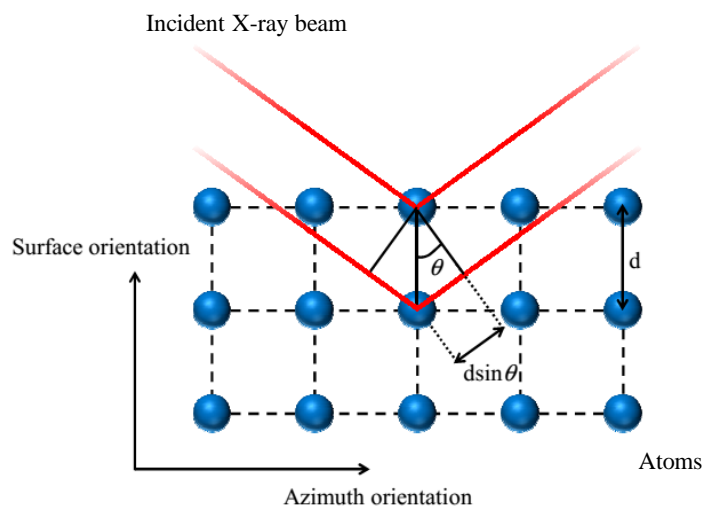


Figure. 3.5 Bragg's law.

$$2d \sin \theta = M\lambda \quad (3.2)$$

where d is the spacing of atomic plane, θ is a half of the diffraction angle of incident X-ray, M is integer and λ is the wavelength of the X-ray. This means that the reflected X-ray intensity is strong when the reflected X-ray by the parallel crystal planes are interfered constructively as shown in Figure. 3.5. The XRD instrument (D8 Discover: Bruker AXS Inc.), consists of three basic elements, an X-ray source, a sample holder and a scintillation counter as shown in Figure. 3.6. The wavelength of the emitted X-ray is Cu K_α radiation ($\lambda = 0.15406$ nm). In this study, 2θ - ω scan was employed which changes θ and ω simultaneously maintaining the relation $\theta - \omega = \text{constant}$ and find the proper angle that meets Bragg's law. By using this technique, the c-axis lattice constant of the thin films under different growth conditions are obtained. The domain size in the film is evaluated from the full-width half maximum (FWHM) of the 2θ - ω peaks, which is one of the most important criteria of crystalline quality, by using Scherrer's equation

$$D = \frac{K\lambda}{B \cos \theta} \quad (3.3)$$

where D is crystal domain size and K is Scherrer constant usually around 0.94 [15].

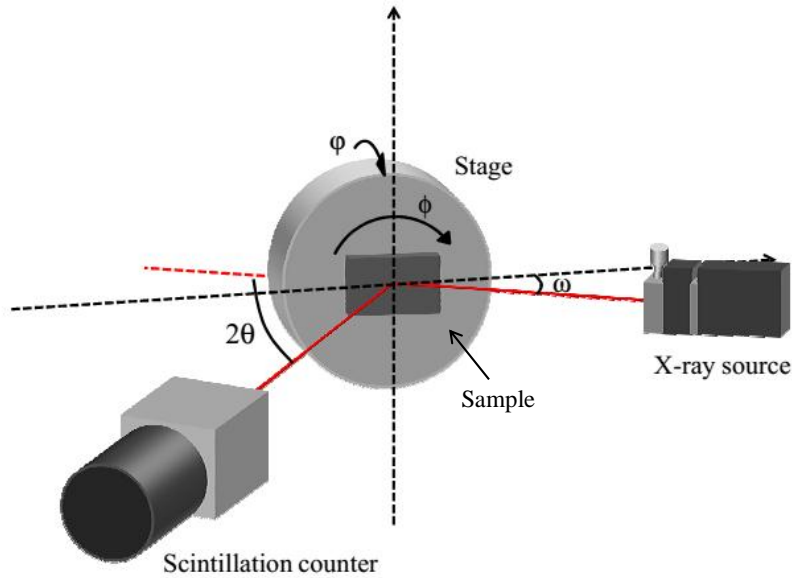


Figure. 3.6 The X-ray diffraction measurement system.

3.4. X-ray reflectivity

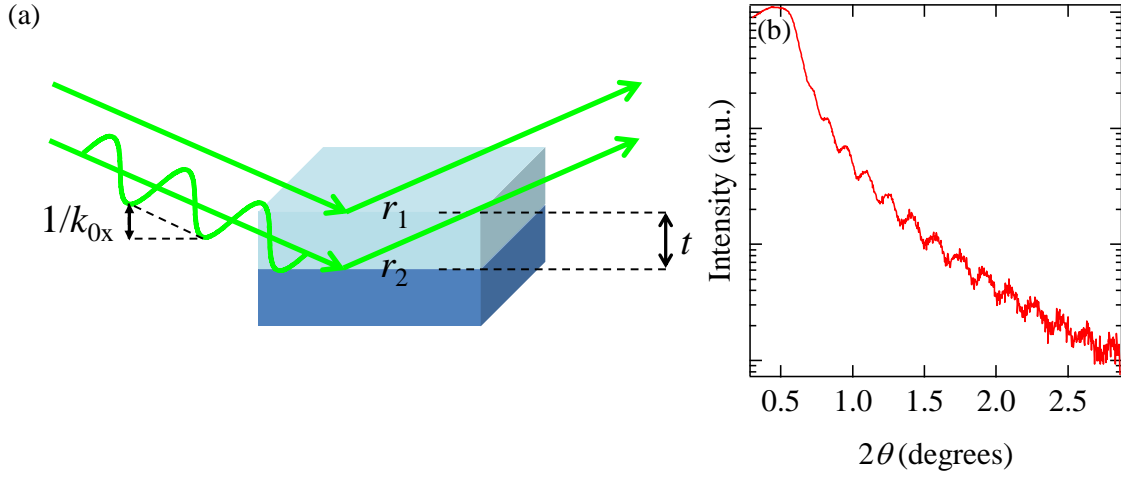


Figure. 3.7 (a) A schematic of interference in XRR measurement. (b) XRR of AgTaO_3 (52 nm)/ Nb:SrTiO_3 (100).

Accurate thickness measurement is always important for thin film samples. X-ray reflectivity (XRR) is a suitable technique for several tenths nm thick films grown by PLD where atomically flat surfaces and interfaces are readily obtained. In a reflectivity curve, clear intensity oscillations can be observed when constructive interference occurs between the x-rays reflected from the upper and lower interfaces. This has the same origin as thin film interference fringes observed in optical reflectance and transmittance measurements. The amplitude of the reflection strongly depends on the reflectivity of the interface which is determined by the refractive indices above and below the boundaries as well as the interface roughness. Assuming a single layer grown on a semi-infinite substrate, the reflectivity is described as

$$R = \left| \frac{r_1 + r_2 \exp(-2ik_{0x}t)}{1 + r_1 r_2 \exp(-2ik_{0x}t)} \right|^2 \quad (3.4)$$

where r_1 and r_2 are the Fresnel reflectivity coefficients of the free surface and the substrate interface, respectively, k_{0x} is the vertical component of the wave vector of the beam transmitted through the layer and t is the layer thickness as shown in Figure. 3.7 (a). From this formula it follows that the intensity maxima appear whenever $\exp(-2ik_{0x}t) = 1$. This means that at angle positions α_{im} satisfying the following equation will show maximum intensity,

$$2t\sqrt{\sin^2 \alpha_{\text{im}} - \sin^2 \alpha_c} = M\lambda . \quad (3.5)$$

where α_c is the critical angle of total external reflection of the layer defined as $\sin \alpha_c = \sqrt{2(1-N)}$ where N is the layer refractive index. Assuming the incident angle is sufficiently small enough to meet $\sin \alpha_{\text{im}} \approx \alpha_{\text{im}}$, this formula can be approximated to:

$$\alpha_{\text{im}}^2 - \alpha_c^2 = M^2 \left(\frac{\lambda^2}{2t} \right) \quad (3.6)$$

Figure 3.7 (b) shows an example of clear oscillations observed for XRR data for AgTaO₃ thin film grown on Nb:SrTiO₃.

3.5. Electrical transport measurements

Electrical transport properties of the semiconducting thin films were characterized by temperature dependent resistivity measurements and Hall measurements using four probe methods. Compared with two probe methods, the four probe method has the advantage that the effect of the contact resistance can be ignored if it is small compared to the input impedance of the voltmeter (typically, GΩ range or higher). The samples were wired with Al wires by using an ultrasonic wire bonder (West Bond 74760, HiSOL, Inc.). All transport measurements were performed in a PPMS (Quantum Design, Inc.) down to 2 K in temperature and under magnetic fields up to ± 14 T applied by a superconducting magnet. Hall measurement is a technique from which we can obtain a type, density and mobility of carriers from Hall coefficients when it is combined with inplane resistivity measurements. For a simple metal, where there is only one type of charge carrier (electron), the Hall voltage V_H , which is the potential difference perpendicular to the current flow, given by

$$V_H = \frac{IB}{ned} \quad (3.7)$$

where I is the current across the plate length, B is the magnetic field, d is the thickness of the film, e is the elemental charge, and n is the charge carrier density of the carrier electrons. The Hall coefficient is defined as

$$R_H = \frac{E_y}{j_x B} = \frac{1}{ne} \quad (3.8)$$

where j_x is the current density of the carrier electrons, E_y is the induced electric field

calculated from the V_H divided by the distance of electrodes measuring Hall voltage. As a result, Hall measurement combined with inplane resistivity measurement is useful to measure the carrier density and mobility.

3.6. Characterization technique of vertical transport

In order to demonstrate the band alignment tuning, Schottky junctions consisting of simple metals and oxide n-type semiconductors are employed as model systems in this study. In particular, we focus on tuning the Schottky barrier height (SBH). There are two advantages for using Schottky junctions. First, its band diagram is simple because there is almost no band bending in the metal side. Second, various techniques are available to characterize the SBH. In this Section, the three techniques to characterize the band alignment will be introduced.

3.6.1. Current-voltage measurement

Current-voltage (I - V) measurement is the most commonly used technique to characterize the SBH of metal-semiconductor junctions. The example of I - V curve is shown in Figure. 3.8 [17]. Assuming the dominant charge transfer across the interface is thermionic emission, which originates from the electrons with kinetic energy higher than the SBH at the interface, the I - V characteristic is expressed by the thermionic emission model.

$$j = j_{ss} \left[\exp\left(\frac{eV}{k_B T}\right) - 1 \right] \quad (3.9)$$

$$j_{ss} = A^* T^2 \exp\left[-\frac{e\Phi_b}{k_B T}\right] \quad (3.10)$$

$$A^* = \alpha \frac{m_n e k_B^2}{2\pi\hbar^3} \quad (3.11)$$

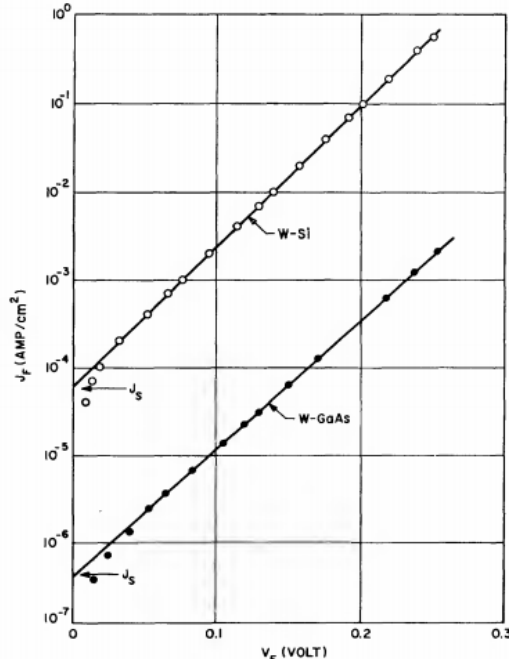


Figure. 3.8 Examples of forward bias I - V curve of W/Si and W/GaAs junctions [17].

where V is the applied bias, T is the temperature, Φ_b is the SBH of the given junction, m_n is the effective mass of the electron in the n-type semiconductor. A^* is called a Richardson constant which includes an empirical factor α that accounts for deviation from the ideal thermionic emission theory. According to Crowell and Sze, $\alpha \sim 0.65$ for Si [18].

SBH is obtained by fitting I - V curve of Schottky junction by this thermionic emission model. However, there are several requirements to use this formula to calculate. First, this formula assumes that an external voltage drop is primarily across the metal semiconductor interface. In highly resistive low mobility and carrier density semiconductor, the current through the Schottky barrier may be limited more by processes of diffusion and drift in the space charge region rather than by the barrier at the metal semiconductor interfaces. Under such conditions, the electron quasi-Fermi level will vary in the depletion

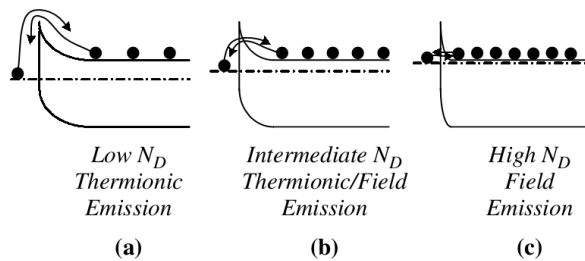


Figure. 3.9 Band diagrams of Schottky junctions when (a) thermionic emission, (b) thermionic field emission, and (c) field emission are the dominant charge transfer mechanism [16].

region, and the thermionic emission model will not be valid. The quantitative criterion of the validity of the thermionic emission model is obtained by comparing the mean free path of electrons with a characteristic distances d_T and λ defined below.

$$d_T = \frac{k_B T}{e F_{\max}} \quad (3.12)$$

where F_{\max} is the maximum electric field at the interface expressed as

$$F_{\max} = \left(\frac{2eN_d V_{bi}}{\epsilon_s} \right)^{\frac{1}{2}} \quad (3.13)$$

and the mean free path λ of the electron given by

$$\lambda = \left(3k_B T m_n \right)^{\frac{1}{2}} \frac{\mu_n}{e} \quad (3.14)$$

where μ_n is the mobility of electron, N_d is the dopant density, V_{bi} is the built in potential which is related to the barrier height by the equation $\Phi_b = eV_{bi} + V_0$ where V_0 is the energy difference of the Fermi level and the conduction band minimum and ϵ_s is the DC dielectric constant of the semiconductor. The thermionic emission model is valid only when $\lambda > d_T$. In the case of Pt/0.1 at % Nb doped TiO₂ junction, $\lambda = 7 \times 10^{-10}$ m and $d_T = 3 \times 10^{-11}$ m meeting this condition.

Second, thermionic emission has to be dominant current flow process at the Schottky junction. There are two more current flow processes competing with thermionic emission which originate from tunneling current. The ratio of the thermionic emission and the tunneling processes are determined by the SBH and the dopant concentration because the depletion layer thickness of Schottky junction is expressed as,

$$W = \left(\frac{2\epsilon_s (V_{bi} - V)}{eN_d} \right)^{\frac{1}{2}} \quad (3.15)$$

where V_{bi} is the built in potential of Schottky junction. the thickness of depletion layer becomes smaller with increase of dopant density in the semiconductor. In Schottky junctions with highly doped semiconductors, the depletion region becomes sufficiently narrow that the electrons can tunnel through the barrier near the top, where the barrier width is thin. Therefore, the electrons with the kinetic energy less than the barrier height start to contribute to the current across the interface. This process is called thermionic field emission. In degenerate semiconductors, even the electrons near the Fermi level can tunnel through the barrier, which is called field emission. The band diagrams for the three different

cases are summarized in Figure. 3.9. In order to judge the dominant contribution of the current, a parameter E_{00} defined as

$$E_{00} = \frac{e\hbar}{2} \left(\frac{N_d}{m_n \varepsilon_s} \right)^{\frac{1}{2}} \quad (3.16)$$

is compared with $k_B T$. When E_{00} becomes much larger than $k_B T$, field emission is dominant and when they are comparable, thermionic field emission is dominant. Only when $k_B T \gg E_{00}$, thermionic emission model is valid. In the case of TiO_2 whose carrier density reaches $1 \times 10^{19} \text{ cm}^{-3}$, E_{00} and $k_B T$ become comparable using the $m_n = m_e$ which is the free electron mass and $\varepsilon_s = 30 \varepsilon_0$ [19]. The I - V characteristic of thermionic field emission is given by the following equation.

$$j = \frac{A^* T \sqrt{\pi E_{00} (\Phi_b - eV - V_0)}}{k_B \cosh\left(\frac{E_{00}}{k_B T}\right)} \times \exp\left(\frac{-V_0}{k_B T} - \frac{\Phi_b - eV - V_0}{E_{00}} \tanh\left(\frac{E_{00}}{k_B T}\right)\right) \quad (3.17)$$

Thus, an ideality factor becomes larger as E_{00} increases and a SBH obtained by the thermionic emission model becomes smaller than the actual barrier height.

Third, the inplane distribution of the SBH has to be uniform since I - V characteristic is sensitive to spatial potential fluctuation at the interface. This is explained by considering the I - V characteristic of parallel diodes with different SBHs. When a

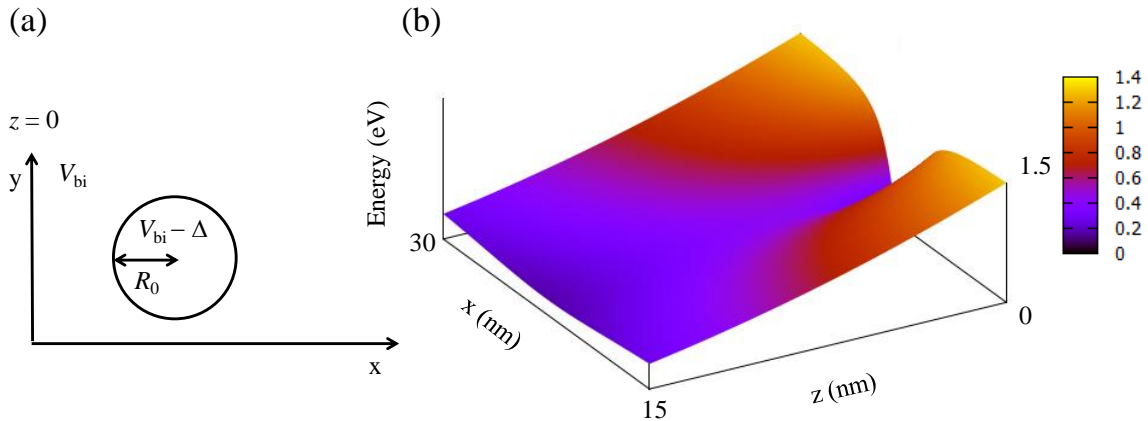


Figure. 3.10 (a) The boundary condition at the interface between a metal and a semiconductor ($z = 0$) projected onto the plane of the interface. (b) The calculated potential profile using equation (3.19) using $R_0 = 2 \text{ nm}$, $W = 30 \text{ nm}$, $\Delta = 0.8 \text{ eV}$, $V_{bi} = 1.5 \text{ V}$.

forward bias is applied to this circuit, the I - V characteristic is always governed by the region with the smallest SBH.

This effect is discussed in detail by considering the Schottky junction having circularly-shaped patches with a smaller barrier height embedded in a host of higher barrier height [20]. The schematics of the boundary condition of the junction is shown in Figure. 3.10 (a). In this model, the boundary condition at the metal semiconductor interface is described by the following formula

$$\phi(x, y, 0) = eV_{\text{bi}} + \Delta(x, y) \quad (3.18)$$

where ϕ is the conduction band minimum of the semiconductor, Δ is the local difference between the high and low SBHs. Coordinates are defined so that z is perpendicular to the interface. The conduction band minimum of the semiconductor at an infinite distance is defined as $\phi(-\infty) = 0$. Here, we treat the potential due to the presence of the SBH inhomogeneity as a perturbation. The local potential change can be regarded as a variation of interface dipole moment per area given by $2\varepsilon_s\Delta(x, y)$, since it satisfies the boundary condition of Eq. (3.18). From this dipole approximation, the potential at a location (x, y) in the depletion layer is approximately described by

$$\begin{aligned} \phi(x, y, z) = eV_{\text{bi}} \left(1 - \frac{z}{W}\right)^2 + \\ \iint dx_1 dy_1 \frac{z\Delta(x, y)}{2\pi[z^2 + (x_1 - x)^2 + (y_1 - y)^2]^{3/2}} \end{aligned} \quad (3.19)$$

Assuming the local variation of the SBH is circular shape and its diameter R_0 is much smaller than the depletion layer thickness W which is called as pinched off, the potential around the patch, except near the core of the variation is given by

$$E_{\text{CBM}}(x, y, z) = eV_{\text{bi}} \left(1 - \frac{z}{W}\right)^2 - \frac{eV_{\text{bi}}\Gamma^3 zW^2}{(x^2 + y^2 + z^2)^{1.5}} \quad (3.20)$$

where Γ is a dimension less parameter which is a criteria of a strength of a given patch defined as

$$\Gamma = \left(\frac{R_0^2 \Delta}{4eW^2 V_{\text{bi}}}\right)^{1/3} \quad (3.21)$$

The calculated potential around the patch is displayed in Figure. 3.10 (b) for parameters $R_0 = 2$ nm, $W = 30$ nm, $\Delta = 0.8$ eV, $V_{\text{bi}} = 1.5$ V. Applying the thermionic emission theory to this

system, the effective barrier height (Φ_{Beff}) and the ideality factors (n_{ideal}) in I - V measurements are obtained as following.

$$\Phi_{\text{Beff}} = \Phi_{\text{B}}(1 - 3\Gamma) \quad (3.22)$$

$$n_{\text{ideal}} = 1 + \Gamma \quad (3.23)$$

These two equations indicate that applying the thermionic emission model to I - V curves of inhomogeneous junctions gives a smaller SBH value than the averaged SBH and an ideality factor larger than unity.

3.6.2. Capacitance voltage measurement

Measuring the depletion capacitance of Schottky diode is also widely used to evaluate the SBH. Experimentally, the procedure involves application of DC bias voltage across the interface while measuring the impedance with an AC voltage superimposed. This technique is less sensitive to small variation of SBH at the interface compared with I - V measurement because the diode with the smallest barrier height dominates the I - V characteristic but the barrier height with the largest contact area dominates the capacitance measurement. Generally, a SBH measured by I - V is smaller than that is estimated from V_{bi} obtained by capacitance voltage measurement [21]. The capacitance per unit area of a Schottky diode is given by

$$C = \sqrt{\frac{q\epsilon_s N_{\text{D}}}{2(V_{\text{bi}} - V - k_{\text{B}}T/q)}} \quad (3.24)$$

Experimentally, V_{bi} is obtained by the voltage intercept of a linear extrapolation of $1/C^2$ vs. voltage as shown in Figure. 3.11.

In order to obtain V_{bi} correctly, there are several requirements. First, the uniform doping concentration is needed. This is confirmed by the voltage independent derivative of C^{-2} . Second, the impedance originated from any electrical elements connected in series with the depletion capacitor has to be negligibly small. In this study, the capacitance of the oxide dipole is always estimated from the thickness and the dielectric constant of the dipole layer material to make sure its impedance is negligibly small. Third, the leakage of the depletion capacitor should be sufficiently small. This is estimated from the dissipation defined as the ratio of the real part and the imaginary part of the impedance. Assuming the Schottky junction can be regarded as a parallel circuit of a capacitor (C_{p}) and a resistor (R_{p}), large dissipation value corresponds to low R_{p} . This results in the resistive impedance overwhelming the capacitive impedance, and the C_{p} value gets lost in the noise.

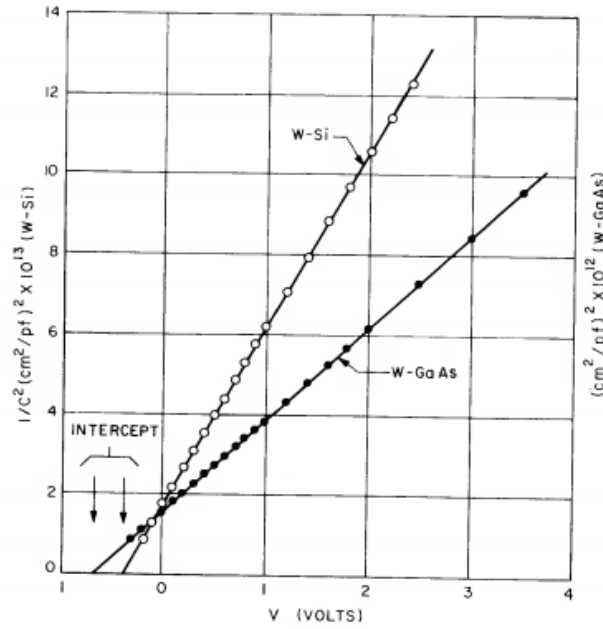


Figure. 3.11 Capacitance voltage measurements of W/Si and W/GaAs Schottky junctions [17].

3.6.3. Internal photoemission

Internal photoemission (IPE) is one of the most reliable techniques to determine the SBH [22]. The principle of IPE owes to the photocurrent through the Schottky junction due to optically excited carriers from the metal which can surmount the barrier. The barrier height is determined by measuring the spectral response of the photocurrent.

The photocurrent is calculated by assuming that the quantum efficiency is proportional to the number of electrons with kinetic energy normal to the interface which is enough to surmount the potential barrier after photo-excitation. In this theory, all the absorbed photon energies are converted to the kinetic energy of the electrons normal to the interface. The parabolic bands of both the semiconductor and the metal are assumed as shown in Figure. 3.12. The z -axis is always chosen perpendicular to the interface of the junction. Additionally, translational invariance of the potential acting upon the carriers was assumed. Hence, the carrier momentum parallel to the interface is assumed to be conserved. The condition for electron injection from metal to semiconductor is

$$\frac{p_z^2 + p_x^2 + p_y^2}{2m_n} > \Phi_B + \frac{p_x^2 + p_y^2}{2m_m} \quad (3.25)$$

where m_n and m_m is the effective mass of electron in the semiconductor and the metal, p_x, p_y, p_z are the x, y and z components of the momentum. When $m_n < m_m$, the number of electron per unit volume is calculated from the following formula.

$$Y \propto (\hbar\omega - \Phi_B)^2 \quad (3.26)$$

where Y is photoyield which is defined as the photocurrent per photons and ω is the wavelength of the excitation light. The SBH is obtained by the photon energy intercept from a linear extrapolation of square root of Y as shown in Figure. 3.13. The basic experimental configurations are summarized in Figure. 3.14. A 300 W Tungsten-Halogen

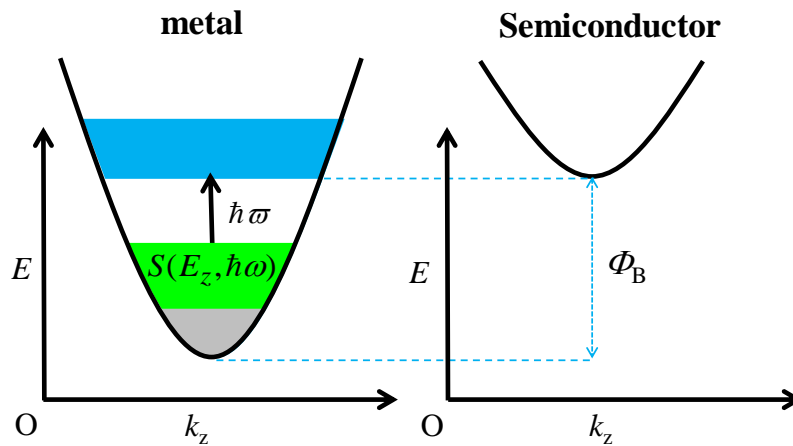


Figure. 3.12 The band diagram of metal semiconductor interface.

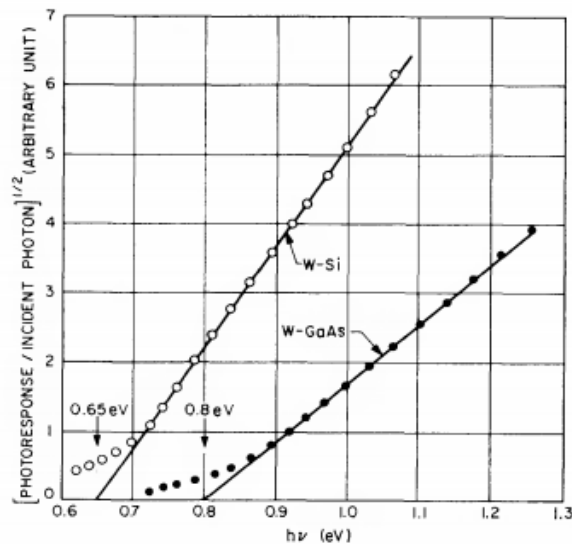


Figure. 3.13 IPE data of W/Si and W/GaAs Schottky junctions. Solid lines are linear fittings to the square root of the photoyield [17].

lamp was utilized as a standard light source covering from UV to IR range. The output wavelength was controlled by a grating monochromator which was coupled to an optical fiber. Long-pass filters were utilized to cut the higher-order harmonics from the gratings. The light was focused onto a circularly-shaped Schottky electrodes with typical diameter of several hundred micrometers using a microscope objective lens. Lock-in amplifier synchronized with an optical chopper was utilized to measure the photocurrent. The uniqueness of IPE is that the barrier height can be measured even without application of external voltage unlike I - V and C - V , probing the junction in equilibrium state.

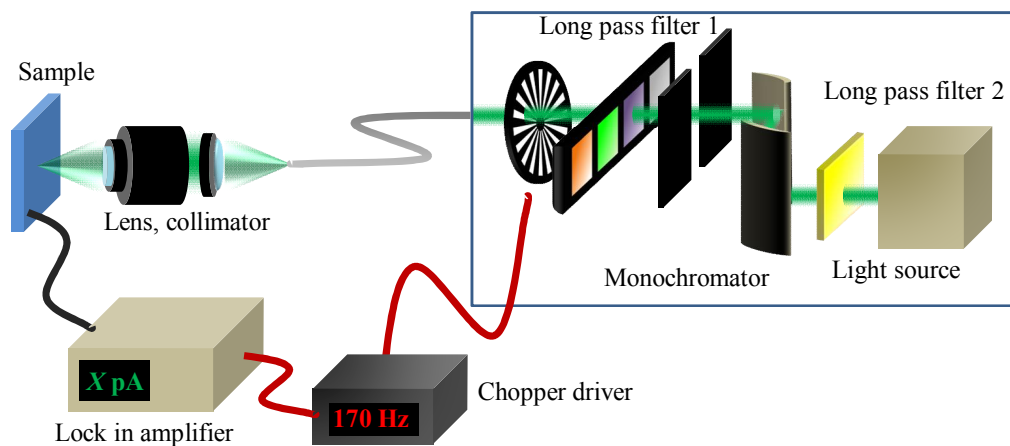


Figure. 3.14 The experimental setup of internal photoemission.

3.7. Bibliography

- [1] H. Koinuma, H. Nagata, T. Tsukahara, S. Gonda and M. Yoshimoto, Appl. Phys. Lett. **58**, 2027 (1991).
- [2] M. Watamori, K. Oura and T. Nakamura, J. Vac. Sci. Technol. A **13**, 1293 (1995).
- [3] A. Miotello and R. Kelly, Appl. Phys. A **69**, S67 (1999).
- [4] A.A. Puretzky, D.B. Geohegan, K.G.E. Jellison Jr. and M.M. McGibbon, Appl. Surf. Sci. **859**, 96 (1996).

- [5] D. B. Geohegan, *Thin Solid Films* **220**, 138 (1992).
- [6] S.K. Hau, K.H. Wong, P.W. Chan and C.L. Choy, *Appl. Phys. Lett.* **66**, 245 (1995).
- [7] J. Sudijono, M.D. Johnson, C.W. Snyder, M.B. Elowitz and B.G. Orr, *Phys. Rev. Lett.* **69**, 2811 (1992).
- [8] S.Clark and D.D. Vvedensky, *Phys. Rev. Lett.* **58**, 2235 (1987).
- [9] W.Braun, B. Jenichen, V.M. Kaganer, A.G. Shtukenberg, L. Daweritz and K.H. Ploog, *Surf. Sci.* **525**, 126 (2003).
- [10] I.K. Robinson and D.J. Tweet, *Rep. Prog. Phys.* **55**, 59 (1992).
- [11] E. Vasco and J.L. Sacedon, *Phys. Rev. Lett.* **98** 036104 (2007).
- [12] H. Sankur, W. J. Gunning, J. Denatale and J. F. Flintoff, *J. Appl. Phys.* **65**, 2475, (1989).
- [13] N. Joyce, D. Norton, J.H. Neave, B.A. Joyce, P.J. Dobson and N. Norton, *Appl. Phys. A* **31**, 1 (1983).
- [14] C. K. Ong and S. J. Wang, *Appl. Surf. Sci.* **185**, 47 (2001).
- [15] A. Patterson, *Phys. Rev.* **56**, 978 (1939).
- [16] R. T. Tung, *Mater. Sci. Eng. R* **35**, 1 (2001).
- [17] C.R Crowell, J.C. Sarace, and S. M. Sze, *Trans. Met. Soc. AIME*, 233, 478 (1965).
- [18] C. R. Crowell, *Solid-State Electron.* **8**, 395 (1965).
- [19] H. Tang, K. Prasad, R. Sanjinès, P. E. Schmid, and F. Lévy, *J. Appl. Phys.* **75**, 2042 (1994).
- [20] R. T. Tung, *Appl. Phys. Lett.* **58**, 2821 (1991).
- [21] Y. P. Song, R. L. Van Meirhaeghe, W. H. Laflère, and F. Cardon, *Solid-State Electron.* **29**, 633 (1986).

[22] L. S. Yu, Q. J. Xing, D. Qiao, S. S. Lau, K. S. Boutros, and J. M. Redwing, *Appl. Phys. Lett.* **73**, 3917 (1998).

Chapter 4.

Fabrication of high quality

LaAlO₃/TiO₂/LaAlO₃ heterostructure

4.1. Introduction

We aimed to grow an epitaxial LaAlO₃ layer on anatase TiO₂ (001) to demonstrate the band alignment tuning at the interface of a polycrystalline metal and a binary oxide. There are two difficulties to fabricate the LaAlO₃/TiO₂/LaAlO₃ (100) heterostructure. The first problem is crystalline quality degradation of TiO₂ upon growth of LaAlO₃ capping layers [1,2]. When heterointerfaces are formed, there are various phenomena that can lead to atomically non-abrupt interfaces, such as cation intermixing [3], electronic reconstruction [4], encapsulation [5] and chemical reactions [6]. In order to observe band offset change induced by electrostatic dipoles, crystalline quality variations, which can also affect the band alignment, caused by the deposition of the dipole layer has to be suppressed. Thus, we will establish the growth conditions for LaAlO₃ where no degradation of TiO₂ occurs by understanding its mechanism.

The second problem is (1 × 4) reconstruction of anatase TiO₂ (001) surface that occurs for the thin films grown under high vacuum. Atomic structure of unreconstructed TiO₂ surface and the reconstructed TiO₂ surface predicted by first principles calculations [7] and STM studies [8] are shown in Figure. 4.2. Owing to the lattice mismatch, the epitaxial growth of an oriented perovskite oxide on the reconstructed surface may be unstable.

Oriented single crystal perovskite oxides may be crucial to obtain dipole effect because they are regarded as an alternate stacking of positively and negatively charged layer only in specific crystallographic orientations. Therefore, we will establish a surface treatment technique to stabilize unreconstructed TiO_2 (001) surface which is lattice matched with a LaAlO_3 (100) surface.

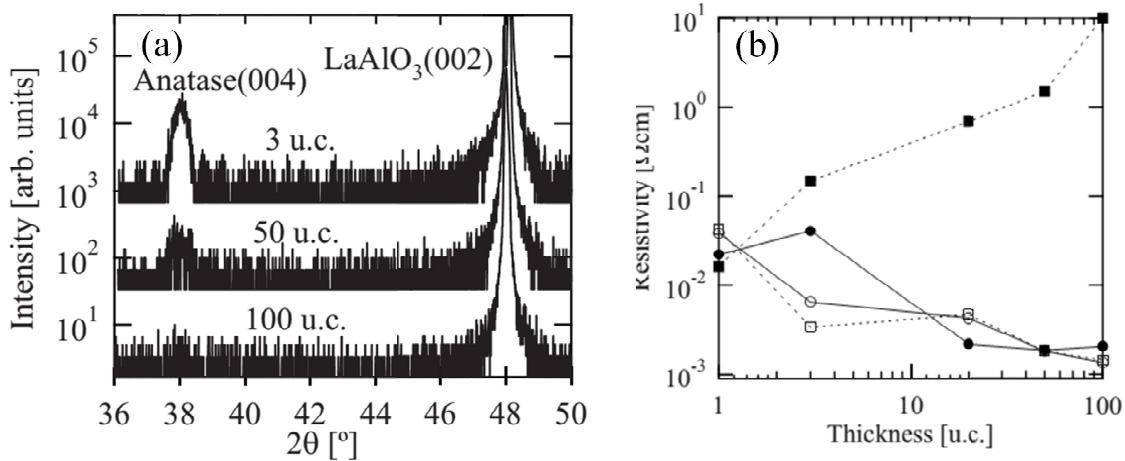


Figure. 4.1 (a) XRD patterns for a TiO_2 film capped by 3, 50, and 100 u.c. LaAlO_3 layers. (b) The overlayer thickness dependence of the resistivity of 16 nm thick TiO_2 for LaTiO_3 open symbol and LaAlO_3 closed symbol at 10 K square and dotted line and 300 K circle and line [1].

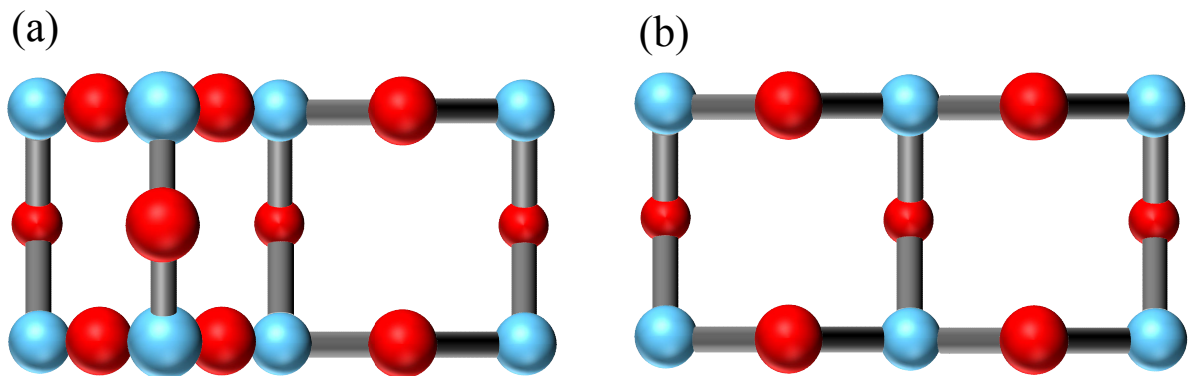


Figure. 4.2 Atomic structures of (a) (1×4) reconstructed and (b) unreconstructed anatase TiO_2 (001) surface suggested from previous researches [7].

4.2. Experimental

Anatase TiO₂ films were epitaxially grown on LaAlO₃ (100) substrates by using PLD with a KrF excimer laser imaged onto a spot size of 3.01 mm². The growth sequence and observed reflection high energy diffraction (RHEED) patterns of a LaAlO₃ (100) substrate and as-grown anatase TiO₂ are shown in Figure. 4.3 (a)-(c). Prior to the deposition, the substrates were annealed at 900 °C at an oxygen partial pressure of 1×10⁻⁶ Torr to obtain atomically flat surfaces with single termination [9]. The 40 nm thick TiO₂ thin films were deposited by ablating a polycrystalline target at substrate temperature and oxygen partial pressure of 700 °C and 1×10⁻⁵ Torr, respectively. These thermodynamic conditions has been already optimized previously [10], and are similar to those reported for high quality epitaxial anatase TiO₂ thin films elsewhere [11,12]. In the previous study, the Hall carrier density was an important criterion for the crystalline quality variation induced by LaAlO₃ deposition. Therefore, before the LaAlO₃ deposition, the number of oxygen vacancies that emit free electrons in anatase TiO₂ should be minimized to sensitively detect the crystalline quality change. Previously, we found that the growth rate strongly influences the number of oxygen vacancies induced in TiO₂ [13]. In the case of pulsed laser deposition, the laser fluence varies the amount of the ablated species per shot and the repetition rate changes the interval between each pulse. The growth rate was regulated to 0.007 nm/s by setting the repetition rate to 1 Hz and the laser fluence to 0.66 J/cm². RHEED was used to confirm the (1 × 4) reconstructed surfaces during the growth. In the case of anatase TiO₂, one period of the RHEED oscillation corresponds to half of a unit cell [14]. The evaluated thickness showed good match with X-ray reflectivity measurement taken after the growth.

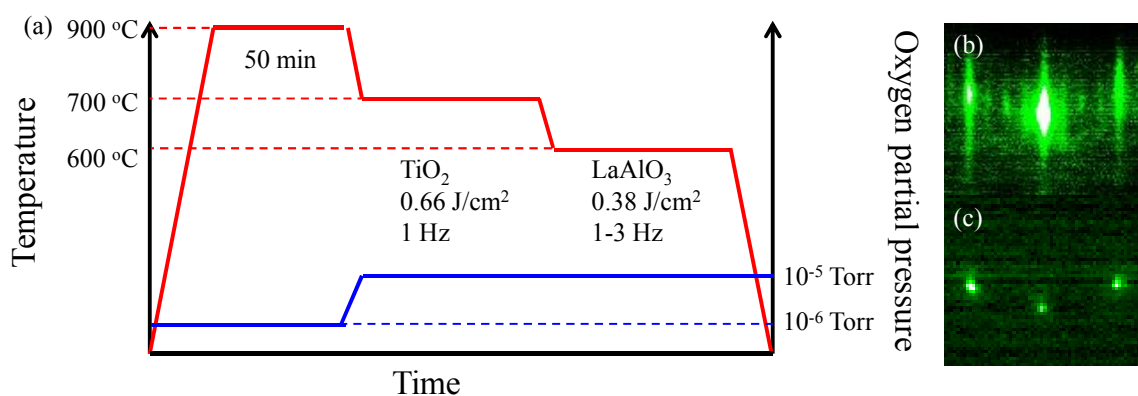


Figure. 4.3 (a) The growth sequence of LaAlO₃/TiO₂/LaAlO₃ (100) heterostructure. (b) RHEED patterns of as-grown anatase TiO₂ thin film and (c) annealed LaAlO₃ (100) substrate.

The LaAlO₃ capping layer was grown on anatase TiO₂ by ablating LaAlO₃ single crystal substrate. The oxygen partial pressure, the laser fluence and the repetition rate of LaAlO₃ growth was changed within the range of 10⁻⁵ to 10⁻⁶ Torr, 0.28 to 0.58 J/cm² and 0.6 to 3 Hz, respectively. Although the LaAlO₃ thickness required for the dipole effect is few u.c., 16 nm LaAlO₃ capping layer was grown on the TiO₂ to characterize the structural properties. In addition, it was previously reported that the crystalline quality degradation of TiO₂ induced by LaAlO₃ capping layer is known to be more significant as the LaAlO₃ capping layer becomes thicker [1]. The structural properties of the fabricated films were characterized by XRD. Raman scattering technique was utilized to detect the in-plane crystalline phase domains. Temperature dependent Hall measurements were utilized to study the number of oxygen vacancies in the TiO₂.

4.3. Anatase TiO₂ thin films growth

First, we'll introduce the brief history of the growth of anatase TiO₂ thin films. The single crystal of anatase TiO₂ has been difficult to grow because it is a metastable phase. Figure 4.4 (a) shows the calculated Gibbs free energy at atomospheric pressure [15]. The rutile phase is more energetically stable independent of temperature. In 2001, Yamamoto *et al.*, demonstrated that the pulsed laser deposition technique can be utilized to grow single crystalline anatase TiO₂ on lattice matched perovskite oxide substrate LaAlO₃ [16]. This result provided an ideal platform to study the basic physical/chemical properties of anatase TiO₂ single crystal leading a discovery of transparent conductivity [17] and room temperature ferromagnetism [18] induced by transition metal doping.

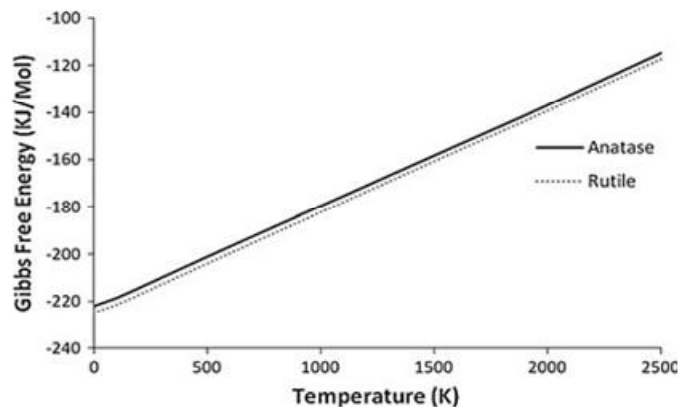


Figure 4.4 (a) Gibbs free energy of anatase and rutile phase in air [15].

With expanding interest for electronic properties of anatase TiO₂, the importance of controlling oxygen vacancies in anatase TiO₂ has been more significant since oxygen vacancies can influence the physical properties in various ways. First, they behave as donor dopants emitting two electrons because the energy level of the oxygen vacancy is very close to the conduction band minimum of TiO₂ [19]. Second, oxygen vacancies are ionized impurities that degrade the electron mobility. Generally, the number of oxygen vacancies in oxides can be easily tuned by changing the thermodynamic conditions during the thin film growth [20]. However, in the case of TiO₂, anatase to rutile phase transition is easily induced by small variations in the growth temperature and the oxygen partial pressure [21]. Previously, we have established a technique to control the number of oxygen vacancies by the modulation of the growth rate [13]. The number of electrons, which corresponds to twice of the number of oxygen vacancies, were continuously tuned by the growth rate accompanied by the mobility change originated from ionized impurity scattering [22] (Figure. 4.5 (b),(c)). This trend is consistent with the growth rate dependence of critical excitation power in photoluminescence at which the photoluminescence intensity from oxygen vacancies are saturated. Associated with a systematic change in the number of oxygen vacancies, the clear insulator to metal transition was observed in temperature dependent resistivity as shown in Figure. 4.5 (a). This behavior is explained by Mott criterion which describes the critical dopant density of the metal to insulator transition in semiconductors. Mott criterion is expressed as

$$n_c = \frac{1}{(4a_H)^3} \quad (4.1)$$

$$a_H = \frac{4\pi\varepsilon_s\hbar^2}{m_n e^2} \quad (4.2)$$

where a_H is the effective bohr radius, m_n is the effective mass of the electrons, and ε_s is the dielectric constant of semiconductor. The calculated Mott criterion of anatase TiO₂ is $2 \times 10^{18} \text{ cm}^{-3}$ using the values of m_n equal to the free electron mass and the relative dielectric constant of 30 [23] which is in the range of the number of oxygen vacancies we tuned. Although the number of oxygen vacancies are tuned by two orders of magnitude, the XRD pattern of anatase TiO₂ (004) remained the same. There was no obvious change in surface morphology either. These results indicate that the successful control of the number of oxygen vacancies utilizing oxidization kinetics by the growth rate.

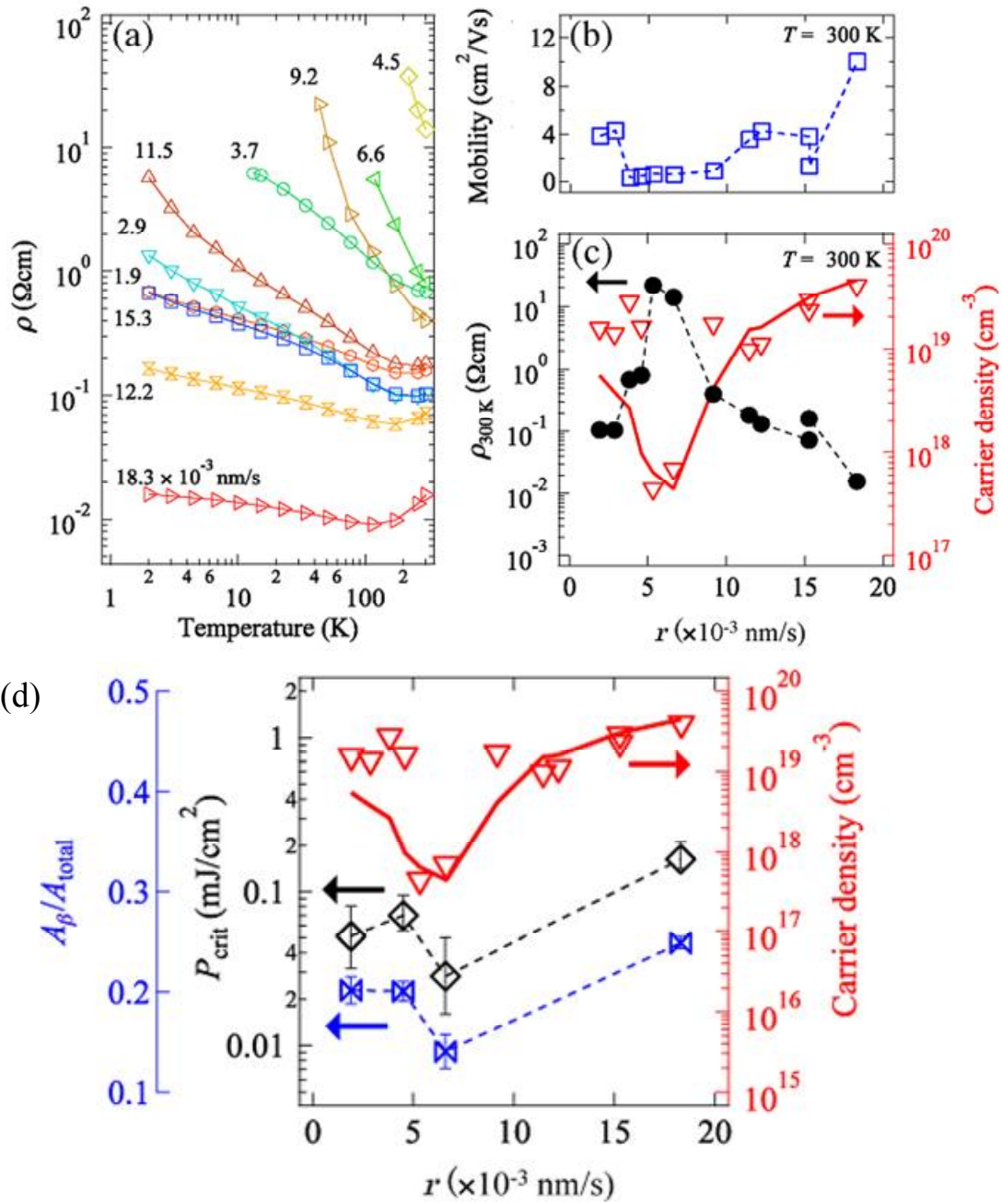


Figure. 4.5 (a) ρ - T curves of anatase TiO₂ for various growth rates (r). Numbers correspond to the growth rate ($\times 10^{-3}$ nm/s). (b) Hall mobility, (c) carrier density and resistivity at $T = 300$ K as a function of the growth rate. The dashed lines are guides for the eye. The solid line gives the calculated carrier density from the kinetic simulation. (d) Growth rate dependences of carrier density and critical excitation power where defect mediated luminescence is saturated [13].

4.4. Growth parameters for LaAlO₃ capping layer and crystalline quality of TiO₂

In the following section, we discuss the optimization of the growth parameters of LaAlO₃ capping layer on top of anatase TiO₂. TiO₂ was fabricated under the condition optimized before. First of all, the relationship between crystalline quality of anatase TiO₂ and the three growth parameters, oxygen partial pressure, laser fluence and repetition rate was investigated. The crystalline quality examined by XRD $2\theta - \omega$ scan is summarized in Figure. 4.6. The thickness of the grown LaAlO₃ capping layer was fixed to 40 u.c. which is almost the same thickness as Takahashi's work [1]. Only anatase TiO₂ (004) peak and LaAlO₃ (002) peak were detected in the conditions we employed. Anatase TiO₂ peak intensity decreases under the conditions where oxygen incorporation from the atmosphere is suppressed, which are lower P_{O_2} , faster repetition rate, and higher laser fluence. In the following section, we will focus on the repetition rate dependence which can systematically tune the oxidization kinetic without major influences on the other growth kinetics and thermodynamics. The growth temperature, the oxygen partial pressure and the laser fluence were fixed to 600 °C, 10^{-5} Torr and 0.28 J/cm^2 , respectively.

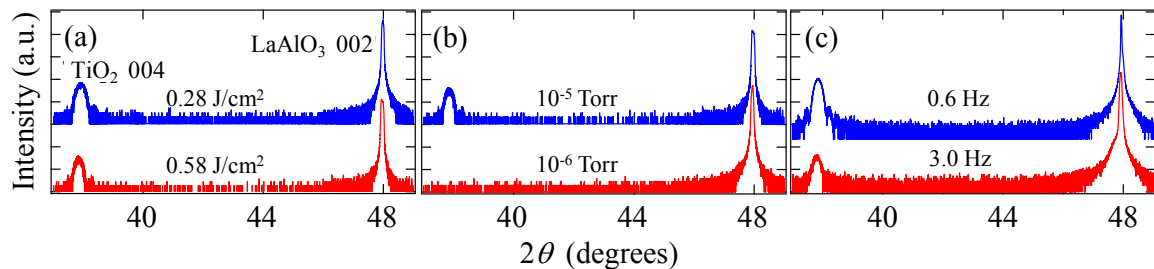


Figure. 4.6 The relation between XRD patterns of LaAlO₃ (40 u.c.)/TiO₂ (40 u.c.)/LaAlO₃ heterostructure and (a) laser fluence, (b) oxygen partial pressure and (c) repetition rate of LaAlO₃ capping layer. The conditions not specified were fixed to the temperature of 600 °C, the oxygen partial pressure of 10^{-5} Torr, the laser fluence of 0.28 J/cm^2 and the repetition rate of 1 Hz.

4.5. LaAlO₃ Repetition rate dependence of anatase TiO₂

X-ray diffraction pattern and Raman spectra of LaAlO₃ (40 u.c.)/TiO₂ 40 (u.c.)/LaAlO₃ (100) fabricated under various LaAlO₃ repetition rates are summarized in Figure. 4.7. The intensity of anatase TiO₂ 004 peak in 2θ - ω scan monotonically decreases with the repetition rate of LaAlO₃ indicating the degradation of the crystalline quality of anatase TiO₂. It should be noted that there were no obvious change of XRD pattern in 0.6 Hz compared with no LaAlO₃ suggesting that high quality anatase TiO₂ were preserved.

Raman spectra showed anatase B_{1g} , A_{1g} , and E_g modes for lower repetition rate samples which correspond to the peaks at 395 cm⁻¹, 515 cm⁻¹ and 636 cm⁻¹, respectively [24]. The small shoulder on the left of A_{1g} peak is originated from E_g mode of LaAlO₃ [25] which mainly comes from substrate because the total volume of the LaAlO₃ capping layer is negligibly small and TiO₂ is transparent for the excitation wavelength as shown in Figure. 4.8 (a) [26]. For 3 Hz case, the sharp anatase peaks disappeared and broad rutile-like peaks showed up. This result suggests that small rutile domains with poor crystallinity exist in the TiO₂ layer which is consistent with the absence of a rutile peak in XRD 2θ - ω scan.

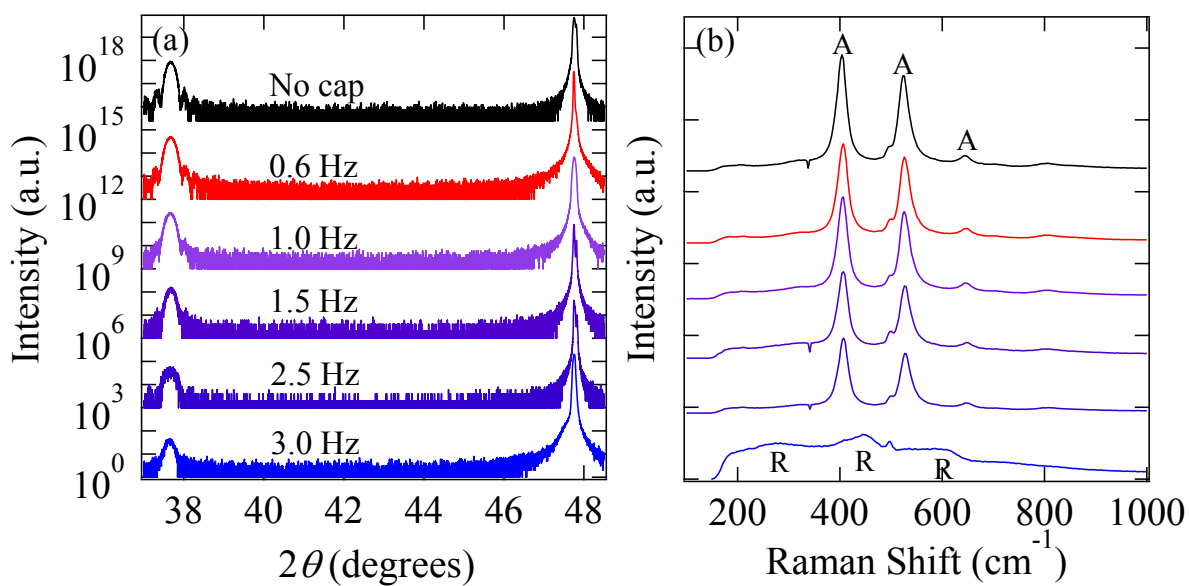


Figure. 4.7 (a) XRD 2θ - ω scan and (b) Raman scattering data of LaAlO₃ (40 u.c.)/TiO₂ (40 u.c.)/LaAlO₃ (100) grown under various repetition rate of LaAlO₃. The Raman scattering peaks originated from anatase and rutile are described as A and R, respectively. The small shoulder on the left of anatase peak at 515 cm⁻¹ corresponds to the phonon mode of LaAlO₃ substrate which was confirmed by measuring bare substrate.

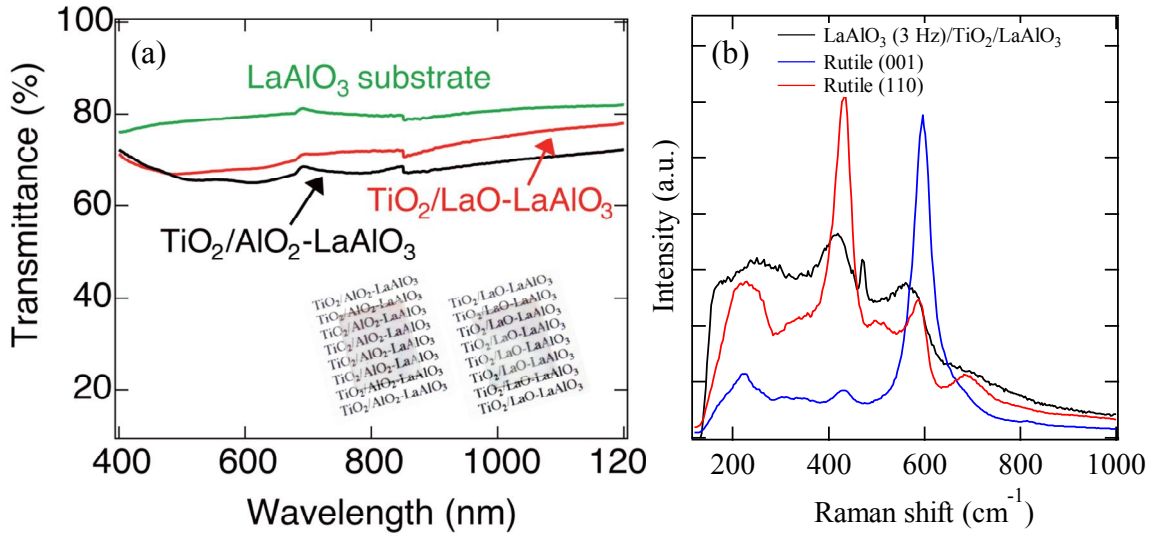


Figure. 4.8 (a) Transmittance spectra for $\text{TiO}_2/\text{AlO}_2\text{-LaAlO}_3$ (100) and $\text{TiO}_2/\text{LaO-LaAlO}_3$ (100) heterostructures and a bare LaAlO_3 (100) substrate. [26]. Inset photographs show the TiO_2 films on $\text{AlO}_2\text{-}$ and LaO- terminated LaAlO_3 substrates (left and right, respectively), placed on top of printed text. Lateral sample size is 10 mm by 10 mm. (b) Raman scattering spectra of $\text{LaAlO}_3/\text{TiO}_2/\text{LaAlO}_3$ (100) with LaAlO_3 capping layer grown under 3 Hz and rutile TiO_2 substrates with (001) and (110) orientation.

In order to determine the crystalline orientation of the rutile phase, Raman data of 3 Hz sample was compared with those of rutile single crystal substrates as shown in Figure. 4.8 (b). Because of the angular dependent cross section, the peak intensity ratio of the three rutile phonon modes depends on the crystalline orientation. The Raman scattering spectra of 3 Hz is similar to that of Rutile (110). Therefore, the (110) orientation of rutile domains are likely to be formed parallel to LaAlO_3 (100).

In order to further understand the origin of the crystalline quality change, electrical transport measurements were performed. Temperature dependent resistivity with various repetition rates is displayed in Figure. 4.9 (a). Clear metal to insulator transition was observed by the growth of LaAlO_3 capping layer. Although 3 Hz sample showed metallic behavior at high temperatures, the resistivity increases abruptly at low temperatures indicating the enhanced scattering by crystalline disorders [22]. Carrier density and mobility obtained from room temperature Hall measurements are displayed in Figure. 4.9 (b). The carrier density monotonically increased with the repetition rate. The carriers are identified as electrons from Hall measurement. Since the activation energy of the carriers calculated from temperature dependent resistivity was 60 meV, the origin of the carriers is

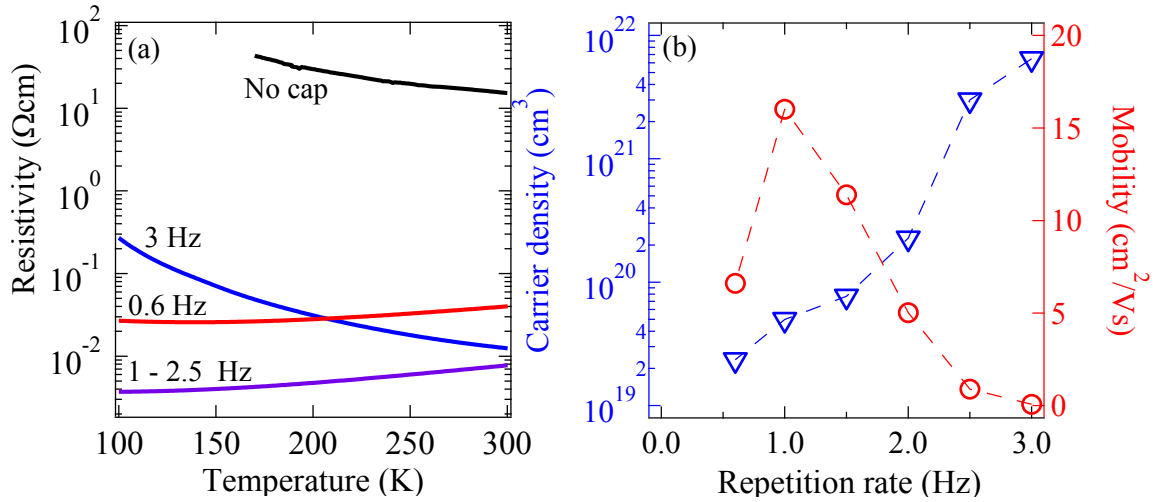


Figure. 4.9 (a) Temperature dependences of electrical resistivity of $\text{LaAlO}_3/\text{TiO}_2/\text{LaAlO}_3$ (100) heterostructure with various repetition rates of LaAlO_3 capping layer. (b) LaAlO_3 repetition rate dependence of carrier density and electron mobility measured by Hall measurement at room temperature and magnetic field of ± 3 T.

dominantly oxygen vacancies [19]. In the 0.6 Hz case, the carrier density was identical to the sample without LaAlO_3 capping indicating that no oxygen vacancies are induced by the LaAlO_3 capping layer at the low repetition rates which is consistent with structural characterizations. The behavior of the mobility change was similar to mobility dependence on dopant density in Nb doped TiO_2 where the major scattering process is grain boundary scattering in diluted case and ionized impurity scattering in heavily doped case [22].

The mechanism of the TiO_2 crystalline quality degradations is explained by the competition of oxygen incorporation from the atmosphere and oxygen extraction from the anatase TiO_2 underneath. It is widely known that the precursors ablated from the oxide target contains reduced elements, such as La, Al and LaO [27]. The precursors are oxidized by the reaction with the oxygen atmosphere on the topmost surface. In the 0.6 Hz case, the topmost surface has enough time to react with the oxygen molecule in the chamber due to the slow growth rate. However, in the 3 Hz case, the deposited layers are covered by the subsequent layers before they are fully oxidized. In order to compensate the oxygen deficiency in the LaAlO_3 , oxygen atoms are extracted from the TiO_2 layer underneath. The driving force of the oxygen extraction is the difference of electron negativities. Since Pauling electron negativity in Al (1.61) in LaAlO_3 is larger than that of Ti (1.54) in TiO_2 , the oxygen atoms can diffuse from TiO_2 to LaAlO_3 . It was also previously reported that the difference in electron negativity is a driving force at heterointerface of transition metal oxides in general [28].

4.6. Surface treatment of anatase TiO₂ (001) surface

Generally, (1 × 4) surface reconstruction occurs at anatase TiO₂ (001) after growth in UHV [9] which could prevent the growth of physically abrupt LaAlO₃/TiO₂ (001) interface due to the mismatch in the lattice symmetry between the reconstructed TiO₂ surface and the perovskite (100) surface. Typical (1 × 4) reconstruction RHEED pattern appeared in the as-grown anatase TiO₂ film as shown in the left image in Figure. 4.10 (a). In order to maintain (1 × 1) unreconstructed TiO₂ (001) surface, the as-grown anatase TiO₂ (001) surface was dosed with water and left in air for 2 hours prior to LaAlO₃ deposition. The water-treated TiO₂ showed (1 × 1) RHEED pattern which was preserved up to 625 °C in $P_{O_2} = 10^{-5}$ Torr above the LaAlO₃ growth temperature of 600 °C as shown in Figure. 4.10 (b). When 40 u.c. LaAlO₃ was grown on a water-treated TiO₂ surface, a clearer streak pattern were obtained from RHEED measurement compared with that on as-grown TiO₂ (Figure. 4.10 (c) and (d)). This result strongly suggests that good lattice match between perovskite oxide and unreconstructed TiO₂ surface is essential for the growth of high quality LaAlO₃ capping layer.

The stabilization by water is explained by the chemical bonding of surface Ti atoms with oxygen atoms since the instability of unreconstructed TiO₂ (001) surface is partially originated from the under-coordinated Ti atoms [29]. In bulk anatase TiO₂, each Ti atoms are coordinated to the six neighboring oxygen atoms via two (long) apical and four (short) equatorial bonds of length 0.1979 nm and 0.1932 nm respectively at 15 K [30].

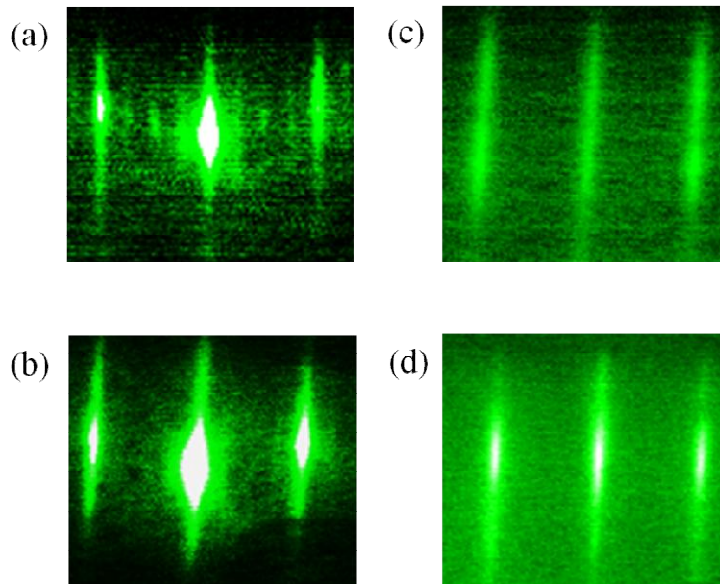


Figure. 4.10 (a) RHEED patterns of as grown and (b) Water treated anatase TiO₂ (001) film. RHEED pattern of LaAlO₃ grown on (c) as-grown and (d) water-treated TiO₂.

However on the surface of TiO_2 , five-fold coordinated or four-fold coordinated Ti atoms are present. The density of such under-coordinated Ti atoms and TiO_2 surface energy for various Ti-coordination are shown in Figure. 4.11 (a)-(c). Because of the high density of five-fold coordinated Ti atoms in anatase (001) surface, surface energy is higher than anatase (101) surface, which is the most stable surface with lowest density of under-coordinated Ti atoms. According to previous theoretical calculations, water molecules dissociatively adsorbs on anatase TiO_2 (001) surface and hydroxyl groups bond with Ti atoms as shown in Figure. 4.11 (d) [31]. According to this proposed atomic structure, Ti atoms are now bonded to six oxygen atoms. Therefore, unreconstructed TiO_2 (001) surface can be stabilized by the water treatment because of the decrease in the under-coordinated Ti atoms.

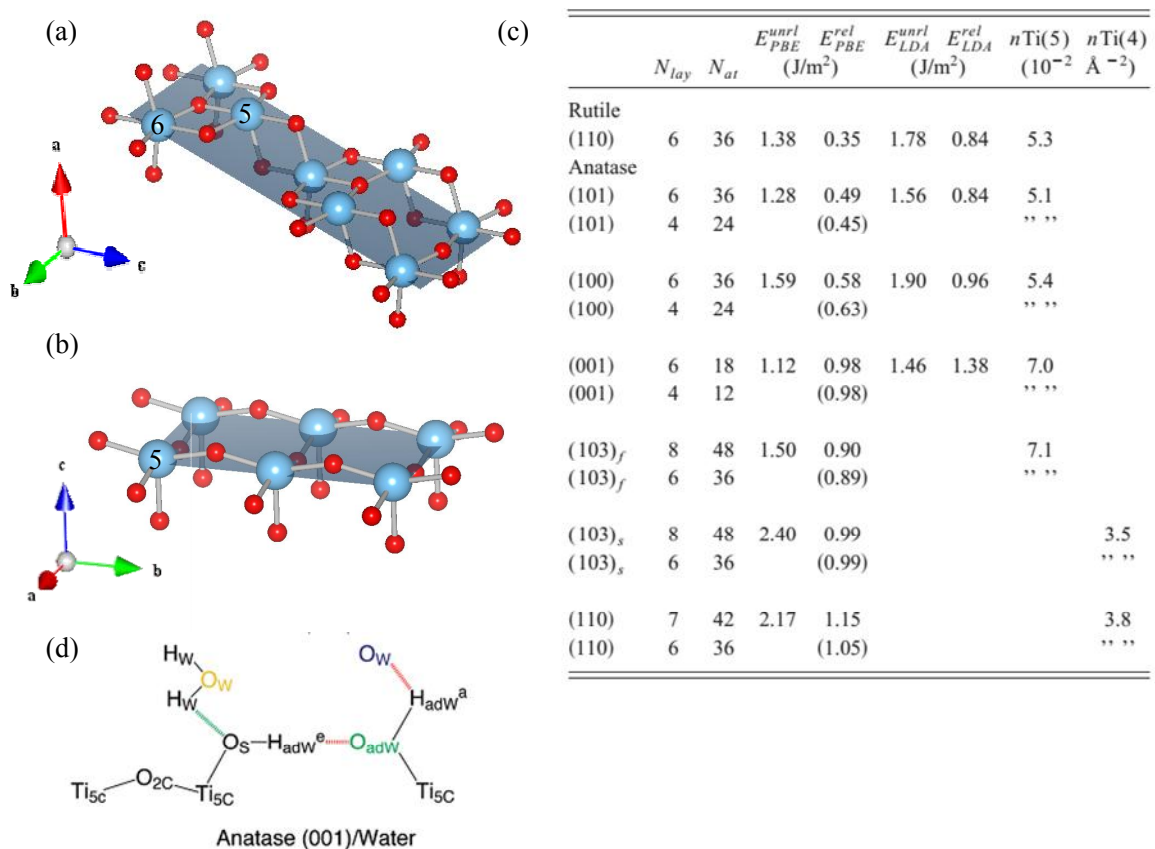


Figure. 4.11 (a) The schematics of atomic structure of anatase TiO_2 (101) surface and (b) (001) surface. The coordination of Ti atoms are described by the number on atoms. (c) Table of formation energies of various TiO_2 surfaces calculated in [29]. (d) Proposed atomic structure of dissociative adsorption of water on TiO_2 (001) surface in [31].

4.7. Conclusion

We aimed to overcome two challenges to fabricate high quality LaAlO₃/TiO₂/LaAlO₃ (100) heterostructure. The mechanism of the degradation of TiO₂ by LaAlO₃ growth was explained by the oxygen extraction from TiO₂ to LaAlO₃ driven by the difference in electron affinities of the cations. This effect is suppressed by the optimization of the repetition rate, controlling the balance of oxygen extraction from TiO₂ and oxygen incorporation from the atmosphere. The (1 × 4) reconstruction of anatase TiO₂ is solved by simple water treatment which decreases the density of under-coordinated Ti atoms by the dissociative water adsorption on the surface of anatase TiO₂ (001). Therefore, it is concluded that the growth condition of high quality LaAlO₃/TiO₂/LaAlO₃ (100) was successfully established.

4.8. Bibliography

- [1] K. S. Takahashi and H. Y. Hwang, *Appl. Phys. Lett.* **93**, 082112 (2008).
- [2] J. Y. Yang, Y. Sun, P. Lv, L. He, R. F. Dou, C. M. Xiong, J. C. Nie, *Appl. Phys. A*, **105**, 1017 (2011).
- [3] L. Qiao, T C Droubay, V. Shutthanandan, Z. Zhu, P. V. Sushko and S A Chambers *J. Phys. Condens. Matter.* **22**, 312201 (2010).
- [4] A. Ohtomo and H.Y. Hwang, *Nature*, **427**, 423 (2004).
- [5] Q.Fu, T. Wagner, S. Olliges, H. D. Carstanjen, *Surf. Rev. Lett.* **2** 109 (1995) 109,
- [6] T. J. Regan, H. Ohldag, C. Stamm, F. Nolting, J. Lüning, J. Stöhr, and R. L. White *Phys. Rev. B* **64**, 214422 (2001).
- [7] M. Lazzeri and A. Selloni, *Phys. Rev. Lett.* **87**, 26 (2001).
- [8] Y. Wang, H. Sun, S. Tan, H. Feng, Z. Cheng, J. Zhao, A. Zhao, B. Wang, Y. Luo, J. Yang,

- and J. G. Hou, *Nat. Commun.* **4**, 2214 (2013).
- [9] M. Murakami, Y. Matsumoto, K. Nakajima, T. Makino, Y. Segawa, T. Chikyow, P. Ahmet, M. Kawasaki, and H. Koinuma, *Appl. Phys. Lett.* **78**, 2664 (2001).
- [10] Y. Nakanishi, Master Thesis Univ. Tokyo (2011).
- [11] M. Kondow and T. Kitatani, *Semicond. Sci. Technol.* **17**, 746 (2002).
- [12] T. C. Kaspar, S. M. Heald, C. M. Wang, J. D. Bryan, T. Droubay, V. Shutthanandan, S. Thevuthasan, D. E. McCready, A. J. Kellock, D. R. Gamelin, and S. A. Chambers, *Phys. Rev. Lett.* **95**, 217203 (2005).
- [13] T. Tachikawa, M. Minohara, Y. Nakanishi, Y. Hikita, M. Yoshita, H. Akiyama, C. Bell, and H. Y. Hwang, *Appl. Phys. Lett.* **101**, 022104, (2012).
- [14] C. K. Ong and S. J. Wang, *Appl. Surf. Sci.* **185**, 47 (2001).
- [15] Dorian A. H. Hanaor • Charles C. Sorrell, *J. Mater Sci* **46**, 855 (2011)
- [16] S. Yamamoto, T. Sumita, Sugiharuto, A. Miyashita, and H. Naramoto, *Thin Solid Films* **401**, 88 (2001).
- [17] Y. Furubayashi, T. Hitosugi, Y. Yamamoto, K. Inaba, G. Kinoda, Y. Hirose, T. Shimada, and T. Hasegawa, *Appl. Phys. Lett.* **86**, 252101 (2005).
- [18] Y. Matsumoto, M. Murakami, T. Shono, T. Hasegawa, T. Fukumura, M. Kawasaki, P. Ahmet, T. Chikyow, S. Koshihara, and H. Koinuma, *Science* **291**, 854 (2001).
- [19] J. M. Sullivan and S. C. Erwin, *Phys. Rev. B* **67**, 144415 (2003).
- [20] M. K. Nowotny, L. R. Sheppard, T. Bak, and J. Nowotny, *J. Phys. Chem. C* **112**, 5275 (2008).
- [21] A. R. Barman, M. Motapothula, A. Annadi, K. Gopinadhan, Y. L. Zhao, Z. Yong, I. Santoso, Ariando, M. Breese, A. Rusydi, S. Dhar, and T. Venkatesan, *Appl. Phys. Lett.*

98, 072111 (2011).

[22] Y. Furubayashi, N. Yamada, Y. Hirose, Y. Yamamoto, M. Otani, T. Hitosugi, T.

Shimada, and T. Hasegawa, *J. Appl. Phys.* **101**, 093705 (2007).

[23] H. Tang, K. Prasad, R. Sanjinès, P. E. Schmid, and F. Lévy, *J. Appl. Phys.* **75**, 2042 (1994).

[24] T. Mazza, E. Barborini, P. Piseri, P. Milani, D. Cattaneo, A. Li Bassi, C. E. Bottani, and C. Ducati, *Phys. Rev. B* **75**, 045416 (2007).

[25] M. V. Abrashev, A. P. Litvinchuk, M. N. Iliev, R. L. Meng, V. N. Popov, V. G. Ivanov, R. A. Chakalov, and C. Thomsen, *Phys. Rev. B* **59**, 4146 (1999).

[26] M. Minohara, T. Tachikawa, Y. Nakanishi, Y. Hikita, L. F. Kourkoutis, J.-S. Lee, C.-C. Kao, M. Yoshita, H. Akiyama, C. Bell, and H. Y. Hwang, *Nano Lett.* **14**, 6743 (2014).

[27] S. Amoruso, C. Aruta, P. Aurino, R. Bruzzese, X. Wang, F. M. Granozio, and U. Scotti di Uccio, *Appl. Surf. Sci.* **258**, 9116 (2012).

[28] T. J. Regan, H. Ohldag, C. Stamm, F. Nolting, J. Lüning, J. Stöhr, and R. L. White, *Phys. Rev. B* **64**, 214422 (2001).

[29] M. Lazzeri, A. Vittadini, and A. Selloni, *Phys. Rev. B* **63**, 155409 (2001).

[30] J. K. Burdett, T. Hughbanks, G. J. Miller, J. W. Richardson, and J. V. Smith, *J. Am. Chem. Soc.* **109**, 3639 (1987).

[31] M. Sumita, C. Hu, and Y. Tateyama, *J. Phys. Chem. C* **114**, 18529 (2010).

Chapter 5.

Band alignment tuning at Pt/LaAlO₃/Nb:TiO₂ interface

5.1. Introduction

The principal goal of this chapter is to clarify the structural requirement to utilize oxide dipole for device applications with non-isostructural interfaces. As discussed in Chapter 2, there are three possible mechanisms in general that might screen dipole effect, which are surface reconstruction of polar surface and pinning effect originating from metal induced gap states (MIGS) or disorder induced gap states (DIGS). Although the pinning effect caused by MIGS in ionic materials is expected to be limited because of the small penetration length, the surface reconstruction and DIGS are likely to take place in oxides materials too. Therefore, the feasibility of perovskite dipole at general interfaces is not obvious and needs to be examined. In Chapter 4, we have established growth techniques to obtain high quality LaAlO₃/TiO₂/LaAlO₃ (100) heterostructure. Here, utilizing these samples, we aim to demonstrate the band alignment tuning at polycrystalline Pt/LaAlO₃/TiO₂ interface to clarify the structural requirement to activate perovskite oxide dipole.

5.2. Experimental

In this section, the experimental procedure to fabricate Pt/LaAlO₃/Nb doped 0.1 wt % TiO₂ (Nb:TiO₂)/LaAlO₃ (100) junction and SBH characterizations are described. Circular shape 5 nm thick Pt electrodes were deposited on top of LaAlO₃ (0-2 u.c.)/Nb:TiO₂/(40 u.c.)/LaAlO₃ (100) heterostructures. A schematic of the sample structure and expected band alignments are shown in Figure. 5.1. Nb:TiO₂ was employed instead of non-doped TiO₂ for stable control of carrier density by Nb dopant with small oxygen vacancies. The high quality LaAlO₃/Nb:TiO₂/LaAlO₃ (100) heterostructure can be fabricated using the same procedure optimized in Chapter 4. Nb:TiO₂ is grown by ablating polycrystalline Nb:TiO₂ target under the same condition as the undoped TiO₂.

The thickness of Pt was varied from 2 nm to 10 nm to clarify the optimal thickness for the various measurements employed. Pt metal slug with 99.99 % purity placed on the carbon crucible was evaporated by the electron beam gun under room temperature and at base pressure of 10⁻⁸ Torr. The diameter and the shape of the metal electrodes were defined by a shadow mask directly attached to the surface of the sample. In order to clean the surface of Pt metal source, pre-evaporation of the Pt slug was performed with the closed shutter for 10 min.

Prior to the Pt deposition, LaAlO₃/Nb:TiO₂/LaAlO₃ (100) heterostructures were annealed under 450 °C and 760 Torr oxygen atmosphere for 5 min. using the tube furnace to remove contaminants and to fill oxygen vacancies on the topmost surface. Figure. 5.2 shows the comparison of the current-voltage (*I-V*) characteristics of Pt/TiO₂ junction with

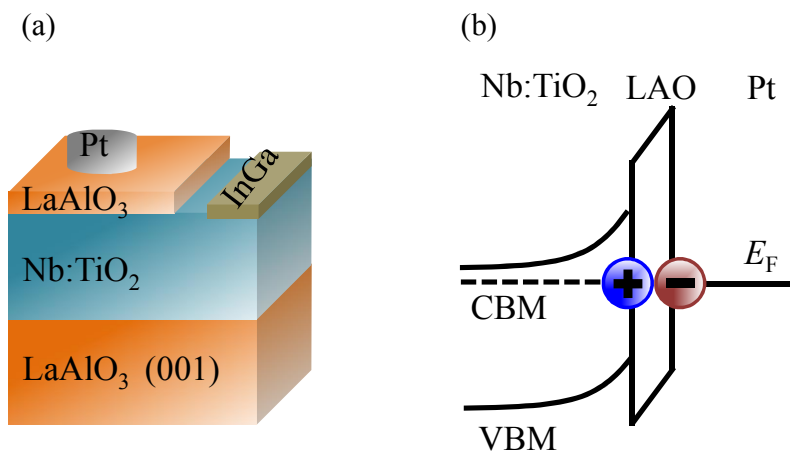


Figure. 5.1 (a) The schematic sample structure and (b) the expected band alignment of Pt/LaAlO₃/Nb:TiO₂/LaAlO₃ (100) heterostructure.

and without this heat treatment. Most of the junctions without heat treatment showed poor rectification properties with large leakage current in the reverse bias. This result suggests that the oxygen vacancies on TiO_2 (001) surfaces or carbon contaminations behave as an electrical leakage path in Pt/ TiO_2 junction. Since the saturation current at forward bias did not change after the heat treatment, only the surface oxygen vacancies are filled without affecting bulk structural properties. The junction without the heat treatment showed clear hysteresis by sweeping external bias. This result is consistent with the fact that oxygen vacancies are crucial for resistive switching behavior of Pt/ TiO_2 junctions [1]. Since suppression of reverse bias leakage is crucial for Schottky barrier height (SBH) measurements, this heat treatment was performed to all the junctions.

The band alignment tuning at Pt/ $\text{LaAlO}_3/\text{TiO}_2$ junction can be useful for practical devices because I - V characteristics of Pt/ TiO_2 junctions were widely studied for potential applications of resistive random access memories [1], photocatalysts [2] and gas sensors [3]. In spite of many studies about Pt/rutile TiO_2 junctions focusing on I - V , the intrinsic value of the SBH is still controversial owing to limited studies on capacitance voltage measurement (C - V) and no report of internal photoemission (IPE) both of which are considered as more reliable techniques to obtain the SBH in conventional semiconductor interfaces. In addition, there is no study for Pt/anatase TiO_2 junction which compare the SBHs obtained by C - V , I - V and IPE. The reported SBH values and measurement techniques are summarized in

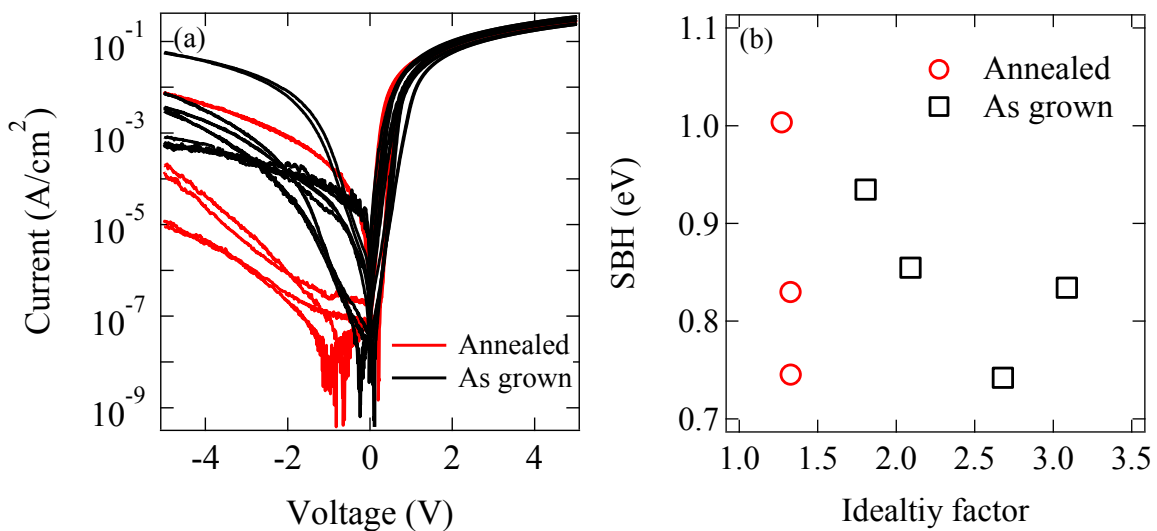


Figure. 5.2 (a) I - V curves of Pt Schottky electrodes deposited on as-grown anatase TiO_2 thin film and oxygen annealed films (760 Torr and 450°C for 5 minutes). I - V curve of four different electrodes for as grown and three annealed samples are displayed. (b) Obtained Schottky barrier height and ideality factors from I - V measurements.

Table. 5.1. In this study, three different SBH measurement techniques were applied to Pt/anatase TiO₂ heterojunction with small reverse bias leakage to establish a solid understanding of the SBH in this system.

Table. 5.1 The reported SBHs of Pt/Rutile TiO₂ junction measured by various measurement techniques [3-6].

Measurement techniques	Measured SBH (eV)	References
<i>I-V</i> , at room temperature	0.5 - 0.9	[3,4]
<i>I-V</i> Temperature dependent	0.5 - 1.37	[5,6]
<i>C-V</i>	1.3	[3]

5.3. Current voltage measurements

The *I-V* curves are summarized in Figure. 5.3 (a). All the junctions showed clear rectification proving the existence of Schottky barriers. The SBHs and ideality factors obtained from simple thermionic emission model discussed in Chapter 3 were summarized in Figure. 5.2 (b). The ideality factors were always larger than 1.5 indicating that simple thermionic emission is not valid. Therefore, although the SBH values are close to that reported for Pt rutile TiO₂ junctions, the barrier height obtained from this model is not reliable.

There are three possible reasons for the large ideality factors. First is that the contribution from thermionic field emissions and field emission in Pt/Nb:TiO₂ is relatively high because of the small depletion layer width in the junctions as discussed in Chapter 3. The calculated depletion layer is 30 nm considering the dielectric constant of 30 [7] and the dopant density of $1 \times 10^{19} \text{ cm}^{-3}$ assuming full ionization of Nb dopant which is consistent with the carrier density obtained from Hall measurements. In this carrier density and depletion layer thickness, thermionic field emission is the dominant charge transfer process as discussed in Chapter 3. However, the calculated ideality factor from eq. (3.12) is 1.07 which is much smaller than experimentally obtained ideality factor. Therefore, the large ideality factor increase cannot be attributed to thermionic field emission.

The second possibility is the existence of small SBH region which is pinched off. As discussed in Chapter 3, if there is a small circular patches with smaller barrier height,

the ideality factor n and the measured barrier height Φ_{Beff} are modified as follows [8]

$$n = 1 + \Gamma \quad (5.1)$$

$$\Phi_{\text{Beff}} = \Phi_{\text{B}} - 3eV_{\text{bi}}\Gamma \quad (5.2)$$

where Φ_{B} is the SBH and V_{bi} is the built-in potential of the junction without small patches. In the case of Nb:TiO₂, eV_{bi} almost equals SBH since the Fermi level is close to the conduction band bottom. If the large ideality factor at no LaAlO₃ case can be explained by the spatial inhomogeneity of the SBH, parameter $\Gamma = 0.6$ from the Eq. (5.1). However, the substituting this value into Eq. (5.2) yields a negative barrier height which is not consistent with the positive barrier height obtained in the experiment.

The third possibility is the dominance of trap assisted tunneling. Trap assisted tunneling is a direct tunneling process from the electron occupied trap state in a semiconductor to a metal [9]. The current originated from trap assisted tunneling (J_{trap}) is expressed as [10]

$$J_{\text{trap}} \propto \exp\left(\frac{-4\sqrt{2m_n(E_g - E_T)}}{3ehF}\right) \quad (5.3)$$

where m_n is the effective mass, E_g is the band gap of semiconductor E_T is the energy level of the trap from the valence band and F is the electric field at the interface.

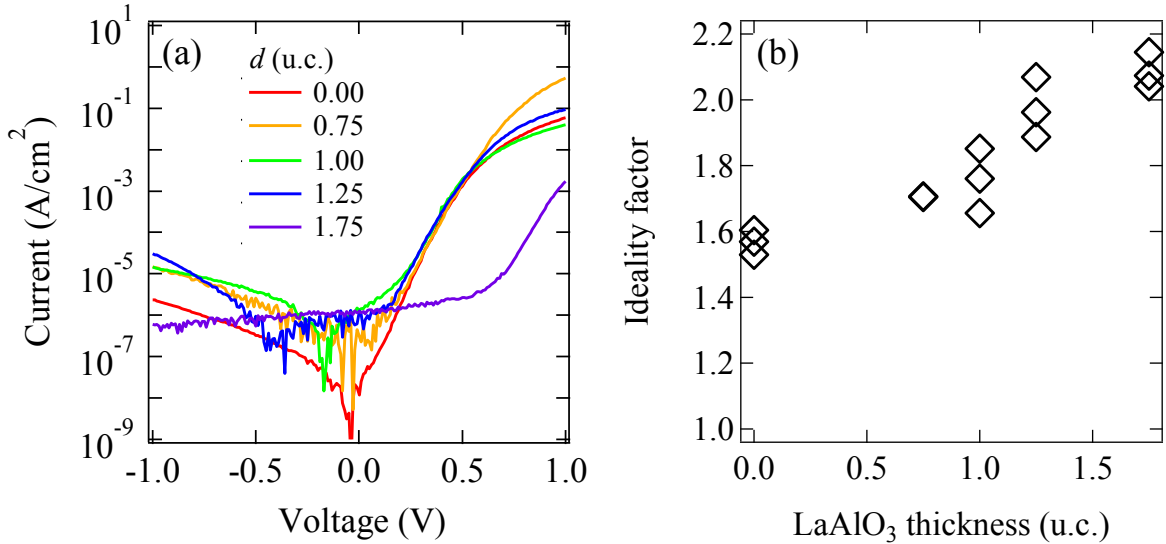


Figure. 5.3 (a) I - V curves of Pt (5 nm)/LaAlO₃ (d u.c.)/Nb:TiO₂ (40 u.c.)/ LaAlO₃ (100) and (b) LaAlO₃ thickness dependence of ideality factors derived from thermionic emission model.

Since the first derivative of the voltage dependence of J_{trap} is not proportional to $\exp(eV/k_{\text{B}}T)$, ideality factor should be larger than 1.0.

The increase of the ideality factor by the insertion of LaAlO_3 is explained by the existence of mid-gap states at the interface of $\text{LaAlO}_3/\text{TiO}_2$. Assuming the number of pinholes in the insulating layer are small and the charge transfer at the interface is not dominated by the pinholes, the ideality factor is described by the following formula [11]

$$n = 1 + \frac{q^2 d D_{\text{int}}}{\epsilon_{\text{ins}}} \quad (5.4)$$

where d is the thickness of the insulating layer, D_{int} is the energy density of interface states at the interface of the insulator and the metal, and ϵ_{ins} is the dielectric constant of the insulator. In the $\text{Pt}/\text{LaAlO}_3/\text{TiO}_2$ junction case, the ideality factors linearly increase with the thickness of LaAlO_3 capping layer in the gradient of 0.15 u.c.^{-1} . From this gradient, D_{int} is calculated as $6.0 \times 10^{13} \text{ cm}^{-2} \text{ eV}^{-1}$ when $\epsilon_{\text{ins}} = 30$ [12] which is in the range of the interface states in the conventional semiconductor [13]. It should be noted that this value is the supremum of D_{int} because it is assumed that the ideality factor increase is just explained by the Eq. (5.4).

5.4. Capacitance voltage measurement

As I - V measurement technique is not reliable technique to estimate the SBH because of too high ideality factor, the C - V measurement technique was applied to this system. In order to obtain the capacitance value of the junction, the equivalent circuit of the Schottky junction has to be clarified. The electrical impedance of the Schottky junction is described by a parallel a resistor and a capacitor in series with another resistor as shown in Figure. 5.4 (a) and C is the capacitance of the Schottky junction. First, frequency dependent impedance measurement was performed to obtain the R_{p} , C , R_{s} value in the model at $V = 0$ V. Frequency dependence of C_{p} was measured, which is the capacitance value when the equivalent circuit is assumed as a parallel circuit of a capacitor and resistor (Figure. 5.6 (b) and (c)). D is the dissipation defined as the real part of the impedance divided by the imaginary part. The relation between C_{p} , D , measurement frequency ω and impedance Z_{tot} is represented by the following formula,

$$Z_{\text{tot}} = iC_{\text{p}}\omega(1 + D) \quad (5.5)$$

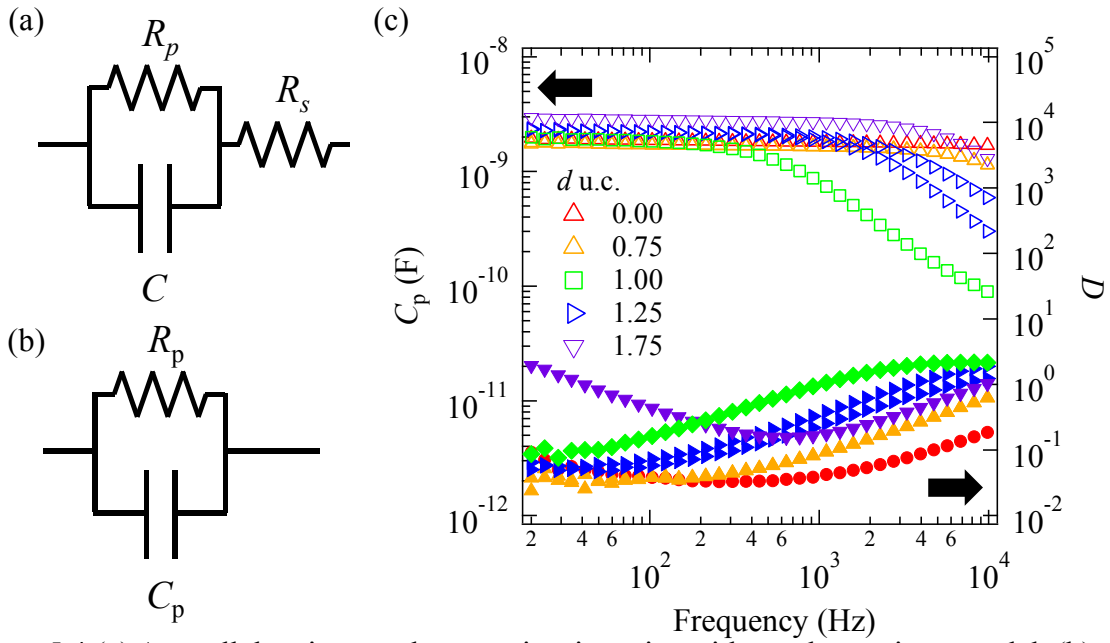


Figure. 5.4 (a) A parallel resistor and a capacitor in series with another resistor model. (b) a parallel resistor and capacitor model. (c) Capacitance frequency measurement of Pt (5 nm)/LaAlO₃ (d u.c.)/Nb:TiO₂ (40 u.c.)/LaAlO₃ (100). C_p and D shown by open and filled symbols, respectively.

In this model, Z_{tot} is expressed as

$$Z_{\text{tot}} = R_s + \frac{R_p(1 - iC\omega R_p)}{1 + (C\omega R_p)^2} \quad (5.6)$$

The obtained C , R_p , R_s values from these two equations are summarized in Figure. 5.6. As the thickness of LaAlO₃ layer increases, the R_p decreases indicating that increase of the electrical leakage at the junction though the insertion of the robust insulating layer at the interface. This trend implies the possible decrease in the SBH. The R_s value is almost independent of the LaAlO₃ layer thickness and roughly same as the resistance of the Nb:TiO₂ between the Pt electrode and the InGa Ohmic contact measured by a 4-probe method.

The measurement frequency of the capacitance voltage measurement was fixed to 1000 Hz because it should be performed at the frequency with minimum dissipation value to suppress the error bar of the capacitance which is expressed as

$$C_{\text{err}} = \frac{D}{\sqrt{1 + D^2}} \quad (5.7)$$

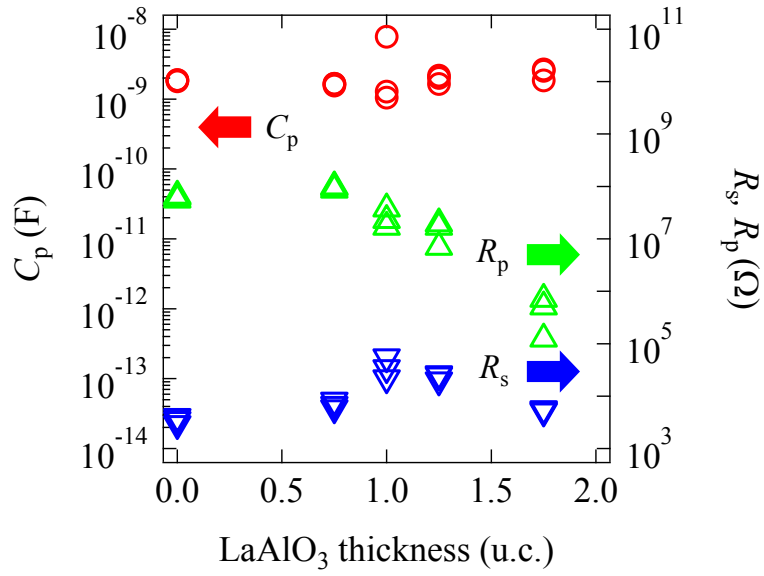


Figure. 5.6 Thickness dependence of C_p , R_s and R_p defined in Figure. 5.4 (a) and (b).

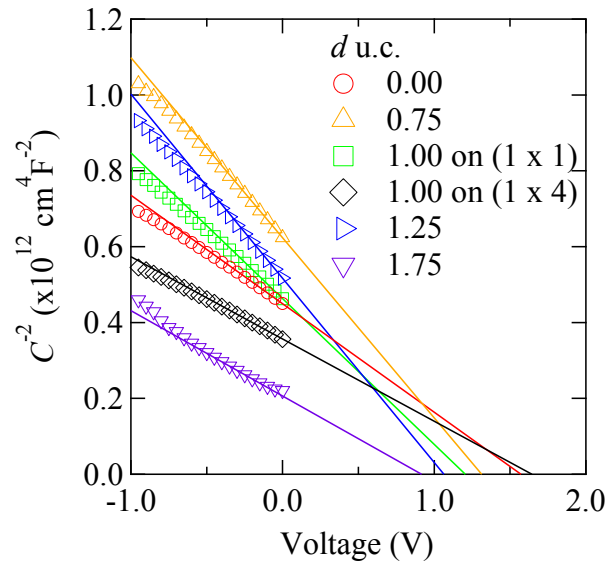


Figure. 5.5 C^{-2} vs. voltage of Pt/LaAlO₃(d u.c.)/Nb:TiO₂ (40 u.c.)/LaAlO₃ (100) junctions. Solid lines are linear extrapolations of the plot and V_{bi} is obtained as the voltage intercept of these linear fits.

The obtained C - V data of Pt/LaAlO₃ (d u.c.)/Nb:TiO₂ (40 u.c.)/LaAlO₃ (100) junctions are shown in Figure. 5.5. All the junctions showed linear relation in $1/C^2$ vs voltage indicating nearly uniform distribution of Nb dopant in the film. The calculated Nb dopant density from the gradient was $1.5 \times 10^{19} \text{ cm}^{-3}$ which is equal to the nominal dopant

density of the ablated target. V_{bi} value, which is almost same as SBH in heavily doped semiconductors, is obtained by the voltage intercept of the linear extrapolation of $1/C^2$ vs. voltage. The LaAlO_3 thickness dependence of V_{bi} is shown in Figure. 5.7 (b). The V_{bi} linearly decreases by 0.4 eV/u.c. with the thickness of LaAlO_3 suggesting the active role of LaAlO_3 as a dipole layer.

There are four possible origins for the decrease in V_{bi} . First, the dipole effect caused by the LaAlO_3 which is the goal in this study. Second, even if LaAlO_3 is a simple insulator without electrostatic dipole, there is a voltage drop as a capacitor connected in series with depletion layer of Nb:TiO_2 . In order to examine the second possibility, band alignment in a simple metal-insulator-semiconductor junction (MIS) was considered as shown in Figure. 5.7. From the Maxwell's equation, the voltage drop in the LaAlO_3 is calculated from the following formula,

$$V_{bi}(d) = \frac{C_{\text{LAO}} V_{bi}(d=0)}{C_{\text{LAO}} + 2C_{\text{TiO}_2}(V)} \quad (5.8)$$

where $V_{bi}(d)$ is built in potential inside the Nb:TiO_2 depending on the LaAlO_3 thickness, C_{LAO} and C_{TiO_2} are the capacitance of LaAlO_3 and the depletion layer, respectively. The derivation of this formula is discussed in Appendix A.1. The thickness dependent voltage drop in LaAlO_3 and Nb:TiO_2 are calculated assuming a dielectric constant of 30 for both LaAlO_3 (ϵ_{LAO}) and TiO_2 (ϵ_{TiO_2}). According to this simulation, almost no voltage drop (~ 0.04

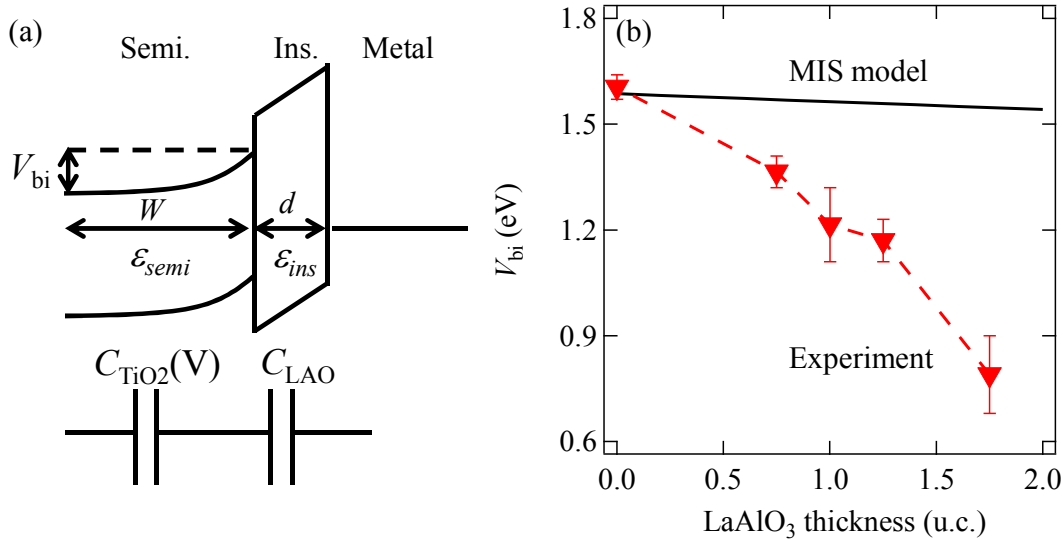


Figure. 5.7 (a) Band diagram of a MIS junction and equivalent series capacitor model. (b) LaAlO_3 thickness dependence of experimentally measured semiconductor built-in potential and that of simulated MIS model.

V) is expected. Therefore, the MIS model cannot explain the experimentally obtained data.

The third possibility is the screening effect of the charged mid-gap states at the interface of the insulator and semiconductor. They form the dipole with the screening charges in the metal side as shown in Figure. 5.8 (a). The magnitude of SBH change is described as following [14]

$$V_{\text{int}}(d) = \frac{edD_{\text{int}}(E_{\text{F}} - E_{\text{i}})}{\epsilon_{\text{int}}} \quad (5.9)$$

where E_{i} is the charge neutrality level in the semiconductor. $V_{\text{int}} = 0.06$ V when the thickness of LaAlO_3 is 1 u.c. using the value of D_{int} obtained by the gradient of ideality factor. Therefore, this is not the main reason of the SBH decrease either.

The fourth possibility is the charged defects at the insulator. Transistor turn-on voltage shift brought by the charged defects in the high- k dielectric is widely known phenomenon [14]. The basic principle is same as the interface states case discussed above as shown in Figure. 5.8 (b). Assuming there are only positively charged defects, the SBH modification is expressed as

$$V_{\text{int}}(d) = \frac{e \int_0^d SN_{\text{defect}} z dz}{\epsilon_{\text{int}}} \quad (5.10)$$

where N_{defect} is the density of positively charged defects, S is the number of charges in a defect, z is defined normal to the interface, 0 and d are the positions of the metal/insulator and the insulator/semiconductor interfaces. Assuming the entire barrier height change is explained by (5.10), $V_{\text{int}}(d) = 0.05$ eV at 1 u.c. for $SN_{\text{defect}} \approx 0.5$ u.c.⁻¹ which is not realistic. Therefore, this is not the major contribution either.

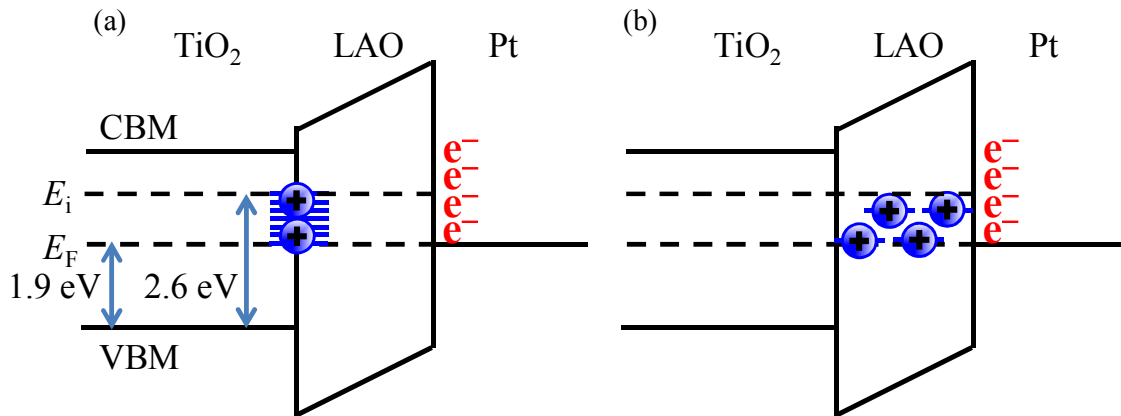


Figure. 5.8 Band diagrams focusing on the interfaces of metal insulator semiconductor junctions with (a) interface states and (a) positively charged defects in the insulator.

5.5. Internal photoemission technique

IPE technique was also employed to directly measure the SBH. First, the thickness of the Pt electrode on the top of TiO₂ was optimized to maximize the signal to noise ratio. This is because the monochromatic light is incident from the metal side, and considering the optical absorption of Pt in the measured wavelength region, it is expected that when the Pt thickness is too thick, the photocurrent is generated only at the surface of Pt and cannot reach the interface. On the other hands, as thickness decreases, photoexcitation in Pt

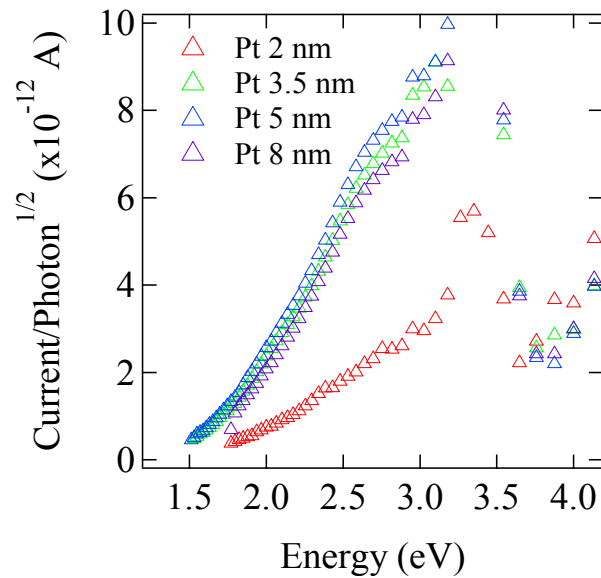


Figure. 5.9 Photoyield of Pt/Nb:TiO₂ (40 u.c.) Schottky junctions with various Pt thicknesses.

becomes smaller and total photocurrent decreases. Figure. 5.9 shows the photoyield, which is defined as the photocurrent generated by photon, of Pt/Nb:TiO₂/LaAlO₃ (100) junction with various Pt electrode thicknesses. When the Pt thickness is 5 nm, the photocurrent became maximum. For the following experiment, the Pt thickness was fixed to 5 nm for all the junctions by a crystal monitor during the deposition.

The IPE data of Pt/LaAlO₃/Nb:TiO₂/LaAlO₃ (100) with various LaAlO₃ thicknesses are summarized in Figure. 5.10 (a). The SBH is obtained by the photon energy intercept of the linear extrapolation of the square root of the photoyield defined as photocurrent generated per photon. However, the obtained square root of photoyield was not a simple linear function of the photon energy when LaAlO₃ was inserted. In order to explain the unexpected behavior of the photoyield, theoretical calculation of the photocurrent was performed. The Fowler's formula explained in Chapter 3 is modified by

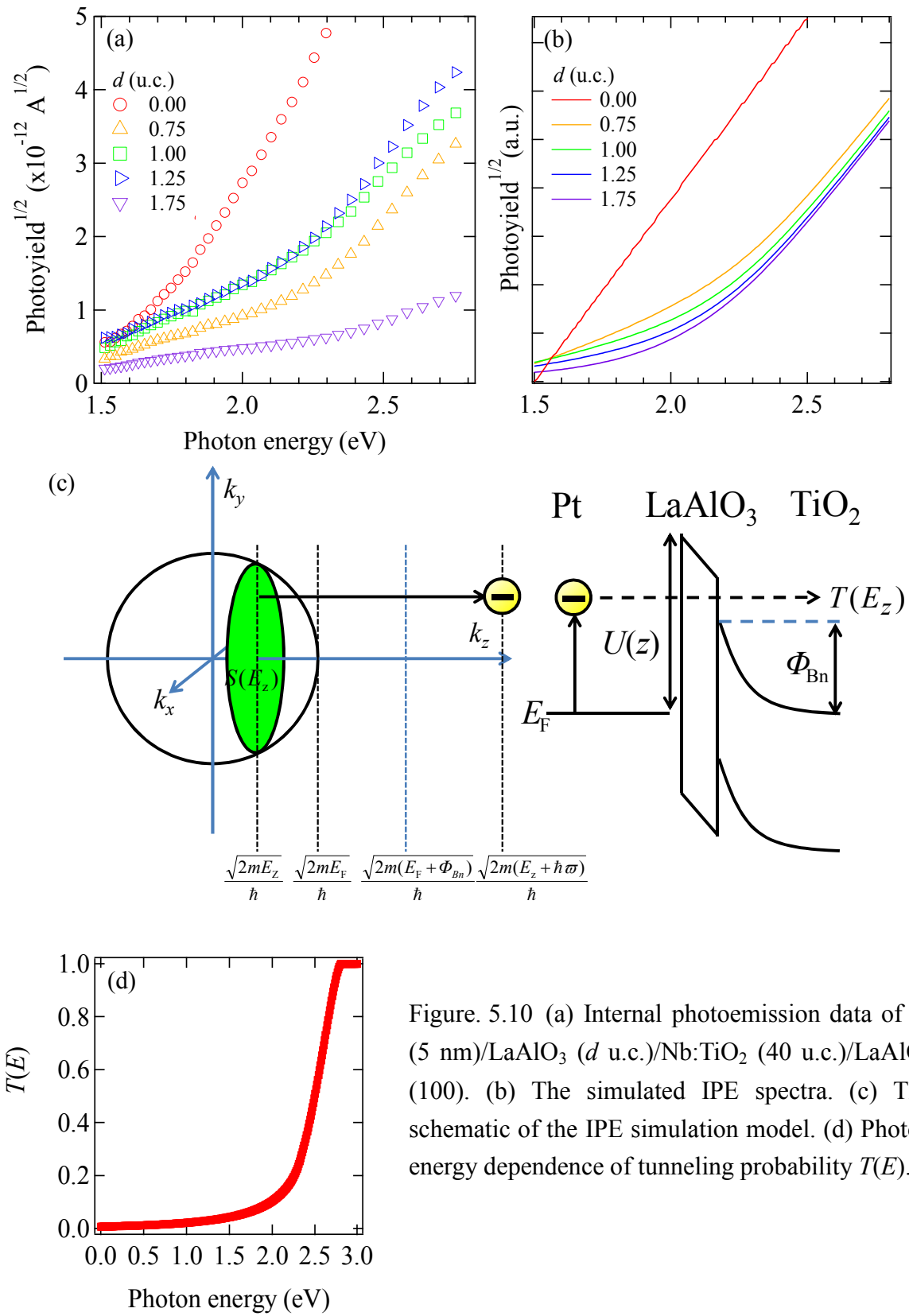


Figure 5.10 (a) Internal photoemission data of Pt (5 nm)/ LaAlO_3 (d u.c.)/Nb:TiO₂ (40 u.c.)/ LaAlO_3 (100). (b) The simulated IPE spectra. (c) The schematic of the IPE simulation model. (d) Photon energy dependence of tunneling probability $T(E)$.

considering the tunneling effect by LaAlO₃. The concept of the model is shown in Figure. 5.10 (c). In this model, the total photoyield (J) is described as follows:

$$J = \int T(E_z + \hbar\omega)S(E_z)dk \quad (5.11)$$

where $T(E_z + \hbar\omega)$ is the tunneling probability at a given kinetic energy of electrons normal to the surface (E_z) and $S(E_z)$ is the number of occupied electrons. The tunneling probability is calculated from the Fowler Nordheim tunneling with a triangle potential with WKB approximation using the following formula [15,16].

$$T(E_z) = \exp\left\{-2 \int_0^d \left[\frac{2m}{\hbar^2}[U(z) - E_z]\right]^{\frac{1}{2}} dz\right\} \quad (5.12)$$

$$U(z) = \Phi_{\text{Pt/LAO}} - Fz \quad (5.13)$$

where $U(z)$ is the conduction band minimum of LaAlO₃ along the out of plane, F is the electric field in the LaAlO₃ layer, $\Phi_{\text{Pt/LAO}}$ is the band offset between LaAlO₃ conduction band and Pt Fermi level at the Pt/LaAlO₃ interface. The barrier height between Pt and LaAlO₃ is estimated from the reported band alignment measured by XPS measurement [17]. The gradient of the potential in LaAlO₃ is assumed to be same as the gradient of V_{bi} shift obtained from C - V measurements because the SBH change induced by the LaAlO₃ is equal to the dipole potential of LaAlO₃. The reported LaAlO₃ and TiO₂ band gaps are 3.2 eV and 5.6 eV [7,18]. The electron energy dependence of the calculated tunneling probability for 1 u.c. LaAlO₃ is shown in Figure. 5.10 (d). The tunneling probability drastically changes in the energy range of 2.0 eV to 2.6 eV which corresponds to the maximum and the minimum of the energy difference between Pt Fermi level and LaAlO₃ conduction band. $S(E_z)$ is calculated by using the following formula assuming a parabolic band of the semiconductor as discussed in Chapter 3.

$$S(E_z) = \frac{2m\pi(E_F - E_z)}{\hbar^2} \quad (5.14)$$

where m is the effective mass in anatase TiO₂ which is equal to the free electron mass. Simulated photoyield and the experimentally obtained IPE data are compared in Figure. 5.10 (a) and (d) whose trend matches quite well. For LaAlO₃ inserted sample, both the experiment and the theory show clear kinks around 2.2 eV. This energy is almost equal to the average of the energy difference between the conduction band of LaAlO₃ and Pt Fermi level where the first derivative of tunneling probability becomes large. As photon energy becomes smaller than 2.2 eV, the square root of the photo yield is proportional to the photon

energy indicating that the Fowler's formula is applicable to obtain the SBH. Linear fittings in the magnified region of IPE data are shown in Figure. 5.11 (a) as solid lines. As LaAlO_3 becomes thicker, the monotonic shift in SBH is observed. In Figure. 5.11 (b), the V_{bi} obtained from $C-V$ and SBH by IPE showed good agreement except for 1.75 u.c. and both of them linearly decrease with the thickness of LaAlO_3 . The disagreement in 1.75 u.c is explained by the strong energy dependence in $T(E)$ for thicker tunneling barriers. From these result, it is concluded that the SBH decrease induced by LaAlO_3 was confirmed by multiple measurement techniques.

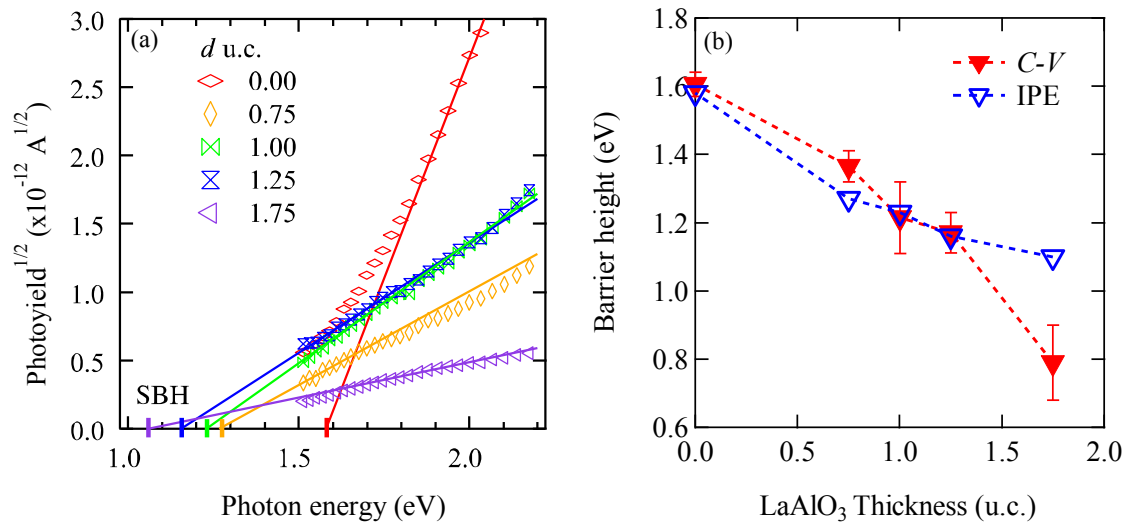


Figure. 5.11 (a) Magnified IPE data. Linear extrapolations of square root of photoyield to obtain SBH are shown expressed as solid lines. (b) The comparison of SBH measured by IPE and $C-V$. The dashed lines are guide for eye.

5.6. The origin of barrier height change

In order to examine the validity of the dipole explanation for the result, three questions should be answered.

1. Is the sign of the SBH change is correct?
2. Is the magnitude of the SBH change reasonable?
3. Is the SBH change proportional to the dipole moment of the dipole layer?

For the first question, the stacking order of $(\text{LaO})^+$ and $(\text{AlO}_2)^-$ layer has to be clarified because that determines the direction of the dipole moment. Previously, adhesion energy W_{ad} of LaO/TiO_2 and $\text{AlO}_2/\text{TiO}_2$ were calculated from first principles calculation [19]. The definition of the adhesion energy is,

$$W_{\text{ad}} = W_{\text{interface}} - W_{\text{TiO}_2} - W_{\text{LaAlO}_3} \quad (5.15)$$

where $W_{\text{interface}}$ is the total energy of the single terminated $\text{LaAlO}_3/\text{TiO}_2$ junction, W_{TiO_2} and W_{LaAlO_3} are the cohesive energy of isolated TiO_2 and LaAlO_3 , respectively. According to their calculation, the adhesion energy of LaO/TiO_2 is 4.02 J/cm^2 and $\text{AlO}_2/\text{TiO}_2$ is 3.02 cm^2 . Therefore, the energetically favorable LaO/TiO_2 interface is expected where the positively charged layer is adjacent to TiO_2 , SBH should decrease in our case which is consistent with the result.

The second question would be answered by treating LaAlO_3 as a parallel plate capacitor with Q equal to the charge density of single $(\text{LaO})^{1+}$ layer and $(\text{AlO})^{2-}$ layer. Based on this assumption, the dipole moment is calculated from the following formula

$$V_{\text{dipole}} = \frac{\epsilon_{\text{ins}} Q}{d} \quad (5.16)$$

where V_{dipole} is the built in potential of the dipole layer, Q is the charge density of the single $(\text{LaO})^+$ layer and d is the thickness of inserted LaAlO_3 . If LaAlO_3 is a purely ionic crystal

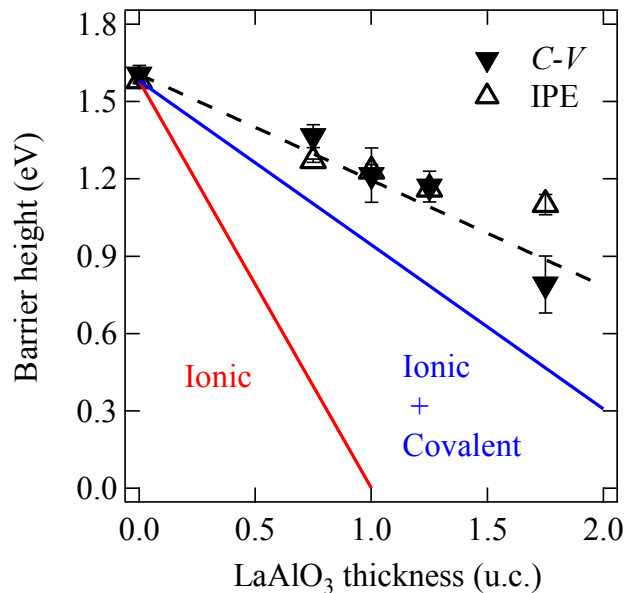


Figure. 5.12 The simulated SBH change when LaAlO_3 is treated as purely ionic crystal (red line) and when covalency is considered (blue line). Experimentally obtained SBH from IPE and $C-V$ is also displayed in black markers.

where LaO layer and AlO₂ layer have +1 and -1 charge as expected from their ionic valences, Q is calculated as $1.11 \times 10^{-5} \text{ C/cm}^2$ by using the bulk lattice constant of LaAlO₃, which is 0.379 nm. The thickness dependence of the SBH simulated by this theory and the experimental data are shown in Figure. 5.12, which shows a clear difference in their gradients. According to a first principles calculation, LaAlO₃ can be regarded as an alternate stacking of +0.4 and -0.4 charges considering the coexistence of covalency and ionicity in LaAlO₃ [20]. Considering the covalency of LaAlO₃, the thickness dependence of SBH is recalculated as shown in Figure. 5.12. The simulated data and the experimental result show good agreement with each other. The gradient of the simulated data is almost same as the SrRuO₃/SrTiO₃ data (0.75 eV/u.c.) reported previously too. The small difference in the gradient can be explained by the surface roughness of TiO₂ or pinning effect by DIGS.

In order to answer the third question, various dipole layers were inserted to Pt/TiO₂ interface. Three different interlayers, LaAlO₃, solid solution of LaAlO₃ and SrTiO₃, which is expressed as (LaAlO₃)_{0.5}(SrTiO₃)_{0.5}, and SrZrO₃ were employed. They can be regarded as alternate stacking of +1/-1 charges, +0.5/-0.5 charges and neutrally charged layers as shown in Figure. 5.13. Since the reported dielectric constant of LaAlO₃, (LaAlO₃)_{0.5}(SrTiO₃)_{0.5} and SrZrO₃ are 30, 30 and 28, respectively, the V_{dipole} expected from the Eq. (5.16) should be proportional to the charge density of the dipole layers.

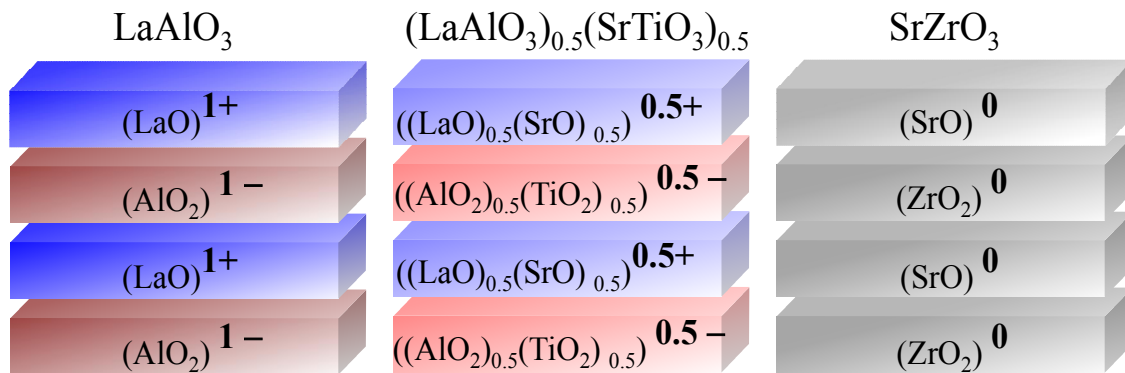


Figure. 5.13 Schematic structures of three different dipole layers, LaAlO₃, (LaAlO₃)_{0.5}(SrTiO₃)_{0.5} and SrZrO₃ employed in this study.

The SBH of Pt (5 nm)/(LaAlO₃)_{0.5}(SrTiO₃)_{0.5} or SrZrO₃ (*d* u.c.)/Nb:TiO₂ (40 nm) were characterized by *C-V* and IPE measurement as shown in Figure. 5.14. The monotonic shift in *V*_{bi} and SBH with the increase of (LaAlO₃)_{0.5}(SrTiO₃)_{0.5} thickness was observed and almost no thickness dependence in SrZrO₃ case. The variation of SBHs induced by the

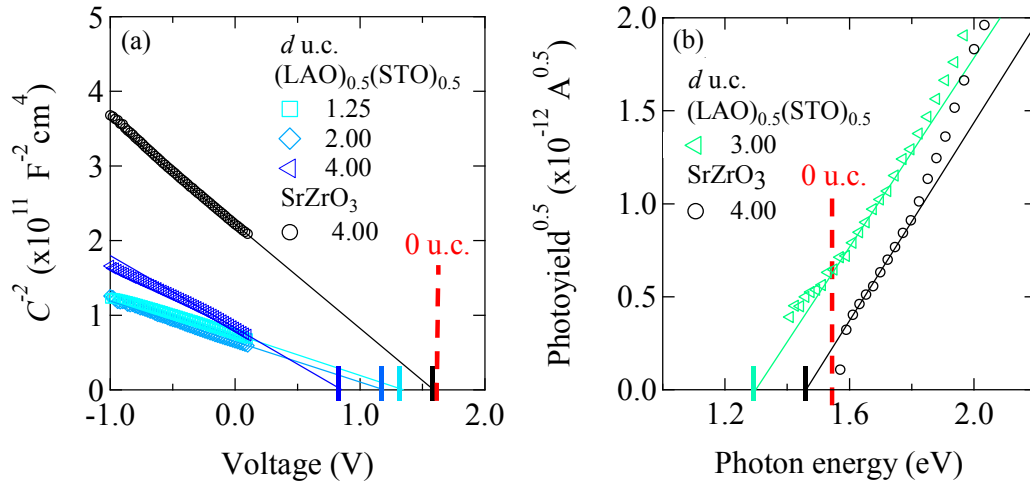


Figure. 5.14 (a) *C-V* and (b) IPE data for Pt (5 nm)/(LaAlO₃)_{0.5}(SrTiO₃)_{0.5} and SrZrO₃ (*d* u.c.)/Nb:TiO₂ heterojunction.

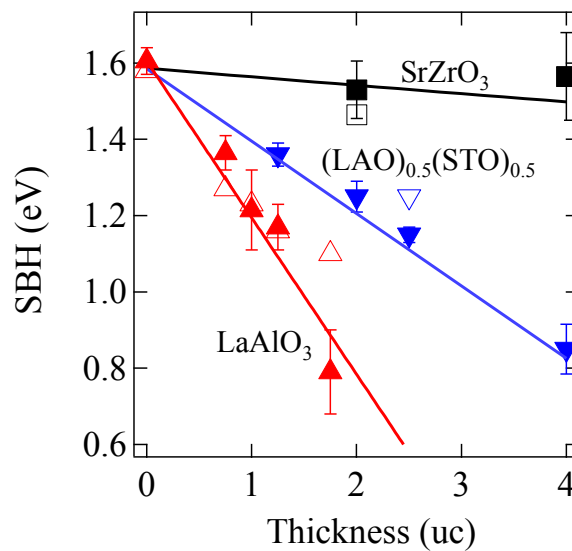


Figure. 5.15 The summary of SBH change induced by three different kinds of dipole layers, (LaAlO₃), (LaAlO₃)_{0.5}(SrTiO₃)_{0.5} and SrZrO₃ at Pt/Nb:TiO₂ interface characterized by IPE (open symbol) and *C-V* (filled symbol). Linear fitting are drawn by solid lines.

three different dipole layers are summarized in Figure. 5.15. SBH and V_{bi} measured by IPE and $C-V$ are proportional to the thickness of the dipole layers and showed good agreements in all the three dipole layers. The gradient of SBH change by $(LaAlO_3)_{0.5}(SrTiO_3)_{0.5}$ is roughly half of $LaAlO_3$ and there are no variation in $SrZrO_3$ case. These results indicate that the entire barrier height variation follows Eq. (5.16) which describes the SBH change induced by electrostatic dipole. Therefore it is concluded that all the data is explained by the electrostatic dipole effect originated from the ionic charges of the inserted layer.

5.7. Attempt to increase barrier height

In this Chapter, the SBH decrease at Pt/TiO_2 interface has been successfully demonstrated. In this section, an attempt to demonstrate an increase in the Pt/TiO_2 SBH is presented. As discussed, the sign of the dipole is determined by the sign of the charges adjacent to the semiconductor. Namely, a negatively charged AlO_2 layer has to be grown on top of bare anatase TiO_2 surface instead of an energetically favorable LaO layer to increase SBH. In order to achieve this, charge neutral SrO layer was grown on top of TiO_2 since subsequent $LaAlO_3$ layer is expected to start from the AlO_2 layer as shown in Figure. 5.16 (a). However, V_{bi} obtained by $C-V$ measurement of $Pt/LaAlO_3/SrO$ (1 u.c.)/ $Nb:TiO_2$ has not shown systematic change as displayed in Figure. 5.16 (b).

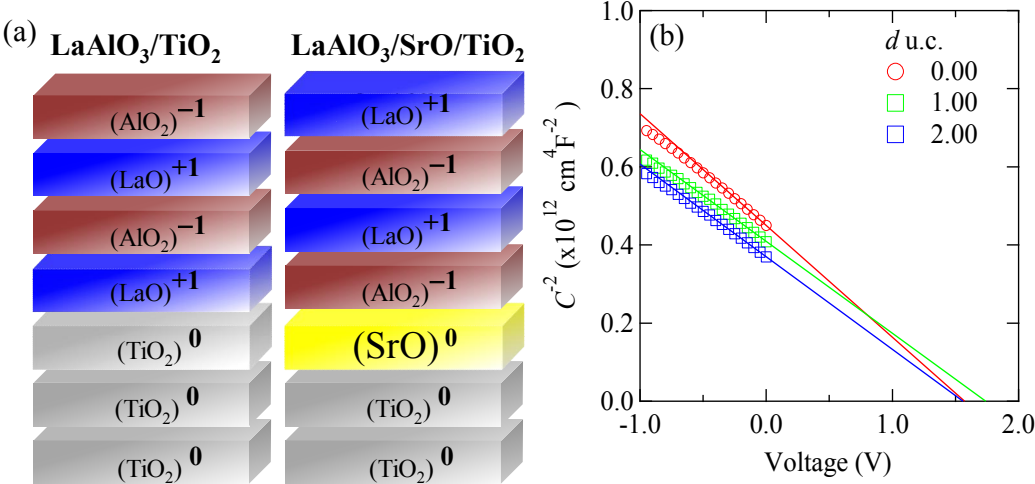


Figure. 5.16 (a) The atomic layer diagrams of $LaAlO_3/TiO_2$ and $LaAlO_3/SrO/TiO_2$ (b) $C-V$ measurement of Pt (5 nm)/ $LaAlO_3$ (d u.c.)/ SrO (1 u.c.)/ $Nb:TiO_2$ (40 nm)/ $LaAlO_3$ (100) heterostructure.

5.8. Comparison of three measurement techniques

I - V , IPE and C - V have been employed to estimate SBH of Pt/LaAlO₃/Nb:TiO₂ junction. Although IPE is considered as the most reliable technique for simple Schottky junction cases, the interpretation of IPE data can be difficult when multiple barriers exist as in the junction employed in this study. Here we summarize the advantages and the disadvantages of each measurement technique. Although I - V measurement is simple, it is most sensitive to local variations of SBH at the interface and difficult to estimate the SBH of the largest contact area. In addition, when the density of interface states between insulator and metal is as high as 10^{13} cm⁻², the ideality factor linearly increases with the thickness of the insulator layer. Also, the tunneling barrier should be so thin that the contact resistance of the tunneling barrier is negligible.

In the case of IPE, Fowler's formula is valid only when transmittance in Eq. (5.11) has no photon energy dependence. As we have already seen, small kinks showed up originating from the tunneling barrier which is not expected from the Fowler's formula. Since there is a strong energy dependence around the band offset between metal Fermi level and insulator conduction band, Fowler's fitting to obtain the metal/semiconductor barrier height should be performed below that photon energy.

For C - V , the capacitance originated from the insulator should be negligible. Since the dielectric constants of most of the oxide semiconductors and insulators are of the same order, depletion layer should be much larger than the thickness of insulating layer. This effect is negligible as long as the dopant density of the semiconductor is small and V_{bi} is high. Another assumption for V_{bi} derivation from linear fitting is the uniform distribution of the dopant density and no electric field dependence in the dielectric constant. Especially, SrTiO₃ is a representative example for its strong field dependence in the dielectric constant [21]. The strongest electric field of the junction is always at the interface. Therefore, the dopant density and V_{bi} should be low enough for electric field not to hit this limit. In our system, C - V is considered as most reliable measurement technique since there is no strong field dependence in dielectric constant and negligible capacitance of the insulating layer.

5.9. Conclusion

We aimed to demonstrate the band alignment tuning at the interface of polycrystalline Pt and anatase Nb:TiO₂ to clarify the structural requirement to utilize the

electrostatic dipole. In order to clarify the band alignment, Schottky barrier height is characterized by the three different techniques, current voltage, capacitance voltage, and internal photoemission. Current voltage technique is found to be not reliable to evaluate the Schottky barrier height because the simple thermionic emission model is no longer available to explain the result. Schottky barrier height estimated from the capacitance voltage measurement and the internal photoemission technique matches well. The linear decrease of Schottky barrier height was observed on LaAlO_3 grown on (1×1) unreconstructed anatase TiO_2 (001) surface and not on (1×4) reconstructed surface indicating that epitaxial relation between semiconductor and electrostatic dipole is crucial to enable the dipole. The sign and the gradient of the Schottky barrier height change agree with the theory. The obtained Schottky barrier height decrease was proportional to the thickness and the charge density of the dipole layer indicating that the entire result can be explained by the dipole effect. Therefore, we conclude that electrostatic dipole can be applicable to the interface consists of polycrystalline metal or non-perovskite oxide as long as the dipole is grown epitaxially.

5.10. Bibliography

- [1] D.-H. Kwon, K. M. Kim, J. H. Jang, J. M. Jeon, M. H. Lee, G. H. Kim, X.-S. Li, G.-S. Park, B. Lee, S. Han, M. Kim, and C. S. Hwang, *Nat Nano* **5**, 148 (2010).
- [2] G. R. Bamwenda, S. Tsubota, T. Nakamura, and M. Haruta, *Catal. Lett.* **44**, 83 (1997).
- [3] M. Cerchez, H. Langer, M. E. Achhab, T. Heinzl, D. Ostermann, H. Lüder, and J. Degenhardt, *Appl. Phys. Lett.* **103**, 033522 (2013).
- [4] C.-W. Wang, S.-F. Chen, and G.-T. Chen, *J. Appl. Phys.* **91**, 9198 (2002).
- [5] J.-J. Huang, C.-W. Kuo, W.-C. Chang, and T.-H. Hou, *Appl. Phys. Lett.* **96**, 262901 (2010).
- [6] K. M. Kim, B. J. Choi, D. S. Jeong, C. S. Hwang, and S. Han, *Appl. Phys. Lett.* **89**, 162912 (2006).

- [7] H. Tang, K. Prasad, R. Sanjinès, P. E. Schmid, and F. Lévy, *J. Appl. Phys.* **75**, 2042 (1994).
- [8] R. T. Tung, *Mat. Sci. Eng. R* **35**, 1 (2001).
- [9] J. Y. Wong, *IEEE Trans. Electron Devices* **27**, 48 (1980).
- [10] Q. K. Yang, F. Fuchs, J. Schmitz, and W. Pletschen, *Appl. Phys. Lett.* **81**, 4757 (2002).
- [11] H. C. Card and E. H. Roderick, *J. Phys. D: Appl. Phys.* **4**, 1589 (1971).
- [12] M. E. Aydin, F. Yakuphanoglu, J. H. Eom, D. H. Hwang, *Physica B & C* **387**, 239 (2007).
- [13] M. K. Hudait and S. B. Krupanidhi, *Mater. Sci. Eng., B* **87**, 141 (2001).
- [14] S.M. Sze and K. K. Ng, *Physics of Semiconductor Devices*, Wiley (1981).
- [15] G. Singh-Bhalla, C. Bell, J. Ravichandran, W. Siemons, Y. Hikita, S. Salahuddin, A. F. Hebard, H. Y. Hwang, and R. Ramesh, *Nat. Phys.* **7**, 80 (2011).
- [16] R. H. Fowler and L. Nordheim, *Proc. R. Soc. Lond. A* **119**, 173 (1928).
- [17] Z. Wang, W. Zeng, L. Gu, M. Saito, S. Tsukimoto, and Y. Ikuhara, *J. Appl. Phys.* **108**, 113701 (2010).
- [18] S.-G. Lim, S. Kriventsov, T. N. Jackson, J. H. Haeni, D. G. Schlom, A. M. Balbashov, R. Uecker, P. Reiche, J. L. Freeouf, and G. Lucovsky, *J. Appl. Phys.* **91**, 4500 (2002).
- [19] Z. Wang, W. Zeng, L. Gu, M. Saito, S. Tsukimoto, and Y. Ikuhara, *J. Appl. Phys.* **108**, 113701 (2010).
- [20] J. Goniakowski, F. Finocchi, and C. Noguera, *Rep. Prog. Phys.* **71**, 016501 (2008)
- [21] C. Ang and Z. Yu, *Phys. Rev. B* **69**, 174109 (2004).

Chapter 6.

Band offset increase by AgTaO_3 dipole layer at Pt/Nb:SrTiO_3 interface

6.1. Introduction

The central goal of this Chapter is the demonstration of band offset increase at a Schottky junction in which the semiconductor and the dipole layer are both perovskite oxides. In the previous study, the amplitude of band offset increase has remained smaller than 0.2 eV [1]. The major challenge in increasing the SBH lies is growing an oxide dipole layer whose negatively charged layer is adjacent to the oxide semiconductor as discussed in Section 5.9. Here we focus on the (100) orientation which has two independent terminations, BO_2 and AO . In case ABO_3 (A^{3+} , B^{3+}) is used as the dipole layer, the B-site (AlO_2^-) is always negatively charged. Since an alternate stacking of A-site and B-site is most energetically favorable for perovskite heterointerfaces, the perovskite semiconductor should be A-site terminated. However, in the case of SrTiO_3 , which is the most commonly utilized semiconductor in perovskite oxides, the A-site terminated surface is unstable compared with the B-site terminated. For example, The surface energy of SrO terminated is larger than that of TiO_2 [2]. Also, during the growth of LaAlO_3 on SrTiO_3 (100), higher density of oxygen vacancies are formed at the AlO_2/SrO interface compared to that of the LaO/TiO_2 interface [3]. The surface energy of SrO terminated is also larger than that of TiO_2 .

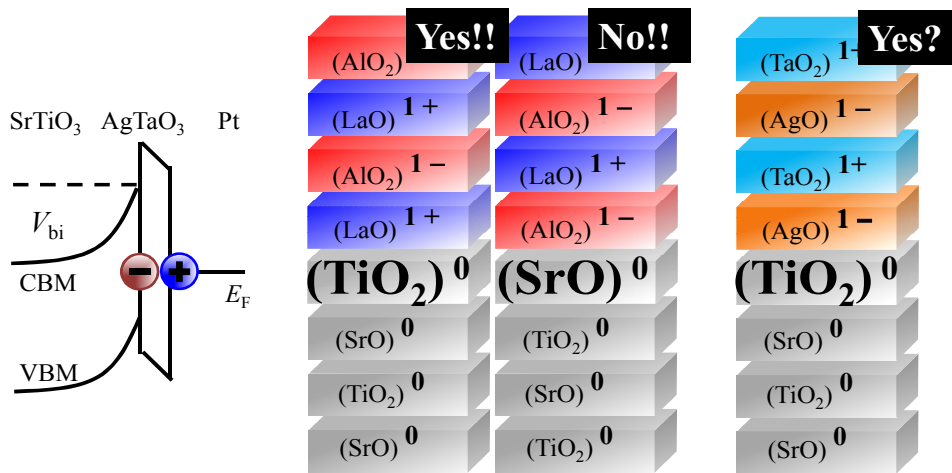


Figure. 6.1 The schematic band diagram of Pt/SrTiO₃ (100) required to achieve the increase of band offset where negatively charged layer of the dipole is adjacent to the SrTiO₃ (100). Schematic structure of LaO/TiO₂ interface of LaAlO₃/SrTiO₃ (100) where dipole works and AlO₂/SrO interface where dipole tuning is not effective. The structure of AgTaO₃/SrTiO₃ (100) interface that may show SBH increase by the dipole effect.

In this study, we focused on AgTaO₃ as an alternative oxide dipole layer in which the A-site layer (AgO⁻) has a negative charge and the B-site (TaO²⁺) has a positive charge as shown in Figure. 6.1. Thus, the barrier height increase would be achieved by AgTaO₃ grown on B-site terminated perovskite semiconductor such as TiO₂-terminated SrTiO₃ (100). We aimed to demonstrate the barrier height increase of Pt/SrTiO₃ (100) 0.02 eV by insertion of the AgTaO₃ layers.

In order to understand the band alignment of Pt/AgTaO₃/Nb:SrTiO₃ (100), it is crucial to understand the physical properties of constituting layer. The study of the physical properties of AgTaO₃ is still limited since there are only two reports for epitaxial thin films grown by PLD focusing on dielectric properties at high frequency (>100 KHz) [4,5] and one report for single crystal study focusing on the structural analysis [6]. Part of the reason for the limited number of studies is the difficulty in the growth of high purity AgTaO₃ samples. In this study, we will first characterize the basic physical properties such as band gap, dielectric constant and conductivity which are crucial in understanding the band alignment control of Pt/AgTaO₃/Nb:SrTiO₃ (100) heterostructure.

6.2. Experimental

AgTaO₃ films were epitaxially grown on 0.02 at.% Nb-doped SrTiO₃ (100) (Nb:SrTiO₃) substrates by using PLD with a KrF excimer laser onto a spot imaged size of 9.01 mm². Prior to the deposition, the substrates were annealed at 1000 °C under oxygen pressure of 1×10⁻⁶ Torr to obtain atomically flat and single TiO₂-terminated (100) surface. The RHEED pattern of the annealed substrate is shown in Figure. 6.2 (a). The AgTaO₃ films were grown under substrate temperature and oxygen partial pressure of 650 °C and 0.8 Torr, respectively. For laser conditions, a repetition rate and laser fluence were fixed to 10 Hz and 2.28 J/cm². The fast growth rate (0.04 nm/s) and the highly oxidizing atmosphere are crucial because Ag⁺ is easily reduced. It was also reported that high oxygen pressure was crucial to obtain stoichiometric AgTaO₃ nano particles [7]. The RHEED pattern, the AFM image and the XRD patterns of the fabricated films are summarized in Figure. 6.2 (b) - (d). The full width half maximum of AgTaO₃ 200 peak in pseudocubic representation was 0.21° which is smaller than the previous report of 0.28° [5]. Optical transmittance and reflectance measurement was performed to characterize the band gap by using UV-Vis spectrometer (wavelength range 200 nm ~ 1000 nm). The dielectric constant of AgTaO₃ was characterized by the impedance measurement by making a AgTaO₃ capacitor using Pt and Nb:SrTiO₃ as the top and the bottom electrodes. The structural properties of AgTaO₃ were characterized by atomic force microscopy (AFM) and X-ray diffraction techniques (XRD). In order to observe the dipole effect, Schottky barrier height (SBH) was characterized by

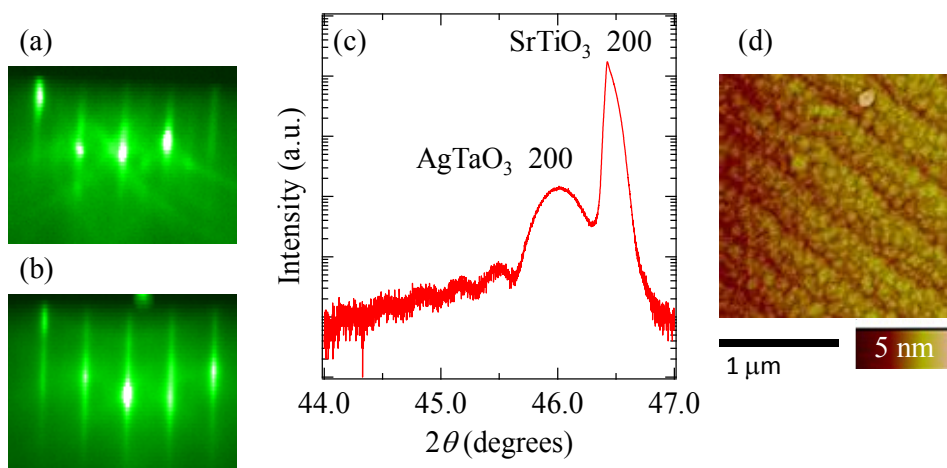


Figure. 6.2 (a) RHEED patterns of pre-annealed Nb:SrTiO₃ (100) substrate and (b) AgTaO₃ film grown under the optimal condition. (c) The XRD $2\theta - \omega$ scan and (d) AFM image of 27 nm thick AgTaO₃ grown on Nb:SrTiO₃ (100) substrate.

capacitance voltage (C - V), current voltage (I - V) and internal photoemission (IPE) as done in the previous Chapter.

6.3. Characterizations of basic physical properties of AgTaO_3

In this Section, we will determine the basic physical properties of AgTaO_3 to understand the band alignment of Pt and AgTaO_3 . AgTaO_3 is a rhombohedral phase ($R3c$) at room temperature whose lattice constant is 0.396 nm as a pseudo perovskite [6]. It is a robust insulator whose band gap is around 3.4 eV [8].

First, the band gap is determined by optical transmittance and reflectance measurement. Since the reported band gap is around 3.4 eV [8], the 24 nm AgTaO_3 was grown on a LaAlO_3 (100) substrate which is a wide gap (5.6 eV) insulator [9]. The obtained absorption coefficients of $\text{AgTaO}_3/\text{LaAlO}_3$ (100) and LaAlO_3 (100) substrate are plotted in Figure. 6.3 (a). Since the film thickness is thinner than quarter of the shortest measurement wavelength (200 nm), there is no thin film interference from the reflected waves at the film surface and the film/substrate interface. A clear absorption edge originating from the onset of photoabsorption in AgTaO_3 was observed at 3.4 eV which does not appear in the LaAlO_3

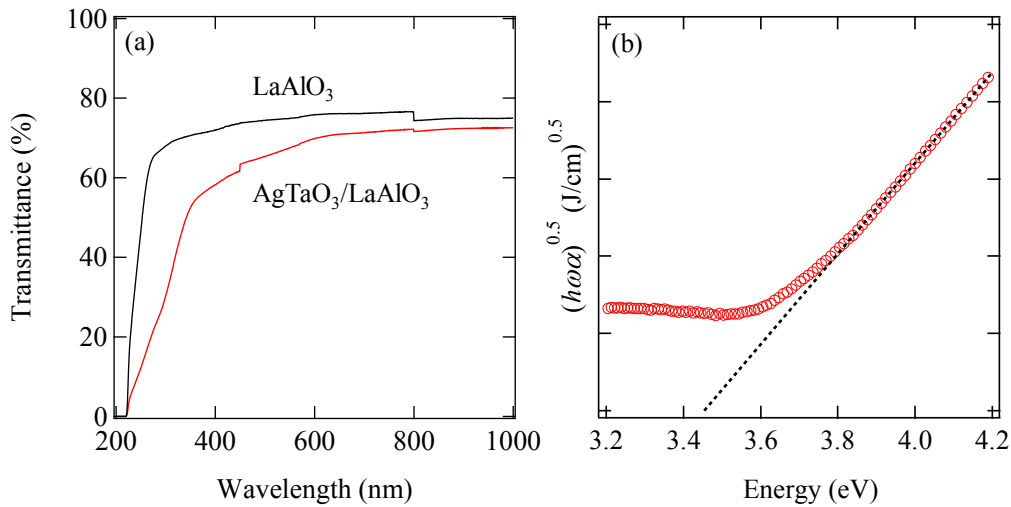


Figure. 6.3 (a) Optical transmittance data for LaAlO_3 (001) substrate and AgTaO_3 (24 nm)/ LaAlO_3 (100) heterostructure. The abrupt change in transmittance at 800 nm and 450 nm originate from the exchange of the grating and the light source, respectively. (b) $\sqrt{h\omega\alpha}$ vs. excitation energy where α is the absorption coefficient of AgTaO_3 obtained from (a) and ω is the frequency of excitation light. The linear extrapolation of the data is shown in dashed line and band gap is linear energy intercept of it.

(100) substrate. In order to clarify the band structure and the accurate band gap, vs. the photon energy vs. the product of the square root of the absorption coefficient and the photon energy is plotted on Figure. 6.3 (b). Linear behavior around the absorption edge indicates that AgTaO₃ has a 3.45 eV indirect band gap.

Next we characterized the dielectric constant of AgTaO₃ thin films. The dielectric constant of AgTaO₃ has to be clarified for two reasons. First, the dielectric constant determines the built-in potential of the dipole following Eq. (5.16). Second, the series capacitance originating from the AgTaO₃ dipole layer could affect the capacitance values in

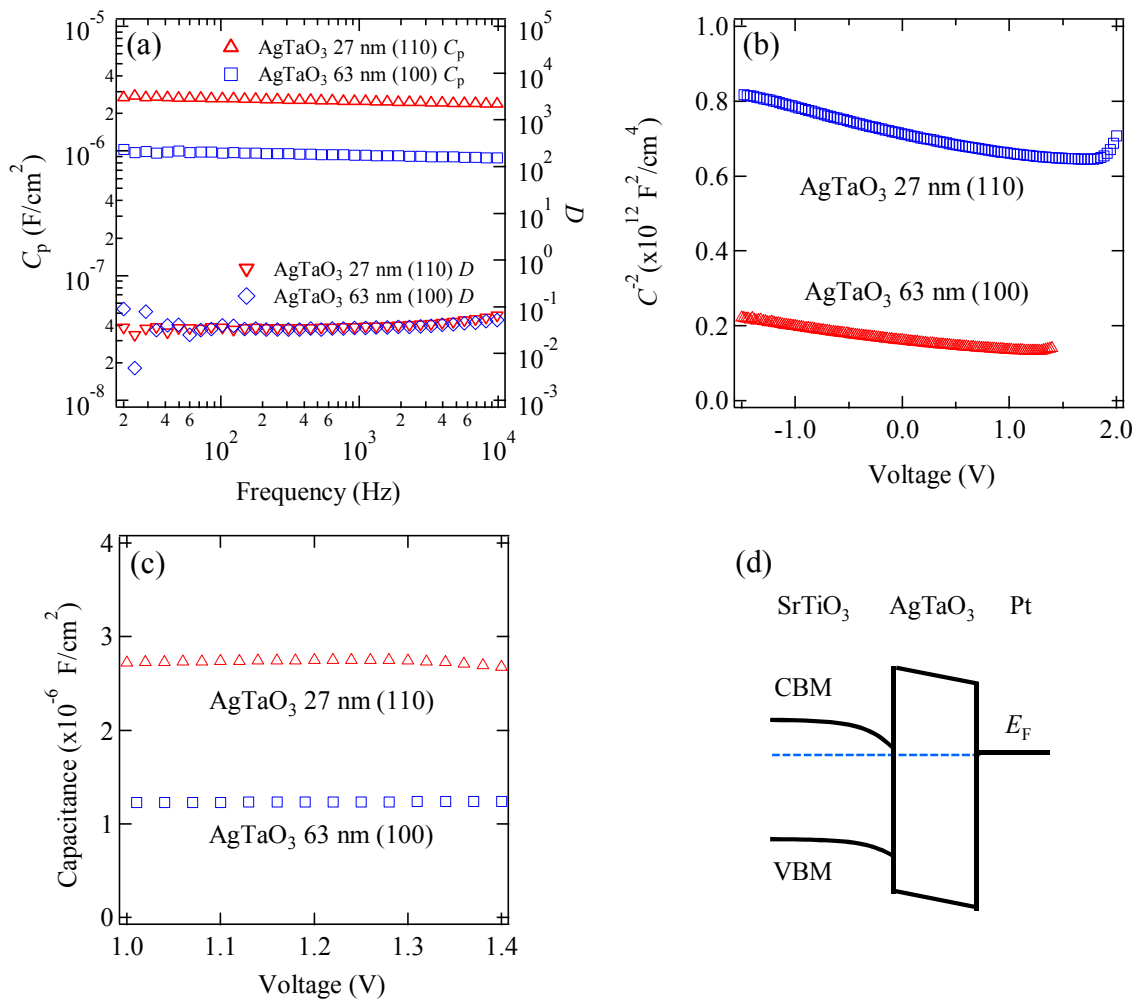


Figure. 6.4 (a) C_p (left), D (right) vs. frequency data and $C-V$ data at 1000 Hz of AgTaO₃ (63 nm)/1 at.% Nb-doped SrTiO₃ (100) and AgTaO₃ (27 nm)/1 at.% Nb-doped SrTiO₃ (110) (c) Capacitance data of the same sample under the bias where 1 at.% Nb-doped SrTiO₃ is accumulated and entire capacitance is originate from AgTaO₃. (d) Band alignment of the Pt/AgTaO₃/1 at.% Nb-doped SrTiO₃ under forward bias.

the junction C - V measurements. The dielectric constant was characterized using a AgTaO_3 thin film capacitor with a Pt top electrode and 1 at.% Nb-doped SrTiO_3 (110) and (100) substrates utilized as bottom electrodes to measure the crystal orientation dependence of the dielectric constant. The frequency dependence of C_p and D of fabricated capacitors are shown in Figure. 6.4 (a). The almost constant C_p value over the measurement frequency range (10 Hz to 10000 Hz) indicates that there is no apparent admittance from defects in the AgTaO_3 thin film at room temperature.

Capacitance voltage measurement was performed as shown in Figure. 6.4 (b). In the reverse bias, the $1/C^2$ vs. voltage plot showed a linear decrease indicating that although the substrate is heavily doped, the depletion layer exists and contributes as a capacitor connected in series with the AgTaO_3 thin film capacitance. When the applied forward bias was higher than 1.0 V, which is close to the SBH of Pt/Nb: SrTiO_3 junction (1.5 eV), the capacitance value became almost constant as shown in Figure. 6.4 (c). This result indicates that the Nb-doped SrTiO_3 is now in the accumulation mode and there is no depletion capacitance. Therefore, the capacitance value in the forward bias larger than 1.0 V can be regarded as the AgTaO_3 capacitance. The dielectric constant is obtained from the simple formula $C = \epsilon/d$ where ϵ is the dielectric constant and d is the thickness of AgTaO_3 film characterized by the X-ray reflectivity measurement. The obtained dielectric constants in the (100) and the (110) directions are 88 and 89, respectively which are slightly lower than the previously reported value of 110 for PLD grown AgTaO_3 on SrRuO_3 [4].

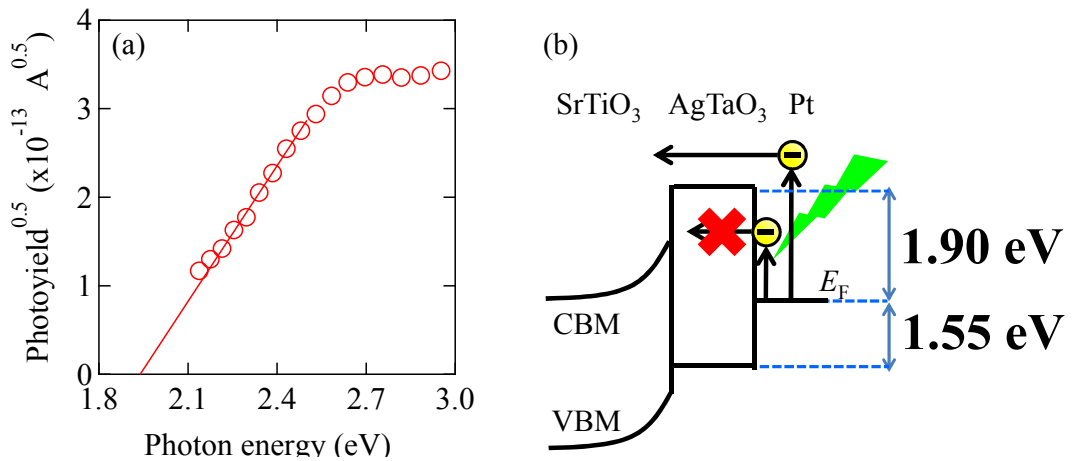


Figure. 6.5 (a) IPE data of Pt/ AgTaO_3 (40 nm)/Nb: SrTiO_3 (100) heterostructure. Linear fitting of the photoyield is shown as a solid line. The intercept to the photon energy gives the Pt/ AgTaO_3 barrier height. (b) Band diagram of Pt/ AgTaO_3 /Nb: SrTiO_3 (100) from the sequence of measurements.

Third, we aimed to determine the band offset between AgTaO₃ conduction band and Pt Fermi level which affects the tunneling probability of I - V and IPE measurements as discussed in Chapter 5. The band offset is characterized by IPE measurement of a Pt/AgTaO₃ (40 nm)/0.02 at.% Nb-doped SrTiO₃ (100) heterostructure as shown in Figure. 6.5 (a). Since the AgTaO₃ is thick enough to suppress any tunneling current from the Pt through the AgTaO₃, the linear extrapolation of the square root of the photoyield is expected to give the band offset as shown in Figure. 6.5 (b). The obtained IPE data is shown in Figure. 6.4 (a) and the band offset was calculated as 1.9 eV. From these results the band alignment between Pt and AgTaO₃ is identified as shown in Figure. 6.5 (b). Because of the large dielectric constant of AgTaO₃, the gradient of voltage drop as a simple insulator in AgTaO₃ is small.

6.4. Schottky barrier height characterization

In this Section, we will demonstrate the barrier height tuning in Pt/AgTaO₃ (d u.c.)/Nb:SrTiO₃ (100) Schottky junctions. First, I - V measurement was performed to characterize the SBH. The I - V data are shown in Figure. 6.6 (a) and all the junctions showed clear rectifying properties indicating formations of Schottky barriers. The saturation current under forward bias decreased as AgTaO₃ thickness became larger than 8 u.c. indicating that the junction resistance is dominated by the tunneling barrier in this voltage

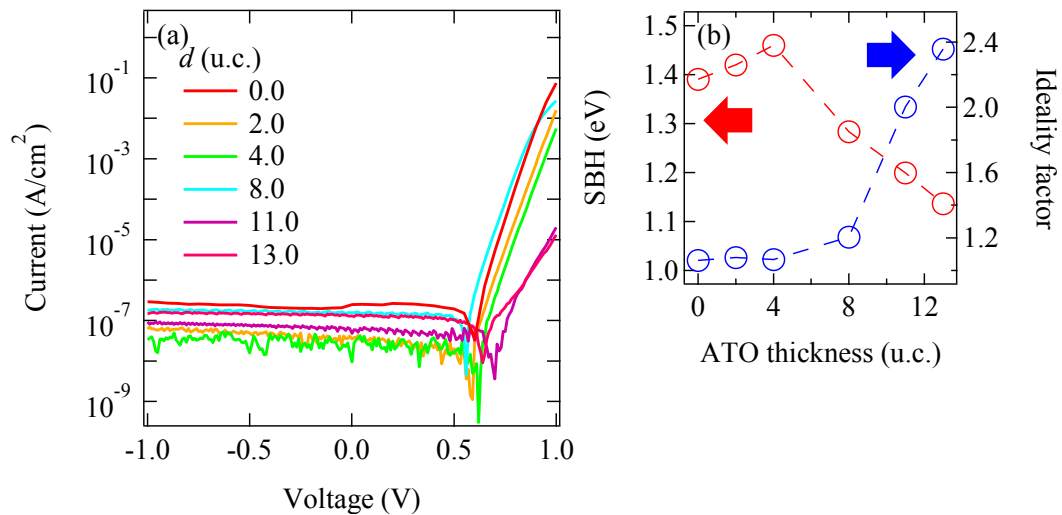


Figure. 6.6 (a) I - V curves and (b) SBH (left) and ideality factor (right) obtained from the thermionic emission model for Pt (5 nm)/AgTaO₃ (d u.c.)/Nb:SrTiO₃ (100) junctions.

range. The thickness dependence of the ideality factor and the SBH is plotted in Figure. 6.6 (b). The SBH monotonically increased until 4 u.c. of AgTaO₃ with small ideality factor suggesting the active role of AgTaO₃ as a dipole layer. The abrupt increase of ideality factor above 8 u.c. is explained by the increase of tunneling resistance which is consistent with the decrease of saturation current [10].

Since the tunneling effect is not negligible as AgTaO₃ becomes thicker, C - V measurement was performed. First, the equivalent circuit is determined by the frequency dependent impedance measurement as displayed in Figure. 6.6. All the junctions showed small dissipation value up to 10000 Hz and constant C_p value throughout the measured frequency range. This result indicates that these junctions can be regarded as a series connection of a simple capacitor with small electrical leakage and a resistor. This small electrical leakage is consistent with the small reverse bias current in the I - V data. In the C - V data in Figure. 6.8 (a), all the junctions showed linear $1/C^2 - V$ behavior indicating uniform dopant distribution in the Nb:SrTiO₃ substrate as expected. The impedance originating from AgTaO₃ can be negligible because C^2 of 10 u.c. AgTaO₃ is as small as $2.58 \times 10^9 \text{ cm}^4\text{F}^{-2}$. The V_{bi} value, which was obtained by the voltage intercept of linear extrapolation of $1/C^2 - V$, did not show monotonic change with respect to the thickness of AgTaO₃ layer as shown in Figure. 6.8 (b). The monotonic increase in V_{bi} was observed up to 8 u.c. and suddenly dropped at 11 u.c. This trend can arise from the electronic reconstruction driven by the

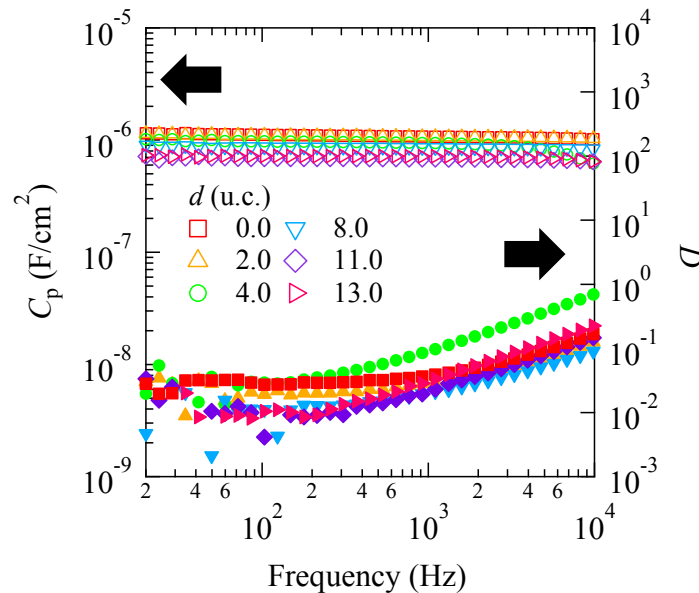


Figure. 6.7 Capacitance-frequency data of Pt (5 nm)/AgTaO₃ (d u.c.)/Nb:SrTiO₃ junctions. The definition of C_p and D are described in the previous Chapter.

accumulated total electrostatic energy with the AgTaO₃ thickness as discussed in Chapter 2 similar to the report in LaAlO₃/SrTiO₃ (100) interface [11]. If this is the case, the critical thickness of AgTaO₃ where the reconstruction happens is three times bigger than that of LaAlO₃. This is justified by calculating the total electrostatic energy E in the dipole layer using the following equation

$$E = \frac{1}{2} \varepsilon_{dipole} F^2 d \quad (6.1)$$

where d is the thickness of the dipole layer and F is the electric field and which can be calculated from the gradient of V_{bi} vs. thickness. F in AgTaO₃ is approximately three times smaller and ε_{dipole} is three times bigger than LaAlO₃. Therefore, assuming the electrical reconstruction occurs at the same electrostatic energy independent of the material, the critical thickness of AgTaO₃ is three times bigger than LaAlO₃ which is consistent with the experiment.

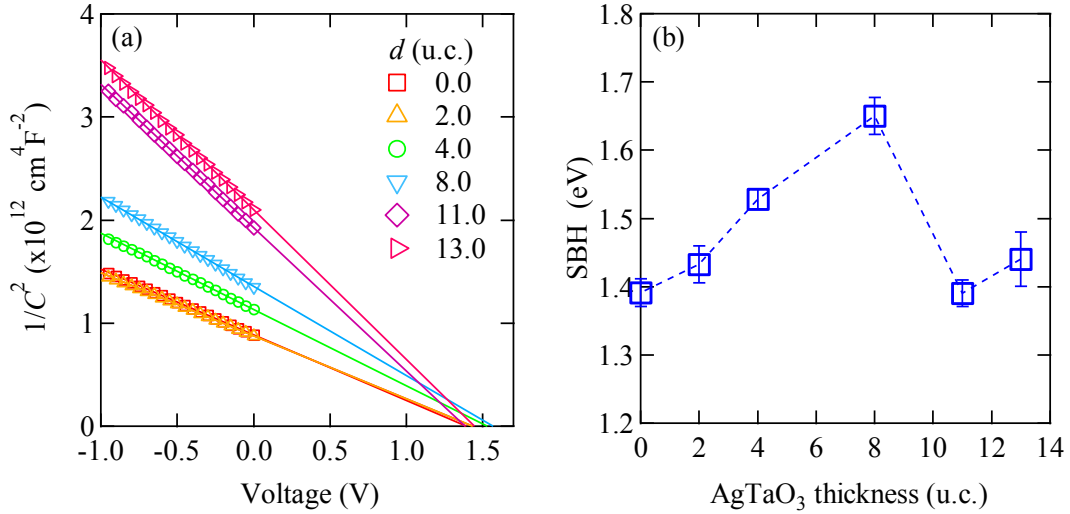


Figure. 6.8 (a) C - V data of Pt (5 nm)/AgTaO₃ (d u.c.)/Nb:SrTiO₃ (100) junctions. Linear fittings of C^{-2} vs. V are shown as solid lines. (b) AgTaO₃ thickness dependence of V_{bi} obtained from (a).

IPE was also performed to obtain the SBHs for different AgTaO₃ thickness. The square root of the photoyield vs. photon energy of Pt (5 nm)/AgTaO₃ (d u.c.)/Nb:SrTiO₃ is plotted in Figure. 6.9 (a). The SBHs were estimated from the photonenergy intercept of the linear extrapolation of the square root of the photoyield. The obtained thickness dependence of the SBH is plotted in Figure. 6.9 (b). Unlike the V_{bi} , the photonenergy intercept monotonically increases even beyond 8 u.c. and approaches to 1.9 eV. This is because the photoelectrons excited in the Pt metal cannot tunnel to the SrTiO₃ conduction band at

thicker AgTaO_3 , and therefore the photothreshold converges to the Pt/ AgTaO_3 barrier height. Therefore, the Pt/ SrTiO_3 SBH cannot be obtained from IPE at $d > 8$ u.c.

The obtained SBH change from IPE and $C-V$ are compared in Figure. 6.9 (b). The basic trend until 8 u.c. matches quite well. The absolute values of SBH by IPE and V_{bi} are always different by 0.15 eV suggesting that Fermi level of Nb: SrTiO_3 is lower than that of conduction band minimum which is also reported in $I-V$ and $C-V$ measurement of the $\text{SrRuO}_3/\text{LaAlO}_3/\text{Nb}:\text{SrTiO}_3$ junctions [1]. Therefore, it is concluded that SBH increase was successfully demonstrated by AgTaO_3 dipole layer.

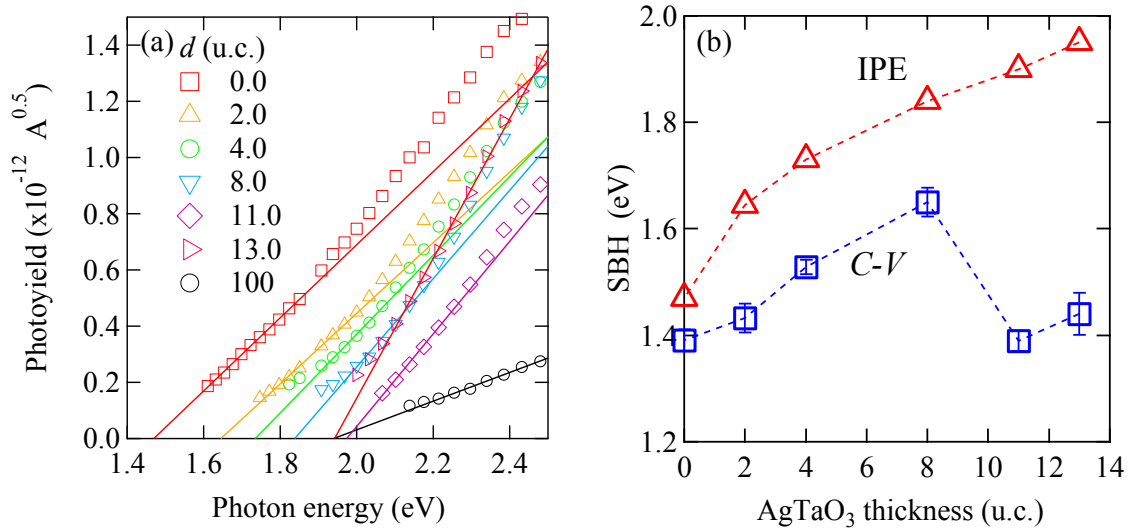


Figure. 6.9 (a) IPE data of Pt (5 nm)/ AgTaO_3 (d u.c.)/Nb: SrTiO_3 . (b) Summary of obtained V_{bi} and SBH from $C-V$ and IPE.

6.5. Solar cell operation of Pt/ AgTaO_3 junction

As an example of possible applications of the dipole tuning technique to practical devices, photovoltaic properties of Pt (5 nm)/ AgTaO_3 (d u.c.)/Nb: SrTiO_3 (100) junctions were studied. In this Schottky-type solar cell, photoabsorption at the Pt/Nb: SrTiO_3 interface occurs and the generated photocarriers are efficiently separated by the depletion width in Nb: SrTiO_3 . Since the SBH is raised by AgTaO_3 , an open circuit voltage increase is expected. An equivalent circuit and a typical $I-V$ curve of general solar cells are displayed in Figure. 6.10 where a constant current source and a diode correspond to the generation of photocurrent and the Schottky junction, respectively. Under an open-circuit condition, all

the photogenerated current flows through the diode. Thus, open circuit voltage V_{OC} is defined as following equation.

$$I_{sc} = A^* T^2 \exp\left(\frac{eV_{OC} - e\Phi_B}{n_{ideal} k_B T}\right) \quad (6.2)$$

where A^* is the Richardson constant, Φ_B is the SBH, n_{ideal} is the ideality factor of the diode and I_{sc} is the generated photocurrent. When A^* and n_{ideal} is not affected by the dipole insertion, the increase of the Φ_B is equal to that of V_{oc} .

The photovoltaic properties of the devices are measured under an 1 sun condition generated by a solar simulator (AM1.5G, 100 mW/cm²) from the top electrode side which was calibrated by a 1-sun checker. The current voltage properties under an 1 sun radiation and a dark condition with various AgTaO₃ thicknesses are shown in Figure. 6.11 (a). All of them showed typical solar cell behaviors.. The thickness dependences of the short circuit current and the open circuit voltage are displayed in Figure. 6.11 (b). The open circuit voltage increased from 0.7 to 0.82 V by the AgTaO₃ insertion which saturated at 2 u.c. because of the decrease of the short circuit current originated from the increasing tunneling barrier. The solar cell efficiency at the maximum power point where the current voltage product becomes maximum was 0.1 % for the 0 u.c. to 4 u.c. sample and 0.06 % for the 8 u.c. sample. Therefore it is concluded that we successfully demonstrated the open circuit voltage increase induced by the insertion of AgTaO₃ without killing their solar cell efficiency.

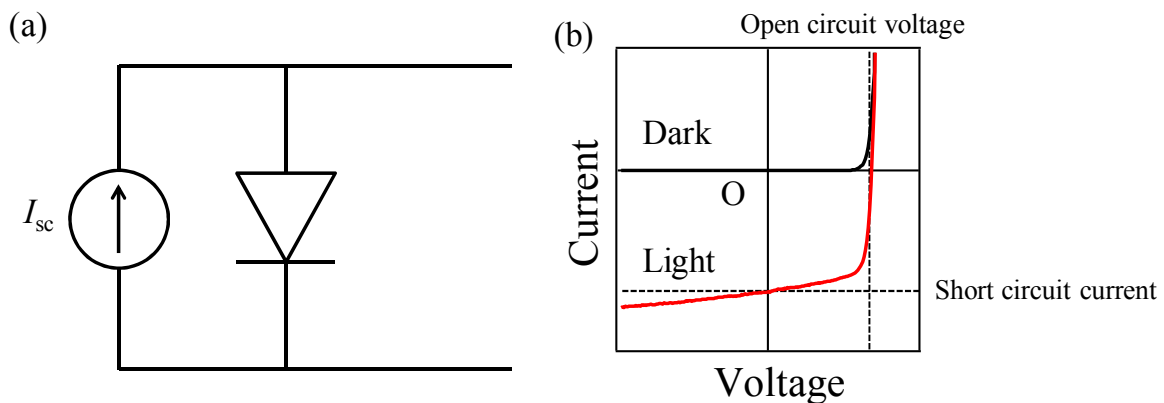


Figure. 6.10 (a) An equivalent circuit of a typical solar cell. (b) A typical I - V curve of a solar cell under photo irradiation. Definition of open circuit voltage and short circuit current are also given.

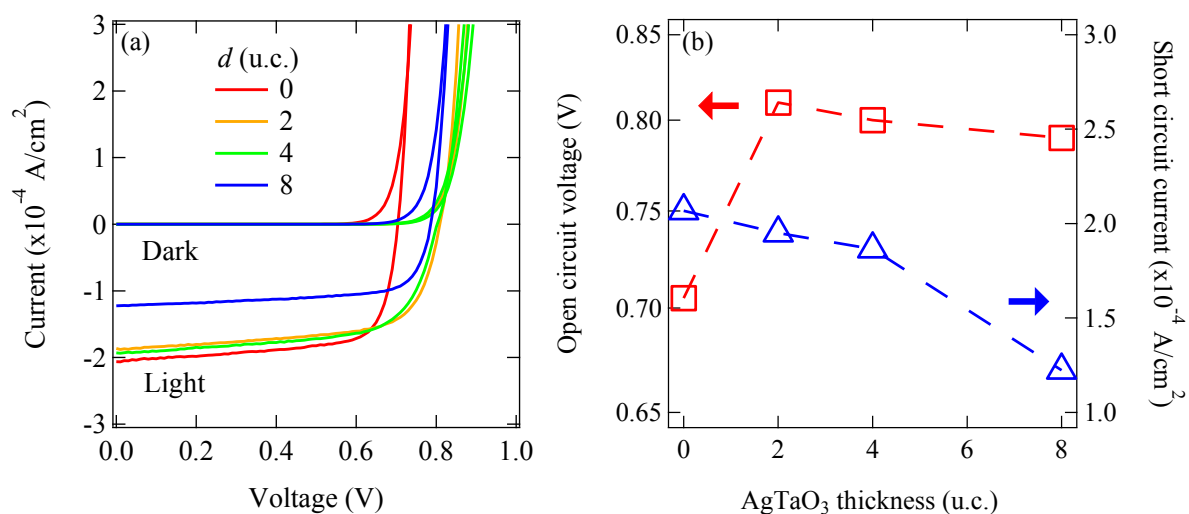


Figure. 6.11 (a) I - V curves of Pt (5 nm)/AgTaO₃ (d u.c)/Nb:SrTiO₃ (100) junctions under dark and light. (b) Thickness dependent open circuit voltage (left) and short circuit current (right).

6.6. Conclusion

Although there are several ABO₃ (A³⁺ B³⁺) perovskite insulators, attempts to increase band offsets using ABO₃ (A³⁺ B³⁺) perovskite insulator always face the instability issue of A-site terminated surface of perovskite semiconductor where negatively charged (AO₂)⁻ layer can be grown. In order to overcome this problem, we focused on AgTaO₃ as a dipole layer whose A site is negatively charged (AgO)⁻ layer and can be grown on stable TiO₂ terminated SrTiO₃ (100) surface. The high quality epitaxial AgTaO₃ film was obtained on Nb:SrTiO₃ (100) substrate under the high repetition rate and the high oxygen partial pressure that prohibits the reduction of Ag⁺ ion to a silver metal. The V_{bi} and SBH measured by C - V and IPE matched well and linearly increased until 8 u.c indicating the active role of AgTaO₃ as an electrostatic dipole. The possible device application of the dipole was demonstrated by the increase in the open circuit voltage of the dipole engineered Pt/Nb:SrTiO₃ Schottky junctions under light illumination.

6.7. Bibliography

- [1] T. Yajima PhD Thesis (2012).
- [2] Z.-Q. Li, J.-L. Zhu, C. Q. Wu, Z. Tang, and Y. Kawazoe, *Phys. Rev. B* **58**, 8075 (1998).
- [3] N. Nakagawa, H. Y. Hwang, and D. A. Muller, *Nat. Mater.* **5**, 204 (2006).
- [4] M. B. Telli, S. S. N. Bharadwaja, M. D. Biegalski, and S. Trolier-McKinstry, *App. Phys. Lett.* **89**, 252907 (2006).
- [5] J.-Y. Kim and A. M. Grishin, *Thin Solid Films* **515**, 615 (2006).
- [6] M. Łukaszewski, A. Kania, and A. Ratuszna, *J. Cryst. Growth* **48**, 493 (1980).
- [7] H. Soon, H. Taniguchi, and M. Itoh, *Phys. Rev. B* **81**, 104105 (2010).
- [8] H. Kato, H. Kobayashi, and A. Kudo, *J. Phys. Chem. B* **106**, 12441 (2002).
- [9] S.-G. Lim, S. Kriventsov, T. N. Jackson, J. H. Haeni, D. G. Schlom, A. M. Balbashov, R. Uecker, P. Reiche, J. L. Freeouf, and G. Lucovsky, *J. Appl. Phys.* **91**, 4500 (2002).
- [10] Ş. Altındal, S. Karadeniz, N. Tuğluoğlu, and A. Tataroğlu, *Solid-State Electronics* **47**, 1847 (2003).
- [11] E. Lesne, N. Reyren, D. Doennig, R. Mattana, H. Jaffrès, V. Cros, F. Petroff, F. Choueikani, P. Ohresser, R. Pentcheva, A. Barthélémy, and M. Bibes, *Nat Commun* **5**, 4291 (2014).

Chapter 7. Conclusion

Electronic devices based on conventional semiconductors ranging from transistors to light emitting diodes have made human life more convenient and more efficient throughout the 20th century. In the 21st century, transition metal oxides have attracted much attention as promising candidates for new device applications not achievable in conventional semiconductors. This stems from the diverse electronic properties they exhibit and their high chemical stability in the atmosphere. Despite the wide range of bulk properties readily available in oxides, controlling the interface energy band alignments of these oxides has a small degree of freedom because of the strong electronegativity of the oxygen anion which predominantly forms the valence band independent of the metal cations leading to fixed ionization energies. This limits access to utilizing the unique intrinsic properties for different device applications in oxide materials.

This problem can be resolved by considering the interface electrostatic boundary conditions. Band alignments for any pair of materials can be tuned by insertion of electrostatic dipoles at the interface. Recently, this concept has been applied to oxide interface systems and continuous band offset decrease has been demonstrated in an all perovskite SrRuO₃/0.02 at. % Nb doped SrTiO₃ (100) Schottky junction using a perovskite LaAlO₃ as a dipole layer.

Although the validity of the concept was demonstrated at all perovskite junction, there are two more challenges before the application of this technique to general oxide devices. First, practical interfaces in devices are not necessarily iso-structural where epitaxial

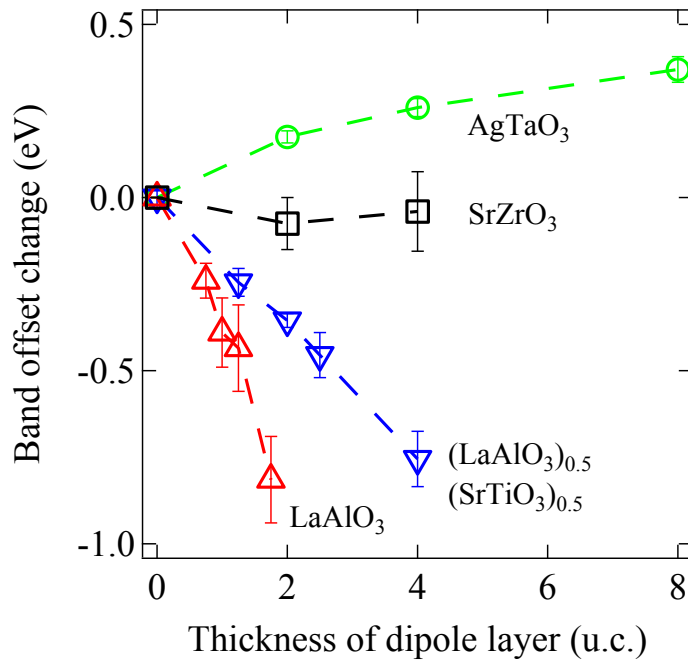


Figure. 7.1 The summary of band offset change induced by electrostatic dipoles employed in this study.

interfaces can be readily obtained. Given the large variations of the crystal structures and forms of oxides, the structural requirement of the oxide dipole has to be examined. In this study, polycrystalline Pt/LaAlO₃/anatase Nb:TiO₂/LaAlO₃ (100) heterojunction was utilized to study the feasibility of the oxide dipole. The Schottky barrier height was decreased only when LaAlO₃ was grown on (1 × 1) unreconstructed surface which is in epitaxial relation with LaAlO₃ but not on (1 × 4) reconstructed TiO₂ (100) surface. The magnitude of the Schottky barrier height lowering is proportional to the thickness of the oxide dipole layer and the charge density as shown in Figure. 7.1. These results suggest that, oxide dipoles are applicable to the interface consists of polycrystalline materials and non-perovskite oxides as long as the dipole layer/semiconductor interface is epitaxial.

Second, the tunable range of the band offset was large when decreasing but small when increasing. In order to release material choice for devices from the restriction for the band alignments, bi-directional band offset tuning is crucial for the device application. Band offset increase by using ABO₃ (A³⁺ B³⁺) perovskite insulators was hindered by the instability of semiconductor surface where negatively charged AO grows. In order to overcome this problem, we focused on AgTaO₃ as a dipole layer whose A site is negatively charged (AgO)⁻ layer and can be grown on stable TiO₂ terminated SrTiO₃ (100) surfaces. Schottky barrier height of Pt/AgTaO₃/Nb:SrTiO₃ (100) linearly increased with the thickness

of AgTaO₃ indicating the successful application of this concept as shown in Figure. 7.1. As an example of a potential application, the enhancement of open circuit voltage under 1 sun radiation was also demonstrated.

This band alignment tuning technique can be utilized for the various applications. For example, the Schottky barrier height of ferromagnetic metals and semiconductors can be tuned to improve the spin injection efficiency. The quantum efficiency in light emitting diodes and solar cells can be tuned by the insertion of oxide dipoles between p-type and n-type semiconductors varying the band offset. The electrical leakage in a gate electrode of a transistor can be suppressed by increasing the band offset.

For future development of dipole tuning, further improvement in techniques to increase the band offset is required since the built in potential in AgTaO₃ was small compared with that of LaAlO₃. One possible solution for this problem is a pair of SrAlO₃ and LaTiO₃ sandwiched by SrTiO₃ which can be regarded as a negatively and positively charged layer, respectively. Since both of them can be stably grown independent of the termination of SrTiO₃ (100) surface, the sign of the dipole can be tuned by just the growth order of the two charged layers as shown in Figure. 7.2.

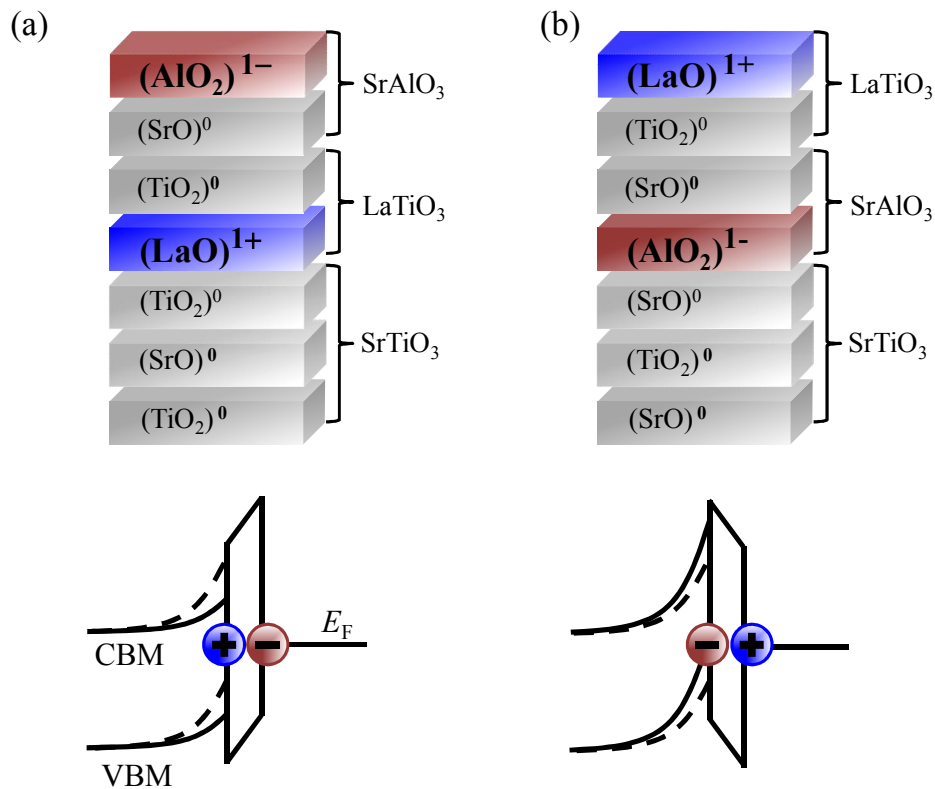


Figure. 7.2 Stacking structures and expected band alignments of (a) SrAlO₃/LaTiO₃/SrTiO₃ (100) and (b) LaTiO₃/SrAlO₃/SrTiO₃ (100).

In summary, we successfully formed oxide dipole layers at a polycrystalline metal and binary oxide interface and developed a technique to increase a band offset by forming a stable dipole layer which had been the two major challenges in previous studies as shown in Figure. 7.1. These results open the door to applying this band alignment tuning technique to a much wider range of various transition metal oxide devices, ranging from light emitting diodes to solar cells.

Acknowledgement

This Research has been carried out under the supervision of Prof. Hiroshi Okamoto and Prof. Harold Y. Hwang. I would like to acknowledge both professors for giving me such a precious opportunity to investigate an exciting research topic. I am especially grateful for Prof. Hwang for keeping close supervision in my activities and being kind as to share his scientific knowledge as much as the equipments and the assistance from his group members. I also appreciate for him to show how to make durable cardboard boxes.

I would like to express my deep gratitude to Prof. Hiroshi Okamoto, Prof. Takahisa Arima, Prof. Yoshihisa Harada, Prof. Tomoteru Fukumura and Prof. Mikk Lippmaa for their feedbacks for my thesis as defense committee members.

I would like to thank Dr. Yasuyuki Hikita, Dr. Makoto Minohara, Dr. Christopher Bell, and Mr. Yasuo Nakanishi for their direct supervision for my entire research. Especially I really appreciate to Dr. Hikita for his advises for my future carrier and research life that helps a lot for me to made a decision for my next job. I really appreciate Dr. Makoto's mentorship for my experiments and writing manuscripts.

I would like to thank Dr. Kazunori Nishio for sharing his advanced knowledge about pulsed laser deposition techniques and supporting to the construction of a new chambers and maintenance of a old chambers. I would like to appreciate Mr. Hisashi Inoue, Mr. Brian Sae Yoon Kim, Ms. Hyeok Yoon and Mr. Tyler Merz for their support for maintaining high vacuum chamber. I also acknowledges all the senior students in hwang group, Dr. Takeaki Yajima, Dr. Masayuki Hosoda, Dr. Hiroki Sato, Dr. Minu Kim and Mr. Satoshi Harashima for their kind support and guidance for my life in Hwang group.

I express my gratitude to experimental support from Mr. Yesheng Yee and Mr. Vijay Parameshwaran. They supported Auger electron spectroscopy measurement and open circuit voltage measurement. I am deeply grateful to Prof. Lena fitting Kourkoutis, Dr, Alberto Curto, Dr. Arturas vailionis, Mr. Xiaoge Liu, Mr. Yuta Matsui, and Ms. HyeRyoung Lee for their exciting research collaborations and discussions. I would like to acknowledge the financial support from the 21st century COE for my employment as a research assistant, and SLAC national accelerator laboratory as a visiting scholar. I would like to acknowledges the administrative assistance from Ms. Deborah Woodward, Ms. Yukiko Tan, Ms. Hiromi Toyoi, Ms. Matsuzaki Makiko and Ms. Sachie Iimura. The daily life in the lab could not have been so smoothly spent without the support from them

Finally, I would like to express my gratitude to my parents for giving me a great degree of freedom to choose my future and their thoughtful support for my life in overseas.

Appendix

A.1. Maxwell's equation for a metal insulator semiconductor junction.

In this appendix, the derivation of the Eq. (5.8) is explained. Consider the metal insulator semiconductor junction consists where insulator does not have electrostatic dipole and semiconductor is n-type. The schematic band diagram is shown in Figure A.1. The Maxwell's equation that has to be solved is following,

$$\frac{\partial^2 \phi(z)}{\partial z^2} = \frac{eN_D}{\epsilon_s} \quad (z_2 < z < z_1) \quad (\text{A.1})$$

$$\frac{\partial^2 \phi(z)}{\partial z^2} = 0 \quad (z \leq z_2 \text{ and } z_1 \leq z) \quad (\text{A.2})$$

where N_D is the dopant density in semiconductor, ϵ_s is the dielectric constant of semiconductor and $\phi(z)$ is the vacuum level of metal insulator semiconductor junction. z is defined as normal to the interface. The boundary conditions are given by

$$\phi(-\infty) = \frac{\partial \phi(-\infty)}{\partial z} = 0 \quad (\text{A.3})$$

$$\phi(0) = W \quad (\text{A.4})$$

where W is defined as the work function difference of metal and semiconductor. From the continuity of electric flux at the interface,

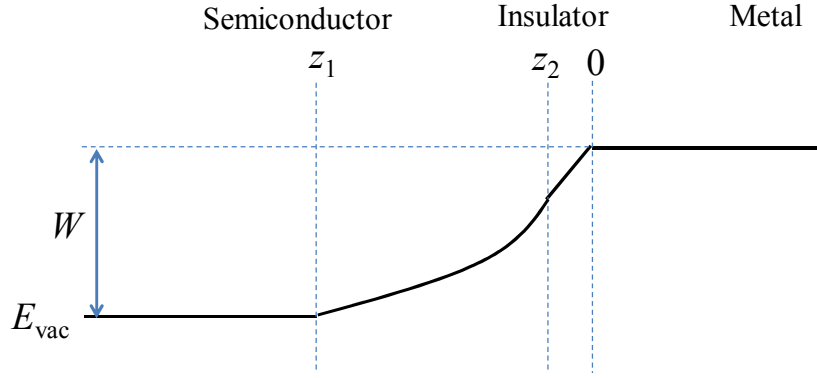


Figure A.1 A band alignment of a metal insulator semiconductor junction.

$$\epsilon_s \frac{\partial \phi(z_2 - 0)}{\partial z} = \epsilon_{\text{ins}} \frac{\partial \phi(z_2 + 0)}{\partial z} \quad (\text{A.5})$$

where ϵ_{ins} is the dielectric constant of insulator. Since there is no charges in the insulator, from (A.1), (A.2) and (A.5)

$$\begin{aligned} \phi(z_2 + 0) &= W - \int_{z_2}^0 \frac{\partial \phi(z)}{\partial z} dz = W - z_2 \frac{\partial \phi(z_2 + 0)}{\partial z} \\ &= W - \frac{\epsilon_s}{\epsilon_{\text{ins}}} z_2 \frac{\partial \phi(z_2 - 0)}{\partial z} \end{aligned} \quad (\text{A.6})$$

Since semiconductor is charge neutral at $z < z_1$, From (A.5)

$$\frac{\partial \phi(-\infty)}{\partial z} = \frac{\partial \phi(z_1)}{\partial z} = \phi(-\infty) = \phi(z_1) = 0 \quad (\text{A.7})$$

Therefore, solution for (A.1) is

$$\phi(z) = \frac{1}{2} \frac{eN_D}{\epsilon_s} (z - z_1)^2 \quad (\text{A.8})$$

Considering the continuity at $z = z_2$, from (A.6) and (A.8)

$$\phi(z_2) = \frac{1}{2} \frac{eN_D}{\epsilon_s} (z_2 - z_1)^2 = W + \frac{1}{\epsilon_{\text{ins}}} z_2 eN_D (z_2 - z_1) \quad (\text{A.9})$$

From the quadratic formula

$$z_1 = \frac{\left(1 - \frac{\epsilon_s}{\epsilon_{\text{ins}}}\right) z_2 N_d - \sqrt{\left(\frac{\epsilon_s}{\epsilon_{\text{ins}}} z_2 N_d\right)^2 + 2\epsilon_s W N_d}}{N_d} \quad (\text{A.10})$$

From (A.9), the ratio of voltage drops in the insulator and semiconductor are

$$\frac{V_{ins}}{V_s} = \frac{\frac{1}{\epsilon_{ins}} z_2 N_D (z_2 - z_1)}{\frac{1}{2\epsilon_s} N_D (z_2 - z_1)^2} = \frac{\frac{2\epsilon_s}{(z_2 - z_1)}}{\frac{\epsilon_{ins}}{z_2}} = \frac{2C_s}{C_{ins}} \quad (\text{A.11})$$

where $C_s = \epsilon_s/(z_2 - z_1)$ and $C_{ins} = \epsilon_{ins}/z_2$ is defined as the capacitance of depletion layer and insulator. From this formula,

$$\begin{aligned} V_{ins} &= W - V_s = W - \frac{2C_s}{C_{ins}} V_{ins} \\ V_{ins} &= W \frac{2C_s}{2C_s + C_{ins}} \end{aligned} \quad (\text{A.12})$$

A.2. Maxwell's equation for a MIS with a dipole layer.

Here the metal insulator semiconductor junction when insulator has electrostatic dipole will be considered. The schematic band diagram is shown in Figure A.2. The charge distribution of electrostatic dipole layer is defined as following

$$\rho(z) = Q\delta(z - z_2) - Q\delta(z) \quad (z_2 \leq z \leq 0) \quad (\text{A.13})$$

Therefore, the boundary condition (A.5) is modified as

$$\epsilon_s \frac{\partial \phi(z_2 - 0)}{\partial z} + Q = \epsilon_{ins} \frac{\partial \phi(z_2 + 0)}{\partial z} \quad (\text{A.14})$$

where ϵ_{ins} is the dielectric constant of insulator. Since there is no charges in the insulator, from (A.1), (A.2) and (A.14)

$$\begin{aligned} \phi(z_2 + 0) &= W - \int_{z_2}^0 \frac{\partial \phi(z)}{\partial z} dz = W + z_2 \frac{\partial \phi(z_2 + 0)}{\partial z} \\ &= W + \frac{\epsilon_s}{\epsilon_{ins}} z_2 \frac{\partial \phi(z_2 - 0)}{\partial z} + \frac{Q}{\epsilon_{ins}} z_2 \end{aligned} \quad (\text{A.15})$$

Since semiconductor is charge neutral at $z < z_1$, From (A.5)

$$\frac{\partial \phi(-\infty)}{\partial z} = \frac{\partial \phi(z_1)}{\partial z} = \phi(-\infty) = \phi(z_1) = 0 \quad (\text{A.16})$$

Therefore, the solution for (A.1) is

$$\phi(z) = \frac{1}{2} \frac{eN_D}{\epsilon_s} (z - z_1)^2 \quad (\text{A.17})$$

The first term in V_{ins} correspond to standard MIS voltage drop and second term is originated from dipole effect.